Hokkaido University

Construction of Photonic–Plasmonic Coupling Color Material Combining Structural Colors by Colloidal Particles and Localized Surface Plasmon Resonances by Metal Nitride Nanoparticles

A Dissertation submitted in partial satisfaction of the requirements
for the degree Doctor of Philosophy

in

Engineering

by

NOGUCHI Shinji

Committee in charge:

Professor SHIMADA Toshihiro, Chair
Professor MATSUI Masaki
Professor TADANAGA Kiyoharu
Associate Professor MIURA Akira

2025

DEDICATION

I dedicate this work to my peer, mentors, and family, who have strengthened my persistence and determination.

> Press on.
>
> Nothing in the world can take place of persistence.
>
> Talent will not; nothing in the world is more common than unsuccessful men with talent.
>
> Genius will not; unrewarded genius is almost a proverb.
>
> Education will not; the world is full of educated derelicts.
>
> Persistence and determination alone are omnipotent.
>
> — Calvin Coolidge

I, too, hold this belief.

TABLE OF CONTENTS

LIST OF FIGURES

LIST OF TABLES

VITA

2020 Bachelor of Science in Engineering, School of Engineering, Hokkaido University (Thesis title: Self-combustion Synthesis of Binary Metal Nitrides Using Sodium Amide)

2022 Master of Science in Chemical Sciences and Engineering, Graduate School of Chemical Sciences and Engineering, Hokkaido University (Master's thesis title: In-situ Measurement in Solid-State Reactions of Multicomponent Inorganic Compounds)

2025 (Doctor of Philosophy in Engineering, Hokkaido University)

PUBLICATIONS

- Related to This Dissertation

1-1 **Shinji Noguchi**, Akira Miura, Kiyoharu Tadanaga, Synthesis of ZrN–SiO_2 Core-shell Particles by a Sol–gel Process and Use as Particle-based Structured Coloring Material, *Journal of the American Ceramic Society*, Wiley, 107 (10), 6885-6895, 2024. (DOI: 10.1111/jace.19981)

1-2 **Shinji Noguchi**, Milena Lama, Yuta Fujii, Akira Miura, Kiyoharu Tadanaga, Structural Color Materials with Color Mixing Effect Using Noble Metal-Free Plasmonic Particles in SiO_2–ZrN System, *Advanced Optical Materials*, Wiley, 12 (19), 2400287, 2024. (DOI: 10.1002/adom.202400287) (**Inside front cover**)

- Other Publications

1-3 **Shinji Noguchi**, Jin Odahara, Hayato Sakai, Nataly Carolina Rosero-Navarro, Akira Miura, Kiyoharu Tadanaga, Combustion Reactions between Transition-Metal Chlorides and Sodium Amide and Their Ignition Temperature, *Inorganic Chemistry*, American Chemical Society (ACS), 60 (17), 12753-12758, 2021. (DOI: 10.1021/acs.inorgchem.1c00557)

1-4 **Shinji Noguchi**, Ryuji Kiyama, Masahiro Yoshida, Maradhana Agung Marsudi, Naohiro Kashimura, Kiyoharu Tadanaga, Jian Ping Gong, Takayuki Nonoyama, Real-Space Visualization of Charged Polymer Network of Hydrogel by Double Network Strategy and Mineral Staining, *Nano Letters*, American Chemical Society (ACS), 24 (29), 9088-9095, 2024. (DOI: 10.1021/acs.nanolett.4c02559) (**Supplementary cover**)

FIELD OF STUDY

Primary Field: Materials Chemistry, Studies in Inorganic Materials Chemistry
Professor TADANAGA Kiyoharu

ABSTRACT OF THE DISSERTATION

In recent years, structural color materials have garnered significant attention due to their high fade resistance and low toxicity compared to traditional pigments. Structural color materials exploit the physical phenomenon of selective reflection of specific wavelengths of light caused by periodic structures at the scale of the wavelength of light. However, these materials often exhibit angle-dependent reflection, making it challenging to achieve angle-independent coloration. Particle-based structural color materials composed of colloidal particles with sizes comparable to the wavelength of light can reduce angle dependence by forming quasi-amorphous structures with diminished crystallinity of the colloidal crystals. Nevertheless, this approach often results in reduced color contrast due to incoherent scattering.

To address this problem, this study aimed to develop structural color materials with tunable reflective properties by introducing metal nitride (MN) nanoparticles into the periodic particle-based structures. These materials combine structural color arising from the periodic structures with localized surface plasmon resonance (LSPR) of the MN nanoparticles, which selectively absorb specific wavelength regions through plasmonic absorption. In this work, the phenomenon where photonic effects from periodic structures and plasmonic absorption from MN nanoparticles coexist is defined as "photonic-plasmonic coupling."

Silica (SiO_2) was employed as the structural framework, and MN nanoparticles such as titanium nitride (TiN), zirconium nitride (ZrN), and hafnium nitride (HfN) were used as components for plasmonic absorption at specific wavelength regions. Two types of core-shell particles were

synthesized: (1) MN-SiO_2 core-shell particles with MN nanoparticles as cores and SiO_2 as shells, and (2) SiO_2-MN core-shell particles with monodispersed SiO_2 particles as cores and MN nanoparticles adhered to their surfaces. Quasi-amorphous structures were constructed using these core-shell particles, resulting in materials with reduced angle dependence and expression of photonic effects from the periodic SiO_2 structures and plasmonic absorption from MN nanoparticles. This work successfully developed photonic-plasmonic coupling structural color materials with enhanced tunability and functionality.

Keywords: Structural color, Localized surface plasmon resonance, Metal nitride, Monodisperse particles, Core-shell particles, Quasi-amorphous.

Chapter 1 General Introduction

1.1 Colorants and their types

In this section, the history of colorant utilization is discussed, followed by descriptions of the colorants currently in use and the methods employed to evaluate them.

1.1.1 History of colorants

Since ancient times, humans have been captivated by the allure of color, incorporating naturally occurring hues into their artistic and daily practices. The use of color traces back to the Paleolithic period, evidenced by the employment of natural pigments in cave paintings and body modifications.[1] These early pigments, sourced from soil, plants, and minerals, have been integral to human expression for tens of thousands of years.

In ancient Egypt, artisans crushed colored natural ores into powder to serve as pigments. It is believed that blue pigments were produced from azurite (copper ores) and green from malachite, while red pigments were derived from iron oxide.[2] As civilizations evolved, the extraction of pigments became more sophisticated, extending beyond the use of naturally occurring materials. For instance, in ancient India, the dye indigo was extracted from plants, marking a significant technological advancement in the utilization of natural substances for dyeing.[3]

Further technological innovations occurred around 2000 BC when the Egyptians began adding blue and green hues to glass by incorporating copper and iron oxides.[4] This practice was expanded by the Romans around the 1st century BC, who advanced glass manufacturing techniques, integrating colored glass into building materials and everyday objects.[5]

The Middle Ages saw further refinement in the use of pigments. In Europe, a plethora of coloring techniques were developed, each workshop inventing unique methods. Pigments such as

red lead and lapis lazuli, still prominent in modern inorganic pigment applications, were developed during this period.[6] The technology of glass coloring also proliferated throughout Europe, significantly influencing the art of medieval stained glass.[7]

The modern era ushered in the synthesis of synthetic dyes. The earliest synthetic dyes were derived from substances such as coal tar by Friedlieb Ferdinand Runge[8] and aniline, synthesized by August Wilhelm von Hoffmann,[9] the mentor of William Henry Perkin. In 1856, the synthesis of mauveine by British chemist William Perkin catalyzed a revolution in dye technology, enabling more vibrant and cost-effective coloring of materials.[10]

Despite the widespread adoption of synthetic dyes in the 20th century, concerns over their environmental and health impacts have emerged in recent decades. This has reignited interest in natural dyes and pigments. Concurrently, research has expanded into the development of functional pigments, including those capable of reflecting sunlight[11] and biodegradable pigments derived from sustainable resources,[12] reflecting ongoing efforts to harmonize technological advances with environmental stewardship.

Thus, the history of colorants has changed with the development of culture and technology and has evolved in response to human aesthetic pursuits and practical needs. In other words, the history of colorants is a mirror that reflects the history of humanity.

1.1.2 Organic colorants

Organic colorants, which are dyes and pigments based on organic compounds, exhibit a diverse array of colors and chemical properties. These colorants can be either synthetic or derived from natural sources, finding utility across a broad spectrum of industries.

Synthetic organic dyes such as azo dyes and phthalocyanine dyes are extensively used. Azo dyes, characterized by the presence of the azo group (-N=N-), are among the most prevalent synthetic organic dyes, producing vibrant red, yellow, and orange hues.[13] These dyes are predominantly utilized in the food, textile, and ink industries. Phthalocyanine dyes, noted for their blue and green shades, demonstrate exceptional resistance to light and chemicals, making them ideal for use in automotive paints and inks.[14]

Conversely, natural pigments like carmine, curcumin, and chlorophyll are derived from biological sources. Carmine, or cochineal pigment, is a red pigment extracted from the cochineal scale insect used in foods and cosmetics.[15] When extracted with warm or hot water, it is obtained as carminic acid and is insoluble as an aluminum salt. Curcumin, a yellow polyphenolic compound extracted from the turmeric root, is employed in food coloring and medicinal products.[16] Chlorophyll, sourced from green leaves, colors foods and beverages.

The classification of dyes and pigments hinges on their solubility and binding properties: dyes like carminic acid dissolve in solvents and chemically bond to substrates, imparting color, whereas pigments such as carmine are insoluble and adhere physically to surfaces. Due to their vivid colors and processing ease, organic colorants are vital in various fields including industrial products, art, cosmetics, and the food industry. However, carbon-based molecules are prone to "fading," a loss of color due to structural changes from decomposition by ultraviolet light or oxidation.[17] Efforts to mitigate fading and deterioration include improving molecular structures, polymer bonding, using stabilizers, and, for pigments, adjusting their shape and size. Despite these efforts, current technology cannot entirely prevent the decomposition and deterioration of organic colorants.

1.1.3 Inorganic colorants

Inorganic colorants, which include metal oxides, sulfides, and silicates, are pigments fundamentally rooted in inorganic compounds. These colorants are renowned for their exceptional stability and resistance to heat, light, and chemicals, making them indispensable in industries such as building materials, ceramics, and paints. Key examples of inorganic colorants include iron oxide, titanium dioxide, cadmium pigments, chromium pigments, and ultramarine pigments.

Iron oxide pigments offer a range of colors such as red, yellow, brown, and black, determined by the iron's valence state.[18] These pigments are highly stable and widely used in coloring outdoor paints, cement, and plastic products. Titanium dioxide, used primarily as a white pigment due to its high refractive index, enhances the whiteness of outdoor paints, plastics, and paper.[19] It also acts as a photocatalyst for the decomposition of water and organic materials under ultraviolet light.[20] Cadmium pigments, known for their vivid yellow hues, are made from cadmium-based compounds but are regulated due to toxicity.[21] Similarly, chromium pigments, derived from compounds containing chromium, are characterized by bright greens or yellows but also face usage restrictions due to health concerns.[22] Ultramarine pigments, composed of complex silicates containing sodium, aluminum, and sulfur, achieve their distinctive blue hue because the radical anion S_3^-, which is included in the silicate, absorbs red to yellow wavelengths of light while reflecting blue.[23] This is because some oxide ions in the silicate are replaced by sulfide ions, thereby shifting the band gap. These pigments are highly valued for their excellent lightfastness, making them ideal for use in art paints and cosmetics.

Inorganic colorants are favored in a broad spectrum of industries because of their chemical stability. They are particularly valued for their superior lightfastness, heat resistance, and chemical inertness compared to organic colorants. These pigments are less affected by sunlight

and weather, thus are more suited for outdoor applications. They maintain their color stability in high-temperature environments and are less reactive to chemicals and solvents, making them ideal for industrial applications. Consequently, inorganic pigments are commonly employed to color products that demand longevity, such as building materials, automotive paints, and ceramics. However, the use of pigments containing hazardous elements is increasingly regulated, prompting the development of safer and more sustainable alternatives.[24]

1.1.4 Other colorants

In addition to organic colorants and inorganic pigments, structural color represents a distinct category of coloration. Structural color arises not from the chemical composition of materials but from the interaction of light with the microstructure of an object. This type of coloration is the result of the surface or internal structure of an object forming specific patterns that cause interference, diffraction, and reflection of incident light, producing distinctive colors. These colors often vary depending on the angle of light incidence and observation, and they change with the lighting conditions.[25]

Structural color is generated through mechanisms such as interference, diffraction, and scattering of light. In phenomena like soap bubbles and an oil film on water, a thin film causes interference of light waves, selectively reinforcing certain colors.[25] Furthermore, objects like compact discs, some butterfly wings,[26] and certain bird feathers[27] possess fine lattices and patterns that diffract light, creating visible colors. In the case of scattering, structures of specific sizes scatter light where the color observed is influenced by Rayleigh scattering,[28] which colors the sky blue, and Mie scattering,[29] which makes clouds appear white.

Structural colors are prevalent in nature, observable in butterfly wings, bird feathers, and the shells of crustaceans. Technologically, structural colors find applications across a diverse range,

including security, art, decorative materials, and high-performance optical devices.[30] They are employed in banknotes and passports to enhance anti-counterfeiting measures. Displays leveraging structural colors are anticipated to offer vivid colors along with energy efficiency. Research is actively pursuing the development of new materials that replicate the principles of structural color observed in nature through biomimicry. Structural colors are particularly advantageous due to their sustainability and minimal environmental impact. Unlike chemical dyes, they are long-lasting and resistant to fading. Additionally, they can be produced using safe, commonly available raw materials, circumventing the issues associated with inorganic pigments. These characteristics render structural colors highly valuable for specific applications. The classification and properties of structural color materials is discussed in the following section.

1.1.5 Color evaluation

Various scientific techniques are employed to accurately measure and express colors. The principal methods include spectrum measurement, evaluation using a multi-angle spectrophotometer, and evaluation with a color difference meter. Spectrum measurement methods encompass both reflection and transmission spectrum measurements. Reflection spectrum measurement assesses the color of an object by analyzing the spectrum of light reflected from its surface. This method determines how light of different wavelengths is reflected, identifying the color based on this data. It is particularly suited for measuring the color of non-translucent materials like solids and powders and can analyze surface color characteristics in detail, facilitating easy color reproduction and comparison.

On the other hand, transmission spectrum measurement evaluates color by analyzing how light is absorbed as it passes through a material. This method is ideal for measuring the color of transparent materials, such as liquids and transparent solids.

Multi-angle spectrophotometers measure the reflection of light from different angles, making them capable of evaluating colors of materials with unique surface effects, such as gloss, metallic, and pearlescent finishes.[31] These instruments are beneficial for materials whose color appearance changes with the viewing angle, such as automotive paints and cosmetic products, enabling the accurate capture of complex visual color effects. This feature is crucial for product management and quality control.

Color difference meters quantify the difference between two colors as a numerical value based on a specified color space.[32] These devices are instrumental in industries that demand high color reproducibility, including printing, painting, and textiles, ensuring color consistency across productions.

Additionally, plotting the obtained spectrum as coordinates in a chromaticity diagram and a color space is possible. A chromaticity diagram, which illustrates hue and saturation (color purity), places colors on a two-dimensional plane.[33] This diagram helps visually understand the relationship between hue and saturation. The most widely used chromaticity diagram is the CIE xy chromaticity diagram, established by the Commission Internationale de l'Éclairage (International Commission on Illumination).[34] The CIE xy chromaticity diagram is a horseshoe-shaped diagram encompassing all colors perceptible to the human eye. The primary feature of the CIE xy chromaticity diagram is that the diagram represents only hue and saturation based on the tristimulus values of color and does not include brightness.

In contrast to the chromaticity diagram, a color space is a three-dimensional coordinate system that numerically expresses colors.[35] To fully describe a color, color spaces include three dimensions: hue, saturation, and brightness (or lightness). Among the various types of color spaces, RGB, CMYK, HSV, HSL, CIE XYZ, and CIE Lab are commonly used.

RGB color space, representing Red, Green, and Blue, is prevalent in evaluating digital displays such as televisions, computers, and smartphone screens.[36] The RGB color space creates colors by blending these three primary colors, based on the principle of additive color mixing where combining colors increases brightness and approaches white. This system allows for simple and intuitive color manipulation.

CMYK color space, standing for Cyan, Magenta, Yellow, and Key (Black), is essential in the printing industry. The CMYK color space utilizes four ink colors and operates on the principle of subtractive color mixing, where colors become darker upon mixing.[37] This system is ideal for accurate color reproduction in print.

HSV color space, or Hue, Saturation, and Value, breaks down color into three components: hue indicates the type of color, saturation denotes the vividness, and value reflects the brightness.[38] This model facilitates intuitive adjustments that align with human color perception.

HSL color space, which stands for Hue, Saturation, and Lightness, is frequently employed in web design. The HSL color space represents color with hue, saturation, and lightness, similar to HSV color space but differs in how brightness is handled, trending towards a middle gray, thus allowing for straightforward color balance adjustments and intuitive brightness control.[39]

CIE XYZ color space is a standard developed from scientific analysis of color reproducibility, designed to reflect colors as perceived by the human eye with three components: X, Y, and Z. The X component predominantly relates to red hues, Y represents luminance or brightness as perceived by the human eye, and Z is primarily associated with blue hues.[34] This space is excellent for color comparison and covers a wide color gamut.

CIE Lab color space aims to accurately represent color differences, where L* indicates lightness, a* the red-to-green spectrum, and b* the yellow-to-blue spectrum.[40] It employs nonlinear

conversions to approximate human visual perception and is advantageous for maintaining consistency across different media.

These color spaces are tailored for specific applications such as printing, digital display, and scientific analysis. Each color space is selected based on its strengths and the requirements of the usage environment. For example, RGB color space is the standard for digital imaging, CMYK color space is preferred for printing, and CIE Lab color space is widely utilized for precise color analysis and management. Unlike two-dimensional chromaticity diagrams, which show only hue and saturation without brightness, these color spaces provide a comprehensive quantification of color, including dimensions for hue, saturation, and brightness, tailored to their respective applications. Color spaces offer precise numerical representations and are utilized in digital imaging, printing, and other color management processes. Chromaticity diagrams are apt for the visual analysis of colors, whereas color spaces are crucial for the technical analysis and management of colors.

The method for calculating the colorimetric system is described below, using the XYZ colorimetric system as an example.[41]

1) Correction of Spectral Data

The spectral data $R(\lambda)$ (reflectance) is multiplied by the light source spectrum $S(\lambda)$ to calculate the corrected spectral data $P(\lambda)$. The calculation is as follows:

$$P(\lambda) = S(\lambda)R(\lambda) \quad (1)$$

Where:

$R(\lambda)$: Reflective spectrum of the sample

$S(\lambda)$: Reflective distribution of light source

2) Calculation of XYZ Values

the corrected spectral data $P(\lambda)$ is used to calculate the XYZ values using the following equations:

$$X = k \sum_{\lambda=380}^{780} P(\lambda)\bar{x}(\lambda)\Delta\lambda \quad (2)$$

$$Y = k \sum_{\lambda=380}^{780} P(\lambda)\bar{y}(\lambda)\Delta\lambda \quad (3)$$

$$Z = k \sum_{\lambda=380}^{780} P(\lambda)\bar{z}(\lambda)\Delta\lambda \quad (4)$$

Where:

$\bar{x}(\lambda)$, $\bar{y}(\lambda)$, $\bar{z}(\lambda)$: Standard observer functions

$\Delta\lambda$: Wavelength interval

k : Normalization factor

3) Calculation of the Normalization Factor

The normalization factor k is calculated using the following equation:

$$k = \frac{100}{\sum_{\lambda=380}^{780} S(\lambda)\bar{y}(\lambda)\Delta\lambda} \quad (5)$$

This factor is used to normalize the Y value to 100.

Furthermore, the X and Y values in the CIE XY chromaticity diagram are derived from the X, Y, and Z components of the CIE XYZ color space and are intrinsically related. The XY chromaticity diagram displays color in two dimensions, representing the chromaticity

coordinates of the CIE color space, which can indicate the hue and saturation of a color. However, as noted, it lacks information about the brightness of the color.

The x and y values in the XY chromaticity diagram are computed from the X, Y, and Z components of the CIE XYZ color space as follows:

$$x = \frac{X}{X + Y + Z} \tag{6}$$

$$y = \frac{Y}{X + Y + Z} \tag{7}$$

Here, x and y denote the chromaticity of a color, representing the "chromaticity coordinates" within the color space. These values specify the hue and saturation of the color and express the relative proportions of the three primary colors. However, the brightness of the color is represented by the Y value, which is the luminance component of the XYZ color space. This value is not determined by the color's position on the xy chromaticity diagram but is a crucial index that defines the color's brightness. Therefore, the x and y values of the xy chromaticity diagram, derived from the X, Y, and Z components of the XYZ color space, are specifically calculated to embody the perceived hue and saturation of the color.

1.2 Structural color

As discussed in the previous section, coloration mechanisms include organic colorants, inorganic colorants, and structural color materials, which show colors derived from the structure itself. This section explores structural colors, focusing on single-layer interference, multi-layer interference, and colloidal particle systems.

1.2.1 Monolayer-film interference system

Thin film interference occurs when light of a specific wavelength interacts with the thickness of a film, causing certain wavelengths to be strongly reflected. This interference depends on several factors, including the thickness of the film, the wavelength of the incident light, and the film's refractive index. The extent of reflection or transmission due to interference is determined by the path difference created by light reflecting and transmitting within the film relative to the light's wavelength.

The fundamental equation for calculating thin film interference is as follows:[42] if the film's thickness is d, the wavelength of light is λ, the refractive index of the film is n, and the angle of incidence is θ (with θ' being the angle inside the film), the path difference Δ traveled by the light through the film is given by:

$$\Delta = 2nd\cos(\theta') \tag{8}$$

Here, θ' is the angle within the film, determined by Snell's law, calculated as:

$$\sin(\theta') = \frac{\sin(\theta)}{n} \tag{9}$$

The resulting phase difference, due to the path difference, is:

$$\delta = \frac{2\pi}{\lambda}\Delta \tag{10}$$

For light reflection, constructive interference occurs when the phase difference is an integer multiple of 2π, and destructive interference when it is an odd multiple of π\piπ. Thus, the condition for maximum reflection is:

$$\delta = 2m\pi \ (m\text{: integer}) \tag{11}$$

Modifying this equation yields the condition for enhanced interference:

$$2nd\cos(\theta') = m\lambda \tag{12}$$

where m represents the order of interference (an integer). Under these conditions, specific wavelengths are strongly reflected, producing visible colors, or act as an anti-reflection function depending on the context.

This optical phenomenon has practical applications, such as the development of color-producing anti-corrosion coatings on magnesium alloys,[43] and the creation of colorful, mechanically robust surface treatments for magnesium alloys.[44] Refractory metals like Ru, Ta, and W can form surface oxides when heated, which can be colored through thin film interference.[45] Additionally, thin films have been designed to achieve perfect light absorption in systems using a single lossy dielectric layer much thinner than the incident wavelength;[46] new types of optical coatings have been developed to selectively absorb different frequency ranges of incident light using highly absorptive ultrathin films with thicknesses ranging from a few to tens of nanometers;[47] and reports have detailed the control of absorption and reflection contrast with ultrathin film coatings.[48,49] Asymmetric structural color reflective materials have also been developed by integrating gold nanoparticles into titania thin films, enhancing the effects of thin-film interference.[50,51]

1.2.2 Multilayer films interference system

When multiple thin films are stacked, they exhibit colors resulting from the interference of light that penetrates through the films. Each layer possesses a different refractive index, and interference occurs when light of certain wavelengths is reflected or transmitted at each interface, causing some wavelengths to be amplified while others are diminished. The refractive index and thickness of each layer determine which wavelengths are emphasized or attenuated.

Alternating layers of materials with high and low refractive indices alter the pattern of light reflection and transmission, enhancing specific wavelengths through interference. Since the

response of the multilayer film structure varies with the angle of incidence of light, the observed color changes with variations in observation angle and light source.

Coloring due to multilayer interference is observable in natural structures, such as shellfish, and is utilized in numerous technological applications and products. It is employed in the production of filters that selectively transmit certain wavelengths of light, as well as in anti-reflective coatings that minimize unwanted reflections on lenses and screens. Additionally, this technology is implemented in currency and identification cards, serving as a security feature to prevent counterfeiting.

The theoretical calculation of structural color due to multilayer interference includes the calculation of interference conditions that take into account the refractive index and thickness of each layer, the wavelength of light, etc. Basically, it can be considered an extension of the calculation of interference for a single layer to multiple layers, but when considering the interference of a multilayer film, more complex calculations of phase addition and reflection and transmission coefficients are required. In the case of monolayer film, as described in the previous section, the path difference Δ is calculated as follows:

$$\Delta = 2nd\cos(\theta') \tag{13}$$

Here, n is the refractive index, d is the thickness of the film, and θ' is the angle of incidence of light within the film. Furthermore, the phase difference δ is calculated using the following formula, and the reflection intensity is determined by the interference conditions.

$$\delta = \frac{2\pi}{\lambda}\Delta \tag{14}$$

In the case of a multilayer film, the above travel path difference and phase difference are calculated for each layer to determine the total travel path difference and phase difference for the light that passes through all layers. The transfer matrix method is used to calculate the overall

reflectance and transmittance, considering the interference of reflection and transmission at each interface.[52] With this method, matrices are constructed based on the refractive index and thickness of each layer, and the overall reflectance and transmittance can be obtained by calculating the product of these matrices. The following transfer matrix is defined for each layer:

$$M_i = \begin{bmatrix} \cos(\delta_i) & \frac{-i\sin(\delta_i)}{p_i} \\ -ip_i\sin(\delta_i) & \cos(\delta_i) \end{bmatrix} \quad (15)$$

Here, $p_i = n_i \cos(\theta_i)$, and δ_i is the phase difference of layer i. The total matrix M through all layers is calculated as the product of the matrix of each layer, and the overall reflectance R and transmittance T are calculated from the total matrix M using the elements of the total matrix. The total matrix is expressed in the following form:

$$M = \begin{bmatrix} M_{11} & M_{12} \\ M_{21} & M_{22} \end{bmatrix} \quad (16)$$

This matrix represents the overall optical properties from the incident medium of the first layer to the incident medium of the last layer. If the refractive indices of the incident medium and the exit medium are n_0 and n_s,the transmittance T and reflectance R are calculated as follows. Since the transmittance indicates how much light remains after passing through all layers, the transmittance T also depends on the refractive indices of the incident medium and the exit medium and is expressed in the following form.

$$T = \left|\frac{1}{M_{22}}\right|^2 \frac{n_s}{n_0} \quad (17)$$

Reflectance R indicates how much of the incident light is reflected and can be expressed by the following formula:

$$R = \left|\frac{M_{21}}{M_{22}}\right|^2 \quad (18)$$

Using this calculation, it is possible to predict the behavior of light at specific wavelengths and design materials with specific optical properties, which makes it possible to design anti-reflective coatings or bandpass filters that enhance or cancel the light of specific colors. Recent reports of structural color materials using multilayer interference include anodized aluminum photonic crystal films with adjustable structural color[53] and magnesium-based reflective filters prepared by magnetron sputtering.[54] In addition, multilayer films that control not only reflection but also reflection and transmission have been developed.[55,56] In addition, multi-layer film materials are applied to an electrochromic device that exhibits the Janus effect, characterized by materials that display different optical properties depending on whether they are viewed from the front or the back[57] and a multilayer structure that created an optical Janus effect was reported.[58]

Structural color materials utilize multilayer interference made of inorganic compounds and structural color materials utilize multilayer interference made of organic compounds. Photonic crystals made of polymers was reported using block copolymers, and in this study, 1D photonic structures were created by self-assembling the polymers through coating and crosslinking.[59] Photonic hydrogels have also been made by self-assembly of amphiphilic polymers and a structure in which lamellar amphiphilic bilayers of poly(dodecyl glyceryl itaconate) (PDGI) are alternately embedded in the matrix using hydrophilic polyacrylamide (PAAm) hydrogels, in which the bilayer domains function as "reflectors" and the hydrogel exhibits structural color.[60]

1.2.3 Colloidal particle system

Similar to the interference of light in a monolayer film and the interference of light in a multilayer film, when the refractive index changes periodically in a structure composed of particles, a reflection of a specific wavelength occurs, and it can be used as a structural color material. The mechanism can be explained by light interference, diffraction, and Bragg

reflection. In light interference, the gaps formed between particles and the position of the particles themselves interfere with the light wave, emphasizing a specific color. In light diffraction, if the arrangement of particles is equal to or smaller than the wavelength of light, the light is diffracted by the particles and scattered in multiple directions, causing a change in color. In Bragg reflection, if the particles are regularly arranged, light incident at a specific angle is reflected according to Bragg's law, resulting in a vivid color.

When modeling particle-based structural colors, they can be understood by the interference of scattered light and the diffraction theory.[61] When particles scatter light, the scattered light from adjacent particles causes interference, emphasizing a specific color. This interference can be modeled using the following scattering matrix theory.

$$I = \sum_{i,j} a_i a_j^* e^{ik(r_i - r_j)} \tag{19}$$

Here, I is the intensity of the light obtained, a_i is the amplitude of scattering by the i -th particle, k is the wave vector ($k = 2\pi/\lambda$, λ is the wavelength of light), and r_i and r_j are the positions of the particles. This sum is calculated across all particle pairs to generate an interference pattern. Diffraction theory can explain color development when particles have a periodic arrangement. In a model that applies Bragg's law, the conditions for light to be diffracted by the particle arrangement and for strong reflection to occur at a specific angle are shown as follows:

$$n\lambda = 2d\sin\theta \tag{20}$$

Here, n is an integer (diffraction order), d is the distance between particles, and θ is the angle of incidence of light.

In addition, the particle material (refractive index and absorptivity), shape (sphere, rod, etc.), and arrangement regularity greatly affect the appearance of color. When Mie scattering theory is used

for the particle's refractive index n and diameter a, the scattering efficiency Q_{scat} can be expressed by the following formula.

$$Q_{\text{scat}} = \frac{2\pi}{k^2}\sum_{n=1}^{\infty}(2n+1)\left(|a_n|^2 + |b_n|^2\right) \quad (21)$$

Here, a_n is the size parameter $x = \frac{2\pi a}{\lambda}$, and b_n is the Mie coefficient which depends on the refractive index ratio $m = n_{\text{particle}}/n_{\text{medium}}$.

Color occurs as a result of the interaction of the optical properties given by these theories.

Particle-based structural color materials are mainly composed of monodisperse colloidal particles. [62,63] For organic compounds, polymers such as polystyrene,[64] PMMA,[65] PDA PNIPAM,[66,67], polysulfide (PSF)[68] have been synthesized as monodisperse particles, but this dissertation describes the inorganic compound particles and their layering method, which are the subject of this dissertation. Amorphous colloidal particles include SiO_2 particles prepared by the sol-gel method,[69–72] TiO_2 particles,[73,74] and Se particles prepared using the polyol method.[75,76] Single crystal particles include Cu_2O particles obtained by reducing a precursor[77–80] and monodisperse particles of bismuth produced by pyrolysis of the precursor and by melting and emulsifying metal powders to produce monodisperse metal particles.[81] This technique has also been extended to low-melting point metals such as Pd, In, Sn, and Cd.[82] Polycrystalline monodisperse particles include ZnO particles formed by the sol-gel process,[83,84] Ce_2O which can be prepared by the polyol process,[85] and Cu_2O particles prepared by reducing Cu(II) salts with various reducing agents at room temperature or high temperature.[86–89] Iron oxides such as hematite (α-Fe_2O_3)[90] and magnetite (Fe_3O_4)[91,92] have been synthesized as monodisperse particles. In addition to oxides, monodispersed particles of cadmium sulfide have been prepared.[93]

These particles are packed through self-assembly driven by evaporation of the dispersion medium, gravity-induced sedimentation, external fields, and supersaturation-induced sedimentation, as well as other techniques such as spray coating, inkjet printing, and spin coating. Evaporation-induced self-self-assembly is one of the most widely used methods for fabricating photonic crystal films from monodisperse particles, in which the evaporation of the solvent generates capillary forces that transport the monodisperse spheres to the air-solvent-substrate interface, where self-assembly occurs.[94,95] Gravity-induced sedimentation is a method in which the sedimentation of particles is induced by centrifugation, etc., and the particles self-assembled by sedimentation to make colloidal crystals.[96] External field-induced self-assembly is a method in which particles self-assembly uses external fields such as electric and magnetic fields instead of gravitational ones. In this process, the particle surface is modified to give it magnetic or electric field responsiveness, resulting in particles that self-assemble in response to an external field.[97–99] In the supersaturation-induced precipitation self-assembly method, monodispersed particles are dispersed in an effective volatile solvent with a low boiling point and then mixed with a target solvent with a high boiling point to form a uniform dispersion. When most of the effective solvent evaporates and the resulting solution is further cooled to room temperature, metastable photonic crystal pieces wrapped around the residual solvent spontaneously precipitate from the saturated solution of the target solvent.[100] In spray coating, air or inert gas is used as the working gas, and the suspension is sprayed from a nozzle to evaporate the solvent in the droplets and deposit the powder uniformly on the substrate. Vivid structural color patterns have been obtained by spray coating inks in which monodispersed ZnS particles, or Cu_2O particles are dispersed in a dispersion medium such as ethanol.[101,102] Inkjet printing is accomplished by facilitating the self-assembly of highly ordered structures through components

that strongly interact with specially pretreated substrates featuring low surface tension.[103–105] In spin-coating, droplets of a dispersion containing colloidal spheres are deposited onto a firmly fixed substrate. The substrate is then accelerated to a constant rotation speed, causing the droplets to spread due to centrifugal force. Meanwhile, due to the rapid evaporation of the solvent, capillary and shear forces drive the particles toward an aggregate, forming a dry photonic crystal film of controllable thickness.[106–108]

As described above, particle-based structural color materials have been produced using various constituent materials and particle packing methods. However, as theory shows, the optical properties of both film-based and particle-based structural color materials depend on the angle of incidence of light, so some ingenuity is required to produce structural color materials that exhibit angle-independent coloring. In particle-based structural color materials, structural colors with low angle dependence can be obtained through amorphous arrangements that lack long-range order and possess local periodic structures.[109–112] This colloidal structure is called quasi-amorphous and has been studied as an approach to structural color materials with low-angle dependency.[113] However, in exchange for the low angle-dependence, these materials usually have a pale color and no luster because of occurring incoherent scattering.[114–117] For this reason, black materials are introduced to the structure as a means of overcoming the angle dependence and low contrast to suppress incoherent scattering. Examples of black materials that were introduced into the structures include carbon black,[118–120] polydopamine,[121,122] polypyrrole,[123] or Fe_3O_4.[124,125] By this approach, structural color materials with low angle dependence and high contrast were reported.

However, by introducing a component that absorbs specific wavelength range rather than absorbing the entire visible light range through black materials, it is possible to prepare a color material that combines the effects of structural color due to photonic properties based on periodic structures and specific wavelength range absorption. The effect is called the color mixing effect. Using metal nitride plasmonic properties, I tried to realize the materials with a color mixing effect.

1.2.4 Application of structural color

Structural color materials are applied to take advantage of the advantages. For example, they have been used as stimuli-responsive materials, such as thermally responsive photonic stickers,[126] electrically responsive photonic crystals, anti-counterfeiting tags using electrically responsive photonic crystals,[127] and electrically and thermally responsive photonic films.[128] They have also been researched as energy materials,[129] such as solar cells[130] and smart windows.[131] In addition, structural color materials have been applied as anti-counterfeiting films,[129,132] materials that can encrypt pre-engraved information when immersed in a specific solvent,[133] and materials that quantitatively show wettability through changes in structural color,[134] as well as uses in photonic catalysts.[135–140], etc.

1.3 Structural color materials with color mixing effect

Incorporating components that absorb specific wavelength range into structures that exhibit structural colors allows for exhibiting the color mixing effect. These materials demonstrate optical characteristics that combine the effects of specific wavelength reflection inherent to the structure and specific wavelength range absorption. This section focuses on materials that

include inorganic compounds leveraging the band gap for specific wavelength range absorption, as well as those utilizing localized surface plasmon resonance (LSPR) by noble metal nanoparticles. This section describes examples from each area of study. Lastly, the potential for using LSPR by metal nitride nanoparticles is explored.

1.3.1 Structural color materials using optical band gaps of inorganic compounds

α-Fe_2O_3/SiO_2 core-shell nanoparticles were reported as structural color materials that incorporate inorganic compounds into particle-based structural color materials and combine visible light absorption based on the band gap of inorganic compounds with diffraction due to the periodic structure of particles.[141] In addition, colloidal photonic crystals with high transparency were reported by adjusting the refractive index by using ZnS@SiO_2 core-shell particles.[142] Some research on particle-based structural color that combines specific wavelength diffraction and light absorption based on the band gap of inorganic compounds was reported. However, more research has been reported on structural color materials utilizing specific wavelength range absorption by LSPR, and this was further explained in the following section.

1.3.2 Structural color materials using noble metal nanoparticles as specific wavelength range absorbers

Color control is also achieved by introducing particles exhibiting LSPR. In this phenomenon, the collective oscillation of electrons on the particle surface occurs in response to an electric field, absorbing specific energies. This is known to occur in nanoparticles of noble metals such as gold,[143,144] silver,[145,146] and palladium.[147,148]

This phenomenon can be described as quantized plasma oscillations, yet it can also be accurately explained using classical physics. Plasmon oscillations can be considered as the mechanical

motion of the electron gas in metals, specifically, the displacement of the electron gas relative to the fixed ion cores in the presence of an external field. In the case of bulk plasmons, these oscillations occur at the plasma frequency and possess energy characterized by the following equation.

$$E_p = \hbar \sqrt{\frac{ne^2}{m\varepsilon_0}} \tag{22}$$

where ε_0 represents the permittivity of free space, n denotes the electron density, and m is the electron mass. At the surface of metals, plasmons take the form of surface plasmon polaritons (SPPs), also commonly referred to simply as surface plasmons. These surface plasmons can be optically excited and couple to either localized or propagating surface plasmon modes through the metal surface's lattice or defects. The excitation of surface plasmons is driven by the oscillating electric field of the incident plane wave; therefore, light with a larger angle of incidence (i.e., light whose wave vector k is nearly parallel to the surface) couples most efficiently.

When surface plasmons are confined within particles of a size comparable to the wavelength of light, namely nanoparticles, the collective oscillations of the free electrons within the particles give rise to what is known as localized surface plasmons (LSPs). There are two significant effects associated with LSPs. First, the electric field near the surface of the particle is significantly enhanced, with the maximum enhancement occurring at the surface and rapidly decreasing with distance. Secondly, the optical extinction of the particles peaks at the plasmon resonance frequency, which occurs within the visible wavelength range for noble metal nanoparticles. This extinction peak is dependent on the refractive index of the surrounding

medium, making it useful for applications such as sensing.[149] To gain a deeper understanding of how localized surface plasmon resonance occurs, it is necessary to examine scattering theory. The Maxwell equations, as analyzed by Gustav Mie in 1908, describe the scattering and absorption of light by spherical particles.[29] When considering a homogeneous conductive sphere irradiated by a plane wave, the resulting scattered field allows for the calculation of the total scattering σ_{sca}, extinction σ_{ext}, and absorption cross-sections σ_{abs}.[150]

$$\sigma_{\mathrm{sca}} = \frac{2\pi}{|k|^2}\sum_{L=1}^{\infty}(2L+1)\left(|a_L|^2 + |b_L|^2\right) \tag{23}$$

$$\sigma_{\mathrm{ext}} = \frac{2\pi}{|k|^2}\sum_{L=1}^{\infty}(2L+1)\left[Re(a_L + b_L)\right] \tag{24}$$

$$\sigma_{\mathrm{abs}} = \sigma_{\mathrm{ext}} - \sigma_{\mathrm{sca}} \tag{25}$$

where k represents the wave vector of the incident wave, and L are integers representing the dipole, quadrupole, and higher multipoles of the scattering. In the equations mentioned, a_L and are b_L parameters composed of Riccati–Bessel functions ψ_L and χ_L.

$$a_L = \frac{m\psi_L(mx)\psi'_L(x) - \psi'_L(mx)\psi_L(x)}{m\psi_L(mx)\chi'_L(x) - \chi'_L(mx)\chi_L(x)} \tag{26}$$

$$b_L = \frac{\psi_L(mx)\psi'_L(x) - m\psi'_L(mx)\psi_L(x)}{\psi_L(mx)\chi'_L(x) - m\chi'_L(mx)\chi_L(x)} \tag{27}$$

Here, $m = \tilde{n}/n_m$, where $\tilde{n} = n_R + in_l$ represents the complex refractive index of the metal, and n_m is the real refractive index of the surrounding medium. Additionally, $x = k_m r$, where r denotes the radius of the particle. The wave number $k_m = 2\pi/\lambda_m$ is defined not as the wave number in vacuum but rather as the wave number within the medium.

Assuming that the nanoparticles are much smaller than the wavelength of light, $x \ll 1$. Under this condition, the Riccati–Bessel functions can be approximated by power series. Following

Bohren and Huffman (Bohren, CF; Huffman),[150] if only the terms up to x^3 are retained, equations 26 and 27 can be simplified as follows:

$$a_1 \approx -\frac{i2x^3}{3}\frac{m^2-1}{m^2+1} \tag{28}$$

$$b_1 \approx 0 \tag{29}$$

Furthermore, higher order terms for a_L and b_L become zero. To calculate the real part of a_1 as required by Equation 25, substitute $m = (n_R + in_I)/n_m$ into Equation 28.

$$a_1 = -i\frac{2x^3}{3}\frac{n_R^2 - n_1^2 + i2n_R n_I - n_m^2}{n_R^2 - n_1^2 + i2n_R n_I + n_m^2} \tag{30}$$

Next, switch to the complex metal dielectric function represented as $\tilde{\varepsilon} = \varepsilon_1 + i\varepsilon_2$, which captures the following relationship:

$$\varepsilon_1 = n_R^2 - n_1^2 \tag{31}$$

$$\varepsilon_2 = 2n_R n_I \tag{32}$$

Upon transitioning to the dielectric function of the medium, $\varepsilon_m = n_m^2$. With these substitutions, the relationship can be expressed as follows:

$$a_1 = \frac{2x^3}{3}\frac{-i\varepsilon_1^2 - i\varepsilon_1\varepsilon_m + 3\varepsilon_2\varepsilon_m - i\varepsilon_2^2 + i2\varepsilon_m^2}{(\varepsilon_1 + 2\varepsilon_m)^2 + (\varepsilon_2)^2} \tag{33}$$

By substituting Equation 33 into Equation 24 and considering only the dipole terms, an expression for nanoparticle plasmon resonance is obtained.

$$\sigma_{\text{ext}} = \frac{18\pi\varepsilon_m^{3/2}V}{\lambda}\frac{\varepsilon_2(\lambda)}{[\varepsilon_1(\lambda) + 2\varepsilon_m]^2 + \varepsilon_2(\lambda)^2} \tag{34}$$

Here, V represents the volume of the particle. Following a similar process, the subsequent scattering cross-section σ_{sca} can be derived.

$$\sigma_{\text{sca}} = \frac{32\pi^4\varepsilon_m^2V^2}{\lambda^4}\frac{(\varepsilon_1 - \varepsilon_m)^2 + (\varepsilon_2)^2}{(\varepsilon_1 + 2\varepsilon_m)^2 + (\varepsilon_2)^2} \tag{35}$$

These small-particle approximations are strictly applicable only to particles with diameters less than 10 nm. However, it has been found that predictions of dielectric sensitivity remain accurate for larger particles as well.[151]

When the denominator of Equation 34 reaches its minimum, the extinction cross-section is maximized. This condition is satisfied when $\varepsilon_1 = -2\varepsilon_m$. This indicates that the localized surface plasmon resonance (LSPR) extinction peak is dependent on the dielectric constant of the surrounding medium.

To find the dependence of the LSPR peak wavelength on the dielectric function of the medium, the analytical, frequency-dependent form for ε_1 from the Drude model of the electronic structure of metals can be used.[152] This classical model of electron transport within conductors describes the collisions between freely moving electrons and the stationary lattice of heavy ion cores, providing an approximation very close to the actual conductivity of noble metals.:

$$\varepsilon_1 = 1 - \frac{\omega_p^2}{\omega^2 + \gamma^2} \tag{36}$$

Here, ω_p represents the plasma frequency, and γ is the damping parameter of the bulk metal. In the case of visible and near-infrared frequencies, where $\gamma \ll \omega_p$, the above expression can be simplified as follows:

$$\varepsilon_1 = 1 - \frac{\omega_p^2}{\omega^2} \tag{37}$$

By applying this equation to ε_1 and setting $\varepsilon_1 = -2\varepsilon_m$ to satisfy the resonance condition, the following expression can be derived:

$$\omega_{\max} = \frac{\omega_p}{\sqrt{2\varepsilon_m + 1}} \tag{38}$$

Here, $\omega_{\max}$ represents the peak frequency of the LSPR. By converting the frequency to wavelength using $\lambda = 2\pi c/\omega$, and converting the dielectric constant to the refractive index using $\varepsilon_m = n^2$, the above equation can be reformulated as follows:

$$\lambda_{\max} = \lambda_p \sqrt{2n_m^2 + 1} \tag{39}$$

where $\lambda_{\max}$ is the LSPR peak wavelength, and λ_p corresponding to the wavelength for bulk metal. Consequently, the dependency of the LSPR peak wavelength on the refractive index is approximately linear at optical frequencies.

Consequently, in localized surface plasmon resonance, wavelengths with specific energies are absorbed, determined by the material's dielectric constant, particle size, and the dielectric environment of the medium.

The introduction of these nanoparticles into particle-based structural color materials allows for tuned coloration. [153] Similar approaches were reported for SiO_2–Au and SiO_2–Ag composite particles,[154,155] which utilize localized surface plasmon resonance for specific wavelength range absorption in conjunction with periodic structure-based reflection, thereby providing an alternative to bandgap absorption. In addition, reconfigurable protein-based plasmonic-photonic crystal hybrid nanostructures were reported.[156] However, these noble metals are costly due to their rarity and compete with uses in jewelry and electronic components. In this study, I developed structural color materials incorporating plasmonic properties without the use of precious metals by integrating metal nitride nanoparticles, which exhibit plasmonic characteristics, into a periodic structure.

1.3.3 Metal nitride nanoparticles as alternative specific wavelength range absorbers to precious metal nanoparticles

As described in the previous section, noble metal nanoparticles such as Au and Ag are the most extensively studied plasmonic nanomaterials due to their strong extinction in the visible and near-infrared regions. However, the high cost of noble metals like Au and Ag poses a limitation for large-scale commercial applications. Additionally, the low melting points of nanoscale metals render them unsuitable for high-temperature applications.[157,158]

Cost-effective alternative plasmonic materials that exhibit not only effective plasmonic responses but also high chemical and thermal stability have been researched. In this regard, metal nitrides have emerged as promising candidates to replace noble metals.[159–161] Computational analyses have demonstrated that transition metal nitride nanoparticles such as TiN, ZrN, and HfN, possess metallic electronic structures and exhibit absorption and scattering in the visible and near-infrared regions for nanoparticles with a radius of 50 nm. Due to differences in the dielectric constants of TiN, ZrN, and HfN, the oscillation frequency of the electrons varies, leading to changes in the wavelength at which the nanoparticles exhibit the strongest light absorption LSPR peak.[162] These properties have been experimentally confirmed, with synthesized transition metal nitride nanoparticles displaying plasmonic characteristics.[163]

Various processes have been developed to synthesize plasmonic metal nitride nanoparticles, including laser ablation,[164,165] non-thermal plasma,[166] arc plasma,[167] solid–gas-phase synthesis,[168] and solid-state synthesis.[163] Among these, solid-state synthesis is one of the simplest approaches, enabling the fabrication of metal nitride nanoparticles through the solid-phase reaction of oxide precursors with magnesium nitride. The resulting metal nitride nanoparticles were reported to exhibit plasmonic properties.[163]

However, the use of plasmonic properties of metal nitride nanoparticles for specific wavelength range absorption in structural color materials has remained unexplored. This dissertation focused on the development of structural color materials that incorporate metal nitride nanoparticles as specific wavelength range absorption components to address the cost and mining-related issues associated with noble metals. In this dissertation, the phenomenon exhibiting both photonic properties from periodic structures and specific wavelength range absorption by the LSPR in metal nitride nanoparticles was defined as photonic–plasmonic coupling. By combining oxides to form periodic structures and utilizing the LSPR in metal nitride nanoparticles, this study aimed to develop photonic–plasmonic coupling color materials that integrated photonic and plasmonic effects.

1.4 Aim and strategies of this work

This dissertation focuses on developing particle-based structural color materials with photonic–plasmonic coupling properties, integrating reflective properties from periodic structures and specific wavelength-absorbing properties by the components. Components that absorb specific wavelength range were embedded into the structure to achieve this integration. Silica was used as a structural material, while metal nitride nanoparticles showing localized surface plasmon resonance were employed as specific wavelength range absorbing components. The size of SiO_2 particles used as structural materials was on the order of several hundred nanometers, whereas the metal nitride nanoparticles used as specific wavelength range absorbing components were just a few tens of nanometers in size.

The primary objective is to develop materials that eliminate the need for precious metals, show low angular dependence, and allow for controlled reflection through adjustments to the periodic structure and controlled absorption by selecting and varying the concentration of metal nitride nanoparticles. Core-shell structures combining metal nitride and silica were synthesized for this purpose. The aim is to utilize these structural color materials by preparing metal nitride-silica core-shell particles, with metal nitride nanoparticles as the core, and silica-metal nitride core-shell particles, with silica as the core and metal nitride nanoparticles as shell particles. In the case of the silica-metal nitride core-shell particles, the prepared particles used smaller shell particles than core particles, and since the shell particles did not completely cover the core, they qualified as "core-satellite particles." Core-satellite particles comprise a primary central core surrounded by smaller, discrete satellite particles that are not connected to form a continuous shell.[169] However, core-satellite particles are also included in the broader definition of core-shell particles;[170] therefore, for consistency in terminology, the prepared particles containing SiO_2 and metal nitride nanoparticles were referred to as core-shell particles. The silica-metal nitride core-shell particles were prepared by attaching an amount of metal nitride nanoparticles around monodisperse SiO_2 core particles that did not significantly affect the monodispersity of the whole particles. As a result, although the diameter of the core-shell particles was slightly larger than that of the SiO_2 particles alone, the overall monodispersity was maintained.

To reduce angular dependence, colloidal particles were formed into quasi-amorphous structures, principally by producing particle-stacked films. The optical properties of these materials were assessed by measuring their reflection spectra and analyzing the angular dependence of the reflected light.

Through these strategies, I aimed to develop photonic-plasmonic coupling color materials that combine the photonic properties derived from the periodic structure of the composition with the plasmonic characteristics of the embedded metal nitride nanoparticles.

1.5 Contents of this dissertation

This dissertation begins with an introduction chapter that explores the background of structural color materials. It emphasizes the significance of developing structural color materials that control absorption and reflection without the use of noble metals, which is the central aim of this research. The second chapter introduces zirconium nitride (ZrN) as a specific wavelength range absorber, capable of absorbing around 700 nm due to LSPR, and discusses the synthesis and evaluation of ZrN-SiO_2 core-shell particles. The third chapter expands this investigation to include titanium nitride (TiN) and hafnium nitride (HfN) as specific wavelength range absorbing species, detailing the preparation and evaluation of TiN-SiO_2 and HfN-SiO_2 core-shell particles. The fourth chapter describes the synthesis process for SiO_2-ZrN core-shell particles used in structural color materials, focusing on the reversed roles of metal nitride nanoparticles and silica, and their optical properties. The fifth chapter investigates materials that manage reflection by adjusting the size of silica particles and control absorption through the species and distribution density of metal nitride nanoparticles, including further developments with TiN and HfN. The sixth and final chapter concludes the findings and discusses their implications for the field of structural color materials.

Chapter 2 Synthesis of ZrN-SiO_2 Core-shell Particles by a Sol-gel Process and Use as Particle-based Structured Coloring Material

2.1 Introduction

Core-shell particles feature a central core containing a distinct component enveloped by an outer shell composed of another compound. Core-shell particles present a method for preparing materials with novel properties and applications ranging from catalysis[51,171–175] to electronic,[176,177] magnetic,[178,179] or optical devices.[180–182] In inorganic compounds, a conspicuous emphasis is on the functionality of core-shell particles comprising metal nitrides. Core-shell particles containing metal nitrides have unique characteristics that hold the potential for a diverse range of applications, including catalysis,[183,184] optical sensing,[185] and energy conversion.[186] In recent years, several core-shell nanostructures composed of metal nitrides and metal oxides were prepared, and their functions were reported.[187–190] In the combination of metal nitrides and oxides, the preparation of core-shell particles requires a component encompassing the selection of materials, choice of the synthesis process, and envisaging of desired properties. The core-shell architecture confers upon these particles an amalgamation arising from the unique traits of metal nitrides and oxides. By careful selection of the core and shell constituents and designing structures from the chemical and physical perspectives, such as catalytic activity, magnetism, stability, and surface area, a variety of properties that surpass those of homogeneous materials or simple mixtures can be achieved. For example, cobalt-based nitride core oxide shells,[187] Fe_2N stabilized by core-shell formation with iridium oxide,[184] and Fe_4N-IrO_2 core-shell particles[188] have successfully acted as catalysts while enhancing both the catalytic activity and stability. The advantages arising from the combination of metal oxides and nitrides were reported in the field of energy materials.[189] Core-shell nanostructures of metal nitrides and metal oxides

have also been explored in magnetic nanodevices and biomedical applications.[190] Thus, the core-shell formation of metal oxides and metal nitrides has the potential to adjust the interactions between metal oxide and metal nitride, increase stability, and rise new materials. However, metal nitride/metal oxide core-shell materials have not been employed in applications to exploit both the optical properties of the metal nitride core and the morphology of the entire core-shell particle.

This study considers ZrN as a core material because it exhibits LSPR. Moreover, LSPR is a phenomenon characterized by the resonance of electrons on the surface of a particle, induced by collective vibrations. The selective absorption of particular light wavelengths by materials is attributed to electron resonance upon light absorption, resulting in collective vibrations. LSPR occurs in noble metal nanoparticles, such as gold, silver, and platinum. Recently, metal nitride nanoparticles were reported to exhibit LSPRs. Karaballi et al. reported that TiN, ZrN, and HfN nanoparticles, which are nitrides of group four elements, exhibited LSPR.[163] Exarhos et al. synthesized core-shell zirconium nitride–silicon oxynitride nanoparticles using chemical vapor deposition (CVD) and confirmed that the formed nanoparticles exhibited LSPR.[191] The absorption wavelength was controlled by coating the ZrN nanoparticles with silicon oxynitride. Moreover, ZrN-SiO_2 core-shell particles were theoretically suggested to boost the efficiency of Pb-free perovskite solar cells to reach up to 20%.[192] From an optical perspective, ZrN and core-shell nanoparticles containing ZrN are expected to gain attention in the future. However, a process for preparing ZrN-SiO_2, which is ZrN coated with SiO_2, has not yet been reported. The formation of ZrN-SiO_2 core-shell particles at ambient temperature and pressure is more valuable than the formation of these particles using processes such as plasma CVD or nitridation with NH_3 gas. Some studies discussed the synthesis of metal nitrides without the use of

NH_3 gas.[193,194] In particular, the liquid-phase process is appropriate as a low-energy process for preparing ZrN-SiO_2 core-shell particles in mass production.

I utilized the Stöber process,[72] as a liquid-phase process, to prepare core-shell particles. The Stöber process is a typical method for synthesizing monodisperse silica particles.[195] The Stöber process involves hydrolysis and polycondensation of silicon alkoxides under basic conditions to obtain uniformly sized particles. Thus, the Stöber process has been used for the core-shelling of Au,[154,196–200] Ag,[201] Fe_2O_3,[141] Fe_3O_4,[202] $CsPbBr_3$,[203] $CdSe/Cd_xZn_{1-x}S$,[204] and nanoscale diamond[205] with silica.

In this study, ZrN nanoparticles exhibiting LSPR were synthesized, and ZrN-SiO_2 core-shell particles were prepared by coating silica around the obtained ZrN nanoparticles using the sol-gel process. By employing these particles as a material that constitutes the structural color, I evaluated the possibility of achieving a material that reflects specific wavelengths from a highly uniform particle size.

2.2 Results and Discussion

The mixture of ZrO_2 nanopowder (**Figure 2.1**) and Mg_3N_2 powder was heated at 1000°C to obtain dark green products. The products obtained after the reaction contained ZrN, MgO, and Mg_3N_2 (**Figure 2.2**). ZrN and MgO were formed through the reaction of ZrO_2 with Mg_3N_2, while the residual Mg_3N_2 was due to an excess of 3 molar equivalents of Mg_3N_2 added to ZrO_2, resulting in unreacted Mg_3N_2 remaining. The reaction of ZrO_2 and Mg_3N_2 forming ZrN is as follows.[163]

$$6ZrO_2 + 4\ Mg_3N_2 \rightarrow 6ZrN + MgO + N_2$$

The obtained dispersion, which was washed in the HCl solution, was blue in color, as shown in **Figure 2.3.a**. The products were observed by transmission electron microscopy (TEM) to confirm their morphology. **Figure 2.3.b-d** shows the TEM image of the products. The products consisted of particles, each size 10–20 nm. From **Figure 2.3.d**, it can be observed that the interplanar spacing in the particles is 0.28 nm. This spacing corresponds to the (100) plane of ZrN. **Figure 2.3.e** shows the X-ray diffraction (XRD) profile of the dried particles. The XRD profile of the products exhibits peaks originating from the ZrN phase. The result indicates that the washing process dissolved and removed the unreacted Mg_3N_2 and the formed MgO, while the insoluble ZrN remained. Peaks observed at 33° and 45° in the XRD pattern are considered to be attributable to impurities that formed during the washing process. The particle size distribution was derived by analyzing the small-angle X-ray scattering (SAXS) intensity (**Figure 2.4**). The particle size distribution shows a mode at approximately 3 nm, which decreases as the particle size increases, as shown in **Figure 2.3.f**. The average particle size is approximately 12 nm. The average crystal size of the obtained ZrN, derived from the XRD profile using the Debye–Scherrer equation, is 11 nm. This result satisfactorily agrees with the average particle size of ZrN determined from SAXS measurements (12 nm), suggesting the validity of the particle size distribution calculated using the SAXS. These particles were sufficiently small to exhibit LSPRs.[163] The absorption spectrum of the ZrN nanoparticle dispersion exhibits a peak at approximately 700 nm, as shown in **Figure 2.1.g**. The dispersion of ZrN nanoparticles exhibited increased absorbance at wavelengths below 400 nm. This phenomenon is attributed to Rayleigh scattering by ZrN particles. Rayleigh scattering is applicable when particle size d is considerably smaller than the wavelength of light λ, typically represented as $d << \lambda$. This implies significant Rayleigh scattering occurs when the particle

diameter is less than one-tenth of the wavelength, that is, $d < \lambda/10$.[28] Given the average particle size of ZrN nanoparticles was 12 nm, it was posited that light with wavelengths shorter than 400 nm is strongly scattered, resulting in reduced transmitted light intensity.

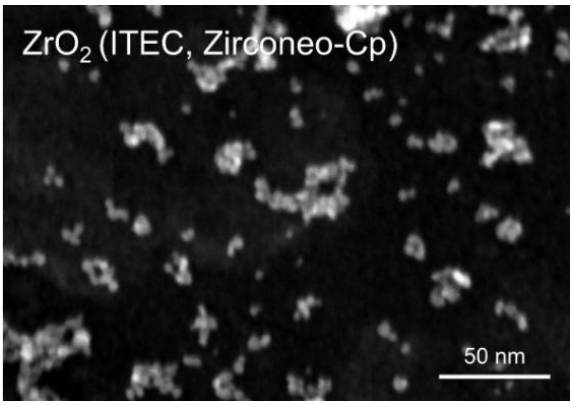

Figure 2. 1 STEM image of the starting material ZrO_2 nanoparticles (ITEC, Zirconeo-Cp).

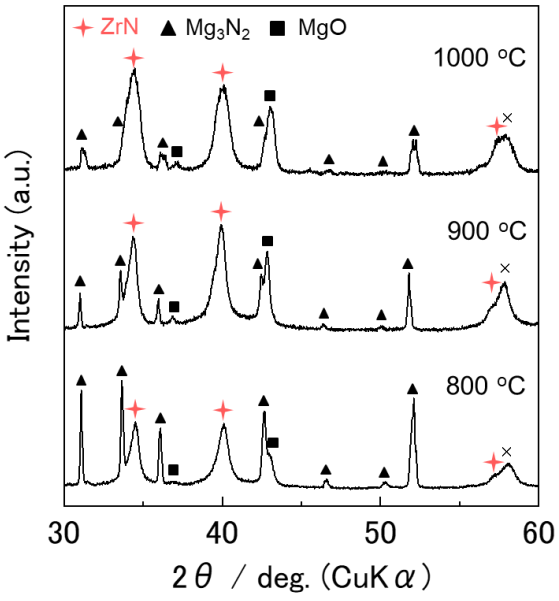

Figure 2. 2 XRD profiles of the products before washing. The products were obtained by heating a mixture of ZrO_2 and Mg_3N_2 at 800 °C, 900 °C, and 1000 °C under a flow of N_2 gas.

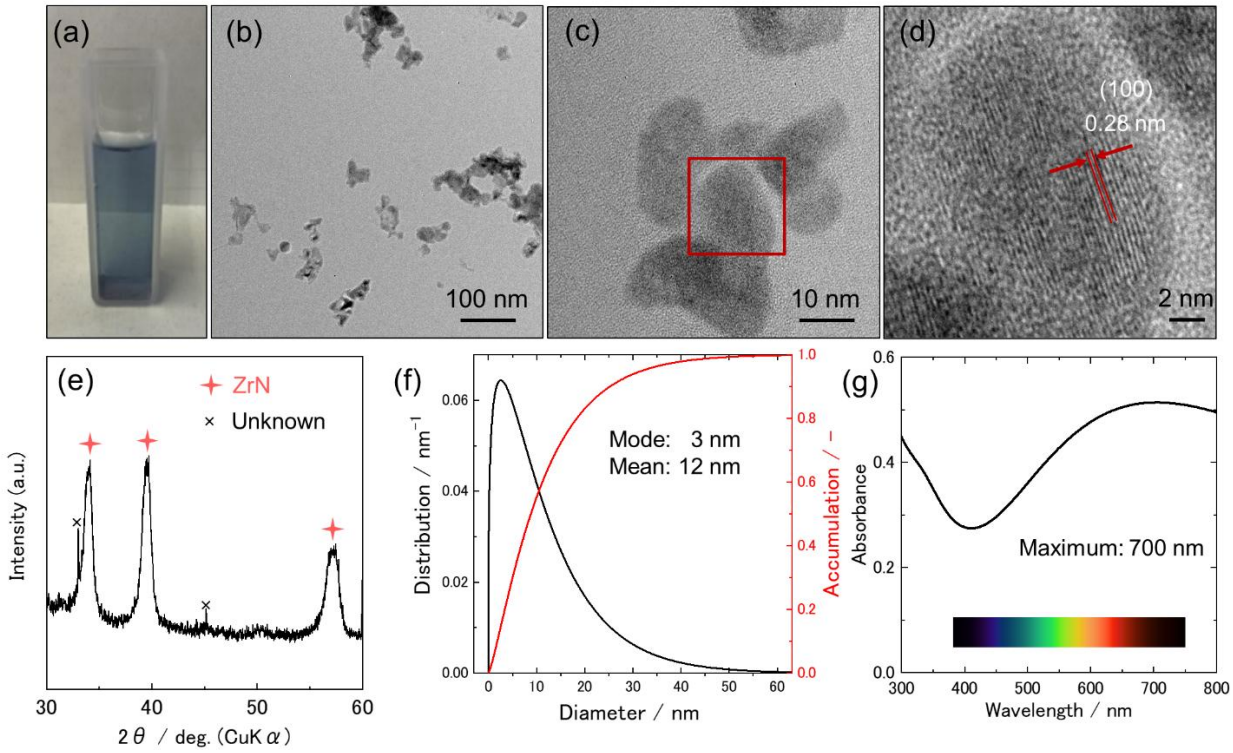

Figure 2. 3 Photograph, TEM images, XRD profile, particle size distribution, and absorption specrum of the sample. **(a)** Photograph of the diluted particle dispersion. Transmission electron microscopy (TEM) images of the product from ZrO_2 and Mg_3N_2. **(b)** Low magnification image. **(c)** Medium magnification image. **(d)** High magnification image. **(e)** X-ray diffraction (XRD) profile of the dried particles obtained. **(f)** Particle size distribution derived by analyzing the small-angle X-ray scattering (SAXS) intensity (Figure 2.4). **(g)** Absorption spectrum of the diluted particle dispersion.

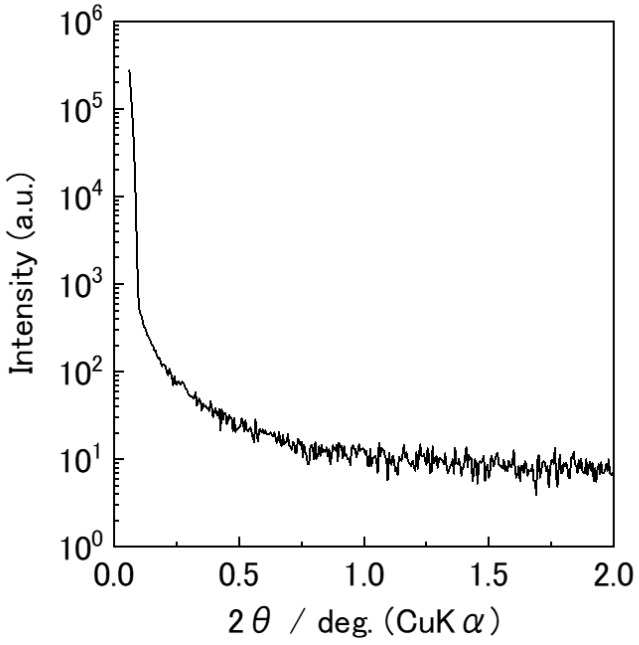

Figure 2. 4 SAXS profile of the obtained ZrN particle dispersion.

The ZrN-SiO_2 core-shell particles were synthesized using the obtained ZrN dispersions. The dark blue solution transformed to a white hue as the reaction proceeded (**Figure 2.5**). During this process, the solution did not undergo gelation and precipitation. After each reaction, the particles were collected by centrifugation. **Figure 2.6** shows the photographs of the particles obtained at each reaction time. The color of particles changed from dark purple to gray white as the amount of silica produced increased with the reaction time. Subsequently, the morphology of the synthesized particles was examined using scanning transmission electron microscopy (STEM). **Figure 2.7** shows the high-angle annular dark-field (HAADF) STEM images of the particles obtained at various reaction times (40, 180, 300, and 1440 min). Spherical particles with internal cores are observed at all reaction times. The morphology of the core particles reflects the

agglomeration state of the ZrN nanoparticles. Since ZrN particles are not present in a completely separated state of crystallites, as shown in **Figure 2.3.b**, there are instances where agglomerated ZrN particles are coated with SiO_2. The particle sizes obtained at reaction times ranging from 40 to 1440 min are approximately 250–700 nm. As shown in **Figure 2.8**, the particle size distribution was obtained using the HAADF STEM images (**Figure 2.9**). The averages of the particle sizes are 289, 497, 628, and 715 nm at reaction times of 40, 180, 300, and 1440 min, respectively. Therefore, particles can be prepared by tuning the particle size and adjusting the shell thickness by varying the reaction time. Moreover, the HAADF STEM images are obtained by detecting forward-scattered electrons, and the intensity of these images is directly proportional to the atomic number of elements. Therefore, heavy atoms appear brighter, whereas light atoms appear darker. Interestingly, the HAADF STEM images showed that the core area of the particle was brighter than the shell area, indicating a different composition between the core and shell.

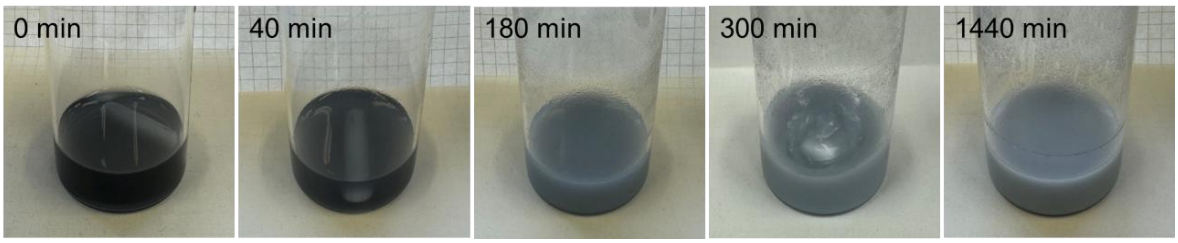

Figure 2. 5 Photographs of the sol at the reaction times of 0 min, 40 min, 180 min, 300 min, and 1440 min.

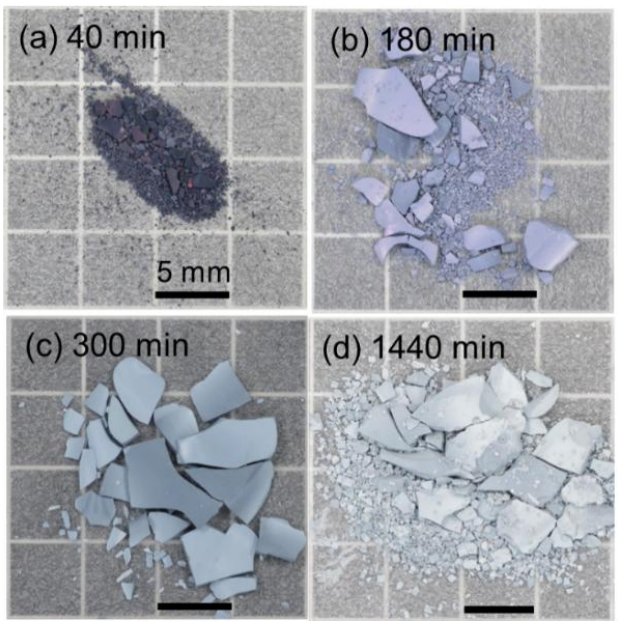

Figure 2. 6 Photographs of particles synthesized at reaction times of **(a)** 40 min, **(b)** 180 min, **(c)** 300 min, and **(d)** 1440 min.

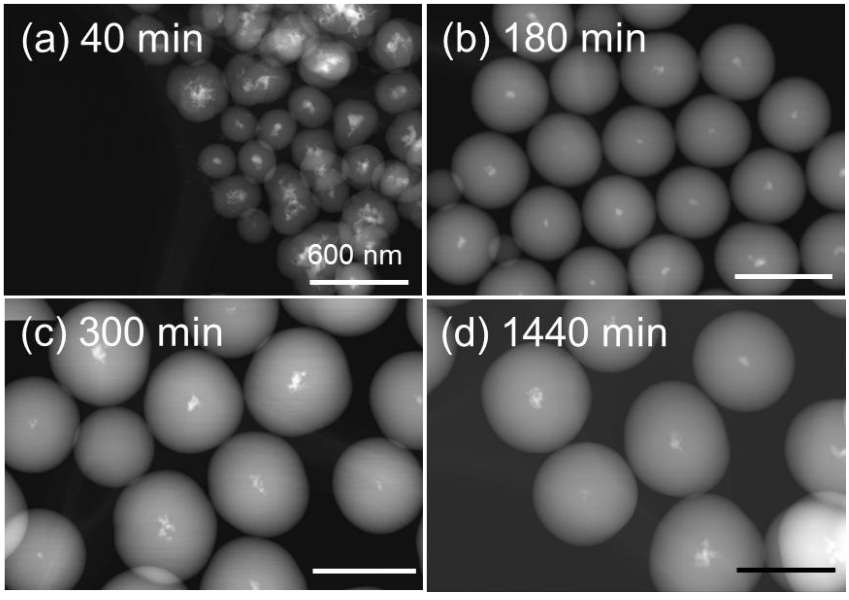

Figure 2. 7 HAADF STEM images of the particles produced at the reaction times of **(a)** 40 min, **(b)** 180 min, **(c)** 300 min, and **(d)** 1440 min.

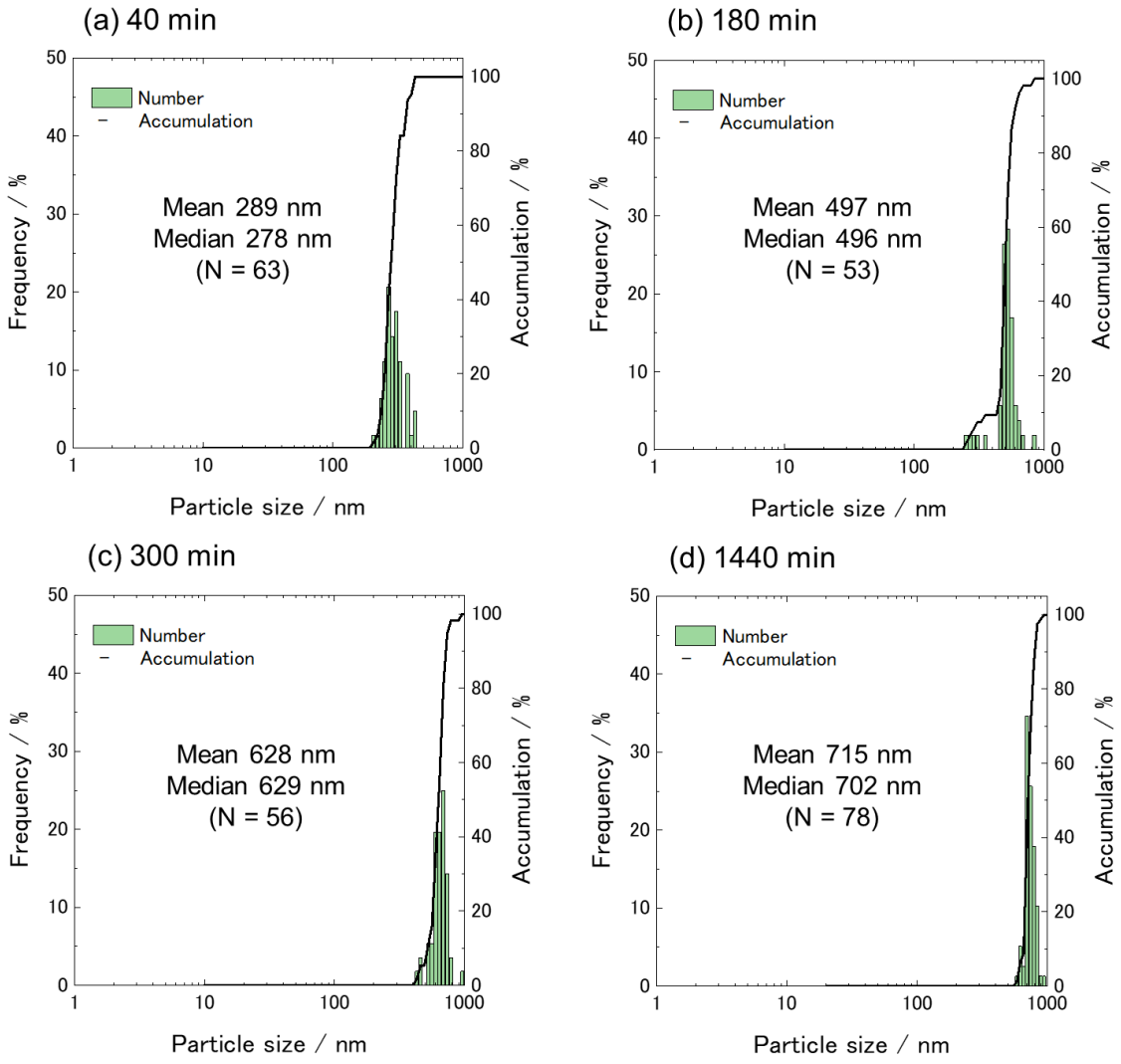

Figure 2. 8 Size of the particles produced at the reaction times of **(a)** 40 min, **(b)** 180 min, **(c)** 300 min, and **(d)** 1440 min.

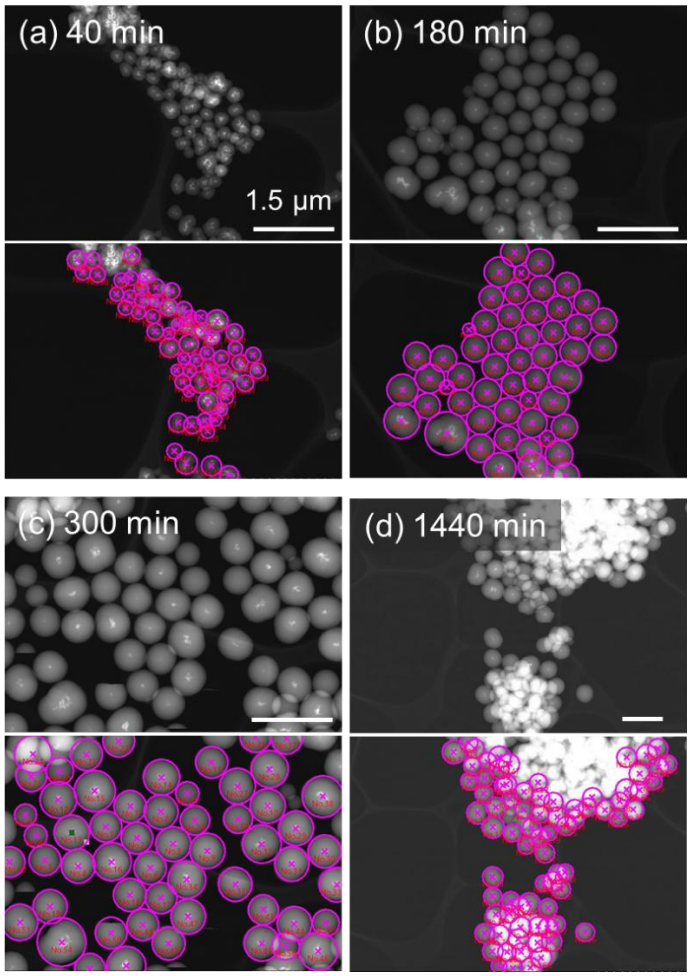

Figure 2. 9 HAADF STEM images and target areas for analysis of the particles produced at the reaction times of **(a)** 40 min, **(b)** 180 min, **(c)** 300 min, and **(d)** 1440 min.

To investigate the shell formation Fourier transform infrared (FTIR) and Raman spectra of the products at designated reaction times were measured (**Figures 2.10**). The FTIR spectra at reaction times of 0 min, 40 min, 180 min, 300 min, and 1440 min with the 4000–1500 cm^{-1} range are displayed in **Figure 2.10.a** and with the 1500–500 cm^{-1} range in **Figure 2.10.b**. **Figure 2.10.c** presents the Raman spectra of the products. From FTIR and Raman spectra, the formation of SiO_2 was confirmed after 40 min, and the intensity of bands based on

Si-O gradually increased with an increase in the reaction time. The intensity of the bands based on O-H groups decreased with an increase in the reaction time. These behaviors indicate that the SiO_2 network was formed with an increase in reaction time, and consistent with the trends observed in **Figures 2.7** and **2.8**. In addition, only very weak C-H bands based on unreacted ethoxy groups (around 3000 cm^{-1}) were observed. Because the intensity of the bands based on O-H groups and C-H groups in core-shell particles is very weak, we believe that the effect of the unreacted ethoxy group or O-H groups on the fabrication of particle assemblies is negligible.

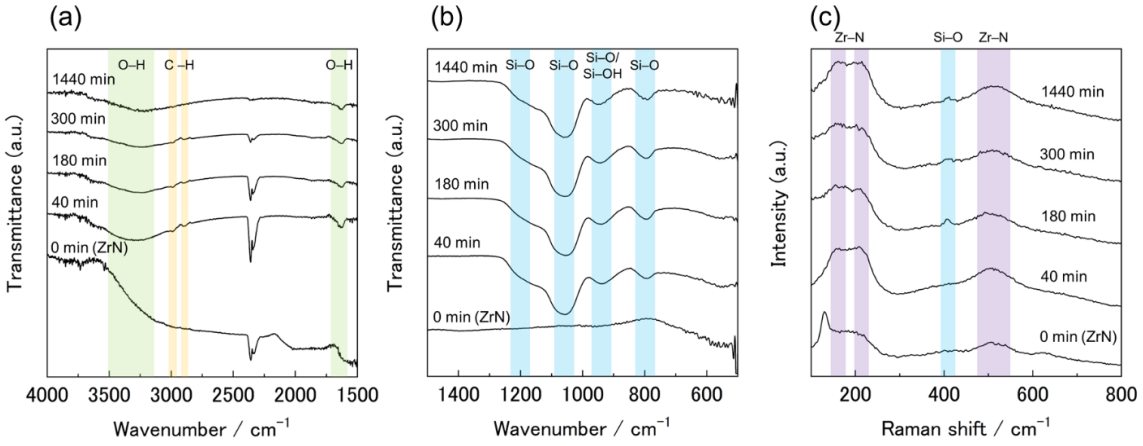

Figure 2. 10 FTIR spectra of the particles produced at the reaction times of 0 min, 40 min, 180 min, 300 min, and 1440 min: **(a)** the 4000–1500 cm^{-1} range and **(b)** the 1500–500 cm^{-1} range. Absorption at approximately 2300 cm^{-1}, attributed to atmospheric CO_2, was detected in all samples. **(c)** Raman spectra of the produced particles. FTIR bands: 3500 to 3200 cm^{-1} for O-H stretching, 2950 cm^{-1} for C-H stretching of the methyl group ($-CH_3$), 2850 cm^{-1} for C-H stretching of the methylene group ($-CH_2-$), and 1600 cm^{-1} for H-O-H bending of water. FTIR bands at 1200 cm^{-1}, 1070 cm^{-1}, 930 cm^{-1}, and 800 cm^{-1} correspond to the Si-O or Si-OH bonds. Raman bands at 160 cm^{-1}, 220 cm^{-1}, and 520 cm^{-1} corresponding to the Zr-N[206] are observed in all products. The band at 140 cm^{-1} corresponds to the acoustic modes of ZrN.[207] The 420 cm^{-1} band observed in products with reaction times of 180 min, 300 min, and 1440 min is assigned to the Si-O bond.[208] The formation of SiO_2 around the ZrN particles leads to a decrease in the scattering intensity of the acoustic modes of ZrN.

Energy-dispersive X-ray spectroscopy (EDS) was employed to determine the elemental composition more precisely across different areas of the particles. From **Figure 2.11.a,b**, the EDS line scan demonstrates a concentration of Zr predominantly in the core area and a concentration of Si in the shell region. This distinct elemental distribution suggested a core-shell structure, a conclusion further supported by TEM imaging, as displayed in **Figure 2.11.c**. The TEM images showed specific features consistent with a core-shell morphology. The electron diffraction patterns in **Figure 2.11.d** displayed distinct spots, indicating crystallinity within the particles. To further validate these findings and explore the specific phases present, XRD was conducted on the synthesized particles. XRD measurements, as illustrated in **Figure 2.11.e**, showed the presence of the ZrN phase in particles synthesized after a reaction time of 1440 min. Collating the data from STEM-EDS and XRD, it can be concluded that the particles synthesized possess a ZrN core and an SiO_2 shell, designating them as ZrN-SiO_2 core-shell particles. The resonance wavelength of particles exhibiting LSPR is known to shift to longer wavelengths as the particle size increases. However, in the process of preparing core-shell particles in the present study, the change in the size of the ZrN particles themselves that exhibit LSPR was not observed. Therefore, I believe that there is no need to consider changes in the absorption wavelength due to changes in ZrN particle size. The absorption wavelength of ZrN nanoparticles due to LSPR is presumed to shift toward longer wavelengths when surrounded by SiO_2, compared to when dispersed in water. This shift is attributed to the dependence of the LSPR resonance wavelength on the dielectric constant of the surrounding medium. The relative permittivity of water is approximately 1.33, while that of SiO_2 is approximately 3.9. A higher dielectric constant tends to elongate the LSPR resonance wavelength of nanoparticles, as it more strongly suppresses the oscillations of electrons around the particle, resulting in resonance at lower energy (longer

wavelength).[209] Analyzing the LSPR effects in the submicron-sized core-shell particles fabricated in this study is challenging due to the dominant influence of overall particle scattering over absorption by the core's LSPR. However, as observed in the obtained images (**Figure 2.6**), specific wavelength range absorption leading to a purple coloration of the particles is confirmed for shell thicknesses up to 250 nm.

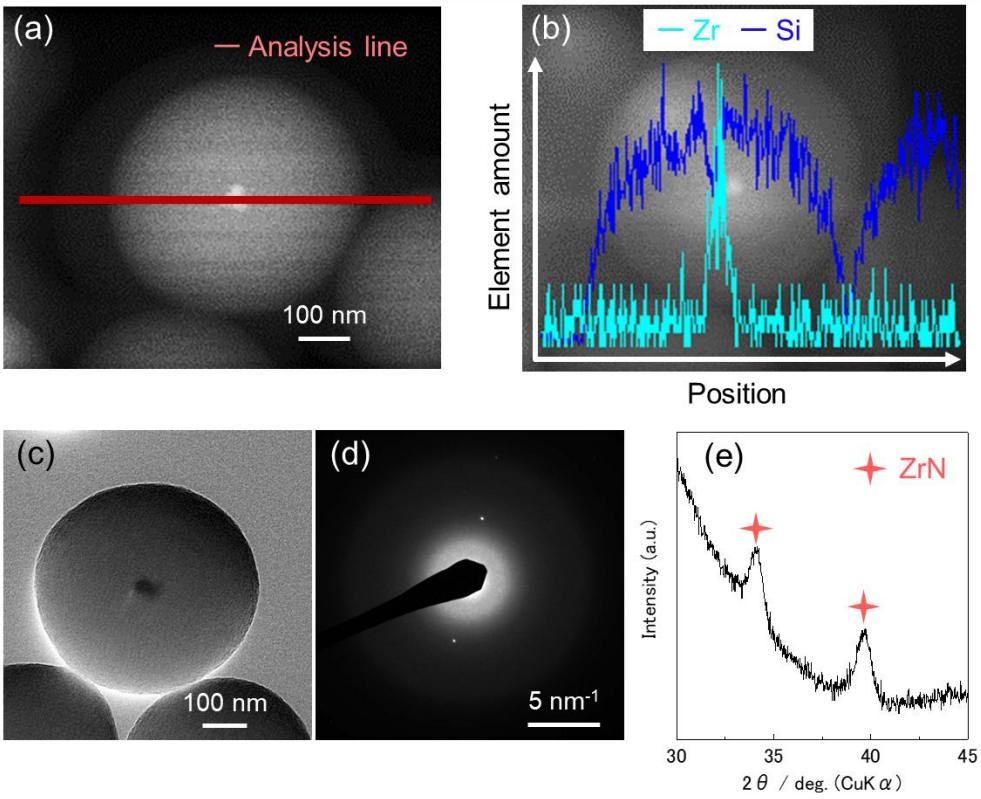

Figure 2. 11 STEM images and XRD profile of the products. **(a)** High-angle annular dark-field (HAADF) scanning transmission electron microscopy (STEM) image of products with highlighted energy-dispersive X-ray spectroscopy (EDS) analysis line. **(b)** Composition amount of the line across the particle. **(c)** Transmission electron microscopy (TEM) image of products. **(d)** Electron diffraction image of products. **(e)** X-ray diffraction (XRD) profile of the products.

The obtained ZrN-SiO_2 core-shell particles were stacked on a glass substrate by the layer-by-layer method using a poly(diallyl dimethylammonium chloride) (PDDA) solution. The layers of particles were formed on the surface of the substrate. Particle-stacked films comprising ZrN-SiO_2 core-shell particles were obtained (**Figure 2.12**). The thickness of the particle-stacked film was approximately 2 μm (**Figure 2.13**). The optical characteristics of the particle-stacked films of the obtained particles were assessed using reflection spectra.

Figure 2.14 shows the reflection spectra of the particle-stacked films. In the case of the particle-stacked films containing ZrN-SiO_2 core-shell particles with diameters of 497, 628, and 715 nm, peaks appear at 542, 605, and 673 nm in the reflection spectra, respectively, as shown in **Figures 2.14.a,b**. The particle-stacked film composed of ZrN-SiO_2 core-shell particles with particle size 289 nm did not exhibit a clear peak. In every instance, a peak was observed at approximately 330 nm. A similar peak at this wavelength was also evident in the SiO_2 substrate alone. This consistent occurrence suggests that the origin of the peak can be attributed to the intrinsic properties of the SiO_2 substrate. **Table 2.1** shows the summary of particle size, coefficient of variation (CV) which means monodispersity, and peak positions of particle-staked film. The CV serves as a statistical metric to assess the homogeneity of particle size distributions. This is the standard deviation of the particle size distribution divided by the average particle diameter, and the lower the CV, the more uniform the particle size distribution. Conversely, a high CV indicates a large variation in particle size. In the reflection spectra derived from films stacked with particles, the observed maxima shift based on particle size. This shift suggests that these maxima indicate structural colors, arising from the strong reflection of specific wavelengths by periodic structures (i.e., Brag diffraction). However, the intensity is less than 10%, and the peaks are broad with large half-widths. The reason why the peaks with large

half-widths in the case of 497, 628, and 715 nm, and no obvious peak in the case of 289 nm appear is due to the low monodispersity of the particles. The CV is in the range of 8%–18% in the case of the particle obtained by this method. This result means that some kinds of the obtained particles have sufficient monodispersity to exhibit a structural color but are insufficient to develop a clear color as a structural color material. However, it is of significance that I was able to demonstrate ZrN-SiO_2 core-shell particle show structural color. The ZrN-SiO_2 core-shell particles have the potential to be materials tuning the absorption and reflection spectra by the combination of LSPR and the periodic structure of components. Controlling absorption and reflection in narrower wavelength ranges requires more precise reaction control and improved particle monodispersity. More understanding of the reaction mechanism and adding ingredients such as surfactants to control the reaction should help achieve the ideal properties to tune the optical properties. I believe that ZrN-SiO_2 core-shell particles obtained by coating with SiO_2 via a liquid-phase process can be a significant material for optical applications.

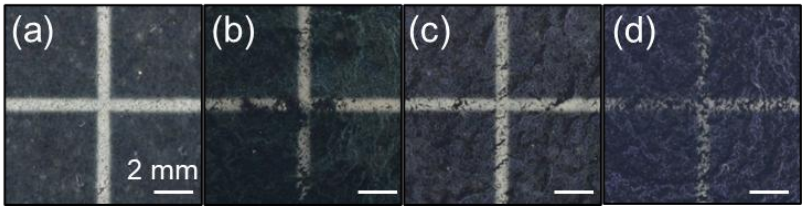

Figure 2. 12 Photographs of the particle-stacked film consisting of ZrN-SiO_2 core-shell particles synthesized at reaction times of **(a)** 40 min, **(b)** 180 min, **(c)** 300 min, and **(d)** 1440 min.

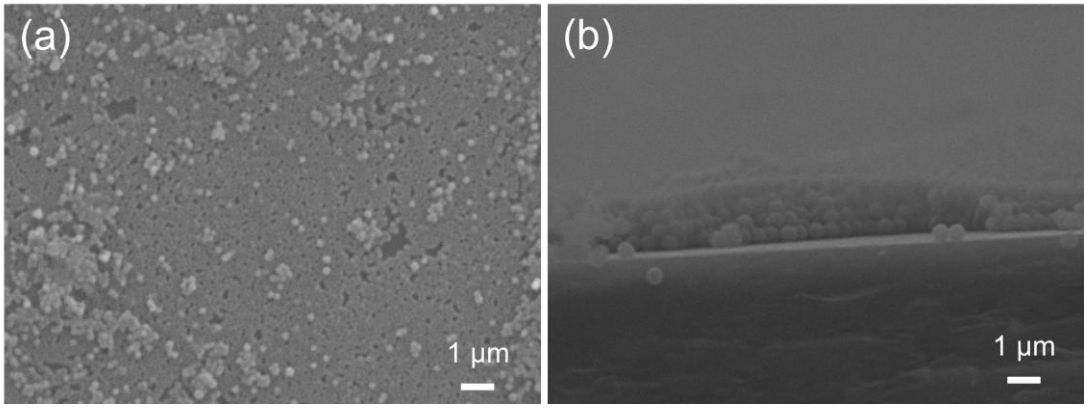

Figure 2. 13 (a) Surface SEM image and **(b)** cross-sectional SEM image of the prepared particle-stacked film.

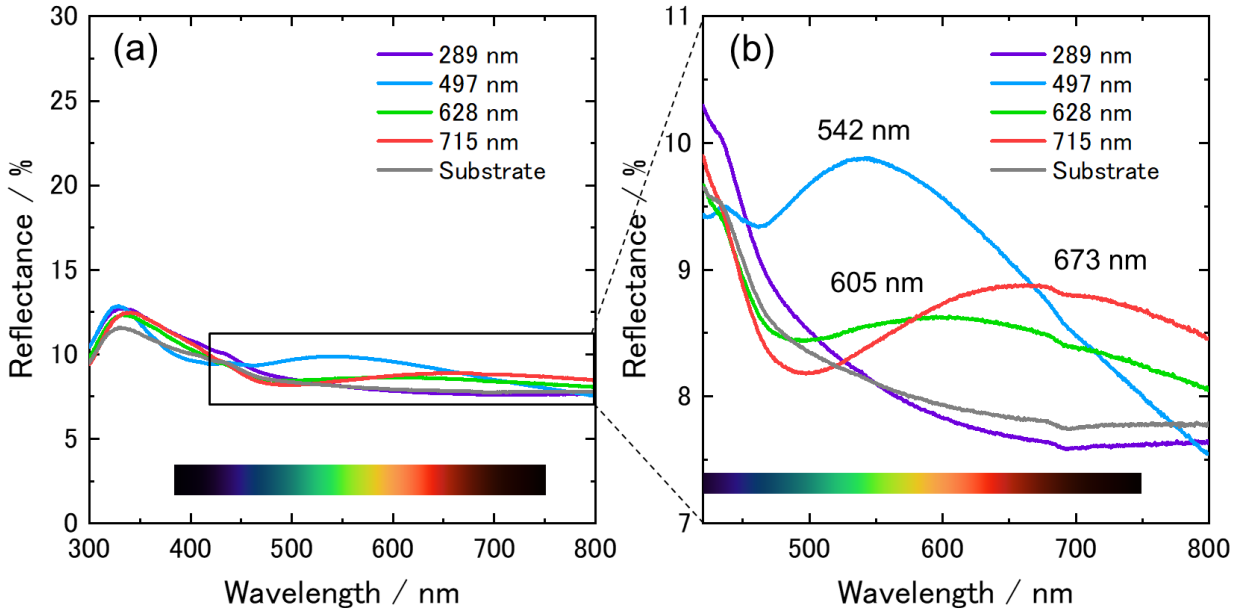

Figure 2. 14 Reflection spectra of the particle-stacked films composed of ZrN-SiO_2 core-shell particles **(a)** with diameters of 289, 497, 628, and 715 nm, and **(b)** its enlarged view.

Table 2. 1 Summary of particle sizes (average ± standard deviation), coefficient of variation (CV), and peak positions of particle-stacked films.

Reaction time / min	Particle size / nm	CV/%	Peak position / nm
40	289±49	17	–
180	497±91	18	542
300	628±84	13	605
1440	715±60	8	673

2.3 Conclusions

I successfully coated a SiO_2 layer through a sol-gel process on the ZrN nanoparticles to form ZrN-SiO_2 core-shell particles. An increase in the SiO_2 shell thickness was achieved by increasing the reaction time, enabling a shift in the structural color reflection toward a long wavelength in the range of 500–700 nm. I believe that the liquid-phase process is applicable to coatings with other nitrides exhibiting plasmon resonance, and offers color tuning by LSPR and controllable periodic structures. ZrN-SiO_2 core-shell particles whose SiO_2 shell thickness is controllable can be a significant material for optical application. However, the intensity at the maxima of the reflection spectrum is relatively weak, making it challenging to verify the plasmonic-photonic coupling effect. It was found that constructing a system with higher monodispersity is necessary for application as a structural color material.

2.4 Method

2.4.1 Materials

Zirconium dioxide (ZrO_2, 10 nm) was purchased from ITEC Co., Ltd. Magnesium nitride (Mg_3N_2) was purchased from Sigma-Aldrich. Tetraethoxysilane (TEOS) was purchased from Fluorochem Ltd. Ammonia solution (30 wt%) was purchased from KANTO CHEMICAL CO., INC. A PDDA solution (20 wt% in H_2O) was purchased from Sigma-Aldrich. Hydrochloric acid (1 M) was purchased from KANTO CHEMICAL Co., Inc.

2.4.2 Sample preparation

2.4.2.1 ZrN nanoparticle dispersion

ZrN nanoparticles were synthesized using a modified version of the process described by Karaballi et al.[163] A mixture of 1 g of zirconium dioxide nanopowder and a 3 molar excess of Mg_3N_2 powder was mixed using an agate mortar for 5 min in an Ar glove box. The resulting mixture was transferred to an alumina combustion boat and hermetically sealed in a plastic bag with a zip. The powder confined in the plastic bag was immediately inserted into a quartz tube and heated at 1000°C for 12 h under nitrogen gas flow in a tubular furnace. After natural cooling to room temperature, 0.2 g of the final product was transferred to a beaker and mixed with 25 mL of 1.0 M HCl solution. The mixture was sonicated for 20 min and 20 mL of water was added. After stirring for 1 h, the supernatant was separated by centrifugation for 1 h at 11 000 rpm. The residual precipitate was then redispersed in 5 mL of water by sonication and centrifuged for 15 min at 3300 rpm. The blue-colored supernatant was collected, and the precipitates were suspended in 5 mL of water by sonication. Finally, supernatants were collected. The ZrN concentration in the obtained dispersion was 0.03 wt%.

2.4.2.2 ZrN-SiO_2 core-shell nanoparticles

The ZrN nanoparticles were surface coated with amorphous silica shells using a sol-gel process. A dispersion of ZrN nanoparticles (0.03 wt%, 2 mL) was mixed with 10 mL of ethanol. Under continuous stirring, 0.3 mL of ammonia solution was added dropwise to the mixture. Subsequently, TEOS (0.1 mL) was added to the reaction mixture every 20 min until the final volume reached 1 mL. The reaction was allowed to proceed for 40–1440 min at room temperature with continuous stirring. The resulting particles were separated from the reaction medium by centrifugation at 3000 rpm for 15 min and resuspended in water.

2.4.2.3 Particle-stacked films

The obtained ZrN-SiO_2 core-shell particles were arrayed on a glass substrate using a layer-by-layer technique. The glass slides were submerged in a 1 wt% PDDA solution for 10 min, washed thoroughly by immersing them in water for 10 min, and dried using N_2 gas. The dried glass plates were then dipped into a 1 wt% suspension of ZrN-SiO_2 core-shell particles for 10 min. The plates were washed by immersing them in water again for 10 min and dried using N_2 gas. The immersion and emersion of the plates in the solution, dispersion, or water were conducted manually, without the use of any specialized equipment. This process was repeated five times to produce films comprising five layers of ZrN-SiO_2 core-shell particles.

2.4.3 Material characterization

2.4.3.1 X-ray diffraction

The crystalline phase was analyzed using an XRD diffractometer (Cu Kα, Mini-Flex 600, Rigaku). The diffraction angle 2θ was scanned in the range of 30–60° at a rate of 5° min^{-1}. XRD

profiles of the core-shell nanoparticles were acquired at a scanning rate of 1° min^{-1} to mitigate the impact of noise.

2.4.3.2 Transmission electron microscopy

The morphologies of the ZrN nanoparticles and core-shell nanoparticles were evaluated using TEM (JEM-2010, JEOL). The dispersions of ZrN nanoparticles and core-shell nanoparticles were drop-cast onto copper-mesh TEM grids. The acceleration voltage of the electron gun used for the observation was 200 kV.

2.4.3.3 Scanning transmission electron microscopy

The morphology of the core-shell particles was examined using STEM with an HD-2000 instrument (HITACHI). The sample was prepared following the same procedure as for the TEM observation, and the electron gun acceleration voltage was set at 200 kV. EDS was performed using the same equipment to investigate elemental distributions of the particles.

2.4.3.4 Small angle X-ray scattering

The particle size distribution of the ZrN nanoparticles in the dispersion was analyzed by SAXS using high-intensity X-ray-generating equipment (SmartLab; Rigaku). The incident X-rays had a wavelength of 1.54 Å. The ZrN dispersion was loaded into capillaries with diameter of 2.0 mm and exposed to X-rays. The scattered X-rays within the range of 0–2° were detected, and the SAXS profiles were obtained to determine the particle size distribution.

2.4.3.5 UV-vis absorption spectra measurement

The ultraviolet-visible (UV-VIS) absorption spectra of the ZrN nanoparticle dispersions were recorded using a V-700 spectrometer (JASCO). For these measurements, the obtained ZrN nanoparticle dispersion was diluted tenfold with water. The diluted dispersion was then placed in a 1 cm square quartz cell and mounted on a holder for measurement. Water was used as the background for absorbance measurements. The scanning rate was set at 200 nm min^{-1} and the bandwidth was 2 nm, with a range of wavelengths scanned from 300 to 800 nm. The reflection spectra of the particle-stacked films were measured using the same instrument, equipped with an integrating spherical unit. The particle-stacked films were placed on a holder for measurement, and the scanning rate was set at 200 nm min^{-1}, with a bandwidth of 5 nm and a range of wavelengths scanned from 300 to 800 nm. The incident light is illuminated at an angle of 5° from the vertical plane of the sample.

2.4.3.6 FTIR absorption spectra measurement

The FTIR absorption spectra of the ZrN nanoparticle and ZrN-SiO_2 core-shell particles were measured using an FT/IR-4700 (JASCO) equipped with an Attenuated Total Reflectance (ATR) accessory. Spectra were collected in the range of 4000–500 cm^{-1} with a resolution of 4 cm^{-1}, and each spectrum was obtained by averaging 32 scans to improve the signal-to-noise ratio. The samples were applied directly to the ATR crystal and gently pressed to ensure good contact. A background spectrum was recorded using a clean ATR crystal and was automatically subtracted from the sample spectra.

2.4.3.7 Raman spectra measurement

The Raman spectra of the samples were recorded using a Horiba XploRA Raman microscope (Horiba) equipped with a 532 nm laser. An attenuator filter was used to reduce the laser power to 0.1% at the sample to avoid sample damage. The spectra were collected in the range of 100–2600 cm^{-1} with a spectral resolution of 1 cm^{-1}. Each spectrum was obtained by accumulating 10 scans with an exposure time of 150 s per scan. The samples were placed on a glass slide and examined under a 100× objective lens.

Chapter 3 Synthesis of MN-SiO_2 Core-shell Particles (M=Ti, Hf) by a Sol-gel Process and Their Optical Property

3.1 Introduction

Core-shell particles are characterized by a distinct core material enclosed by a shell composed of another substance, allowing novel properties. Core-shell particles are extensively applicable in various fields, including catalysis,[51,174,183,187,210] and optical applications.[142,181,211–213] Inorganic core-shell particles, especially those containing metal nitrides, exhibit a range of functionalities due to their unique characteristics. For example, structures with ZrN or TiN as the core and graphene or silica as the shell were theoretically predicted to enable the tuning of the plasmonic resonance wavelength by adjusting the shell thickness, adjusting enhanced the sensitivity and the figure of merit for plasmonic sensing.[185] Additionally, cobalt-based nitride core oxide shell structures reported to exhibit high ORR activity.[187] The conductive nitride core contributed to conductivity, and the oxide shell provided active sites for the oxygen reduction reaction. Furthermore, incorporating ZrN-TiO_2 core-shell structures into dye-sensitized solar cells improved photoelectric conversion performance.[213] In the study, the LSPR properties of the ZrN core were utilized. Meanwhile, the TiO_2 shell served as a dye adsorption site, a charge separation interface, and a suppressor of ZrN particle aggregation, leading to enhanced photoelectric conversion efficiency.

Building on previous studies preparing ZrN-SiO_2 core-shell particles containing ZrN nanoparticles exhibiting LSPR,[214] this study explores the optical properties of core-shell particles using titanium nitride (TiN) and hafnium nitride (HfN) as the core materials. These materials were chosen due to their similar LSPR properties, as demonstrated by recent reports.[163] Due to differences in the dielectric constants of TiN, ZrN, and HfN, the oscillation frequency of the

electrons varies, leading to changes in the wavelength at which the nanoparticles exhibit the strongest light absorption LSPR peak. This research aimed to investigate the effect of these nitrides in combination with silica shells, assessing the implications for optical applications. The methodology involves the synthesis of TiN and HfN nanoparticles exhibiting LSPRs, followed by preparing TiN-SiO_2 and HfN-SiO_2 core-shell particles using a sol-gel process,[72] the same technique used for ZrN-SiO_2. This approach aims to adjust the optical properties by strategically layering metal nitride cores with silica shells. By adjusting the thickness of the silica shell and the type of metal nitride core, I aim to tune the absorption wavelengths and use the particles as structural color materials.

The synthesis and optical evaluation of these core-shell particles aim to provide insights into their potential applications, particularly in enhancing the efficiency and functionality of optical devices and sensors. This study broadens the understanding of metal nitride-based core-shell particles.

3.2 Results and Discussion

The mixture of oxide precursor (TiO_2 or HfO_2) nanopowder and Mg_3N_2 powder was heated at 1000°C under nitrogen flow to obtain black products. **Figure 3.1** shows the X-ray diffraction (XRD) profiles of the products obtained from the reaction between MO_2 and Mg_3N_2. The products obtained after the reaction contained MN (M=Ti or Hf), MgO, and Mg_3N_2. MN and MgO were formed through the reaction of MO_2 with Mg_3N_2, while the residual Mg_3N_2 was due to an excess of 3 molar equivalents of Mg_3N_2 added to the oxide precursor, resulting in unreacted Mg_3N_2 remaining. The reaction of MO_2 and Mg_3N_2 forming metal nitride is as follows.[163]

$$6MO_2 + 4\ Mg_3N_2 \rightarrow 6MN + MgO + N_2, \text{ (M=Ti or Hf)}$$

The obtained dispersion of the products, which was washed in the HCl solution, was dark green in the case of using TiO_2 and dark blue in the case of using HfO_2, as shown in **Figure 3.2.a,e**. **Figure 3.3.a** and **Figure 3.3.b** show the XRD profiles of the washed products using TiO_2 and HfO_2 as oxide precursor (indicated as "before reaction") and the products by reaction with TEOS at reaction times of 1 h, 2 h, and 3 h. XRD profile of the products before reaction with TEOS exhibits peaks originating from the TiN or HfN phase. The result indicates that the washing process dissolved and removed the unreacted Mg_3N_2 and the formed MgO, while the insoluble TiN or HfN remained.

The MN-SiO_2 core-shell particles (M=Ti or Hf) were synthesized using the obtained TiN dispersions and HfN dispersions. The dark green or blue solution transformed to a white hue as the reaction proceeded (**Figure 3.2.b-d,f-h**). During this process, the solution did not undergo gelation and precipitation. After each reaction time, the particles were collected by centrifugation. **Figure 3.4** shows the photograph of dried powder of TiN nanoparticles and HfN nanoparticles and the dried powder from particles obtained by synthesis at each reaction time. The color of particles changed from black to light green in the case of using TiO_2 (**Figure 3.4.a-d**) or from black to light blue in the case of using HfO_2 (**Figure 3.4.e-h**). XRD measurements showed the presence of the TiN or HfN phase in particles synthesized at reaction time of 1 h, 2 h, and 3h. XRD profiles of particles synthesized at reaction time of 1 h, 2 h, and 3h showed halo patterns at 24°.

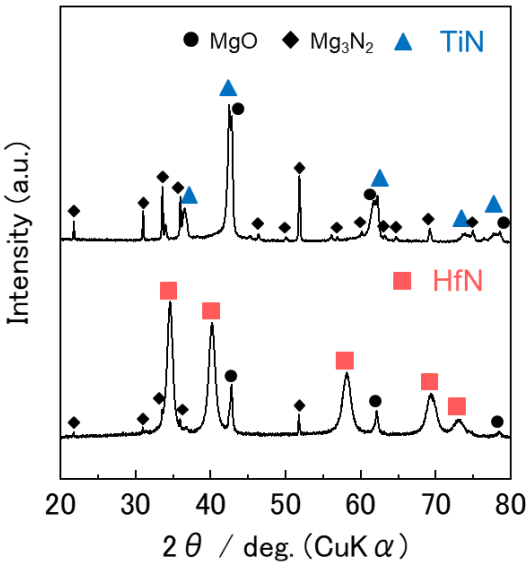

Figure 3. 1 XRD profiles of the products obtained from the reactions between MO_2 and Mg_3N_2, where M=Ti (top) and M=Hf (bottom).

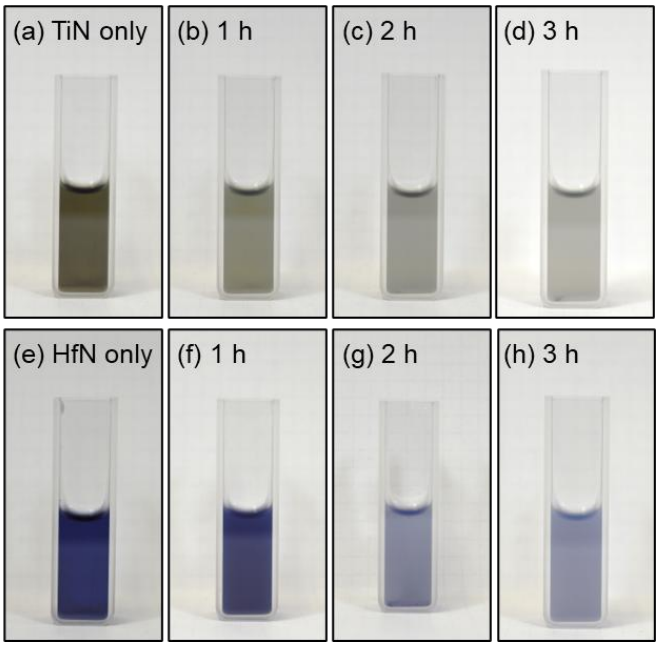

Figure 3. 2 Photograph of **(a)** the dispersion of the TiN nanoparticles, and the sols of the reaction times of **(b)** 1 h, **(c)** 2 h, and **(d)** 3 h. Photograph of **(e)** the dispersion of the HfN nanoparticles, and the sols of the reaction times of **(f)** 1 h, **(g)** 2 h, and **(h)** 3 h.

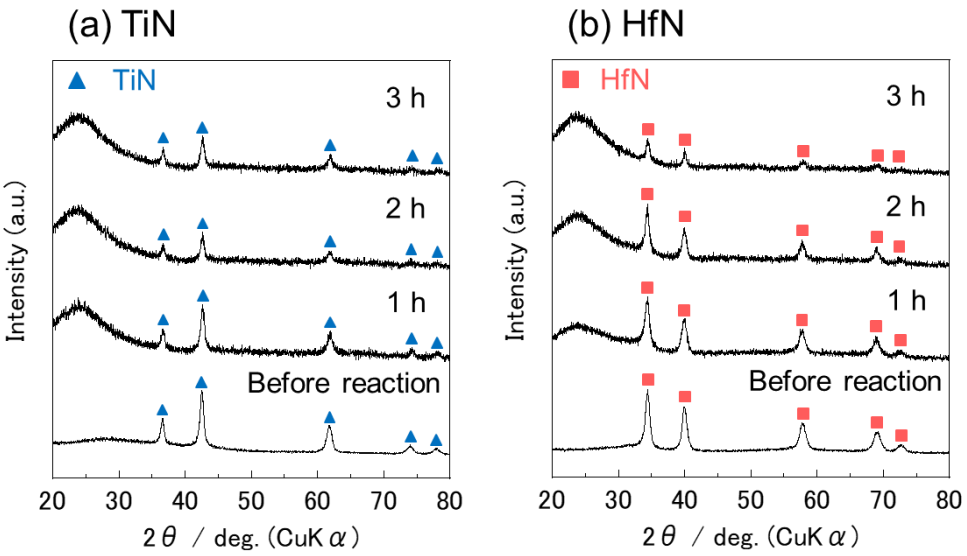

Figure 3. 3 (a) XRD profiles of the washed products using TiO_2 as oxide precursor (indicated as "before reaction") and the products at reaction times of 1 h, 2 h, and 3 h. **(b)** XRD profiles of the washed products using HfO_2 as oxide precursor (indicated as "before reaction") and the products at reaction times of 1 h, 2 h, and 3 h.

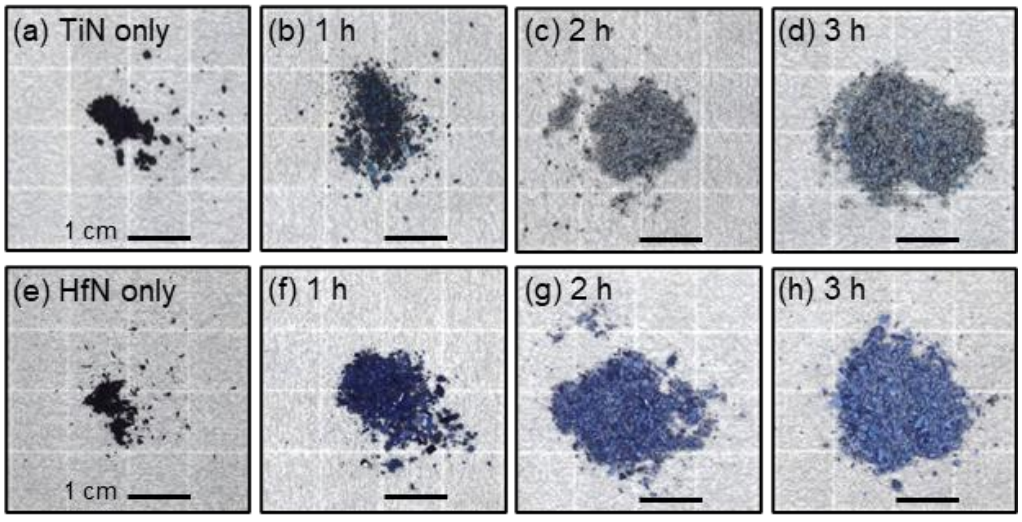

Figure 3. 4 (a) Photograph of dried powder of TiN nanoparticles and the dried powder from particles obtained by synthesis at reaction times of 1 h, 2 h, and 3 h. **(b)** Photograph of dried powder of HfN nanoparticles and the dried powder from particles obtained by synthesis at reaction times of 1 h, 2 h, and 3 h.

Subsequently, the morphology of the synthesized particles was examined using transmission electron microscopy (TEM) and scanning transmission electron microscopy (STEM). **Figure 3.5** shows the TEM images of prepared metal nitride nanoparticles and bright-field (BF) STEM images of the particles obtained at various reaction times (1 h, 2 h, and 3 h). TEM images showed that the particle size of synthesized TiN and HfN nanoparticles was 10-30 nm. Spherical particles with internal cores were observed at reaction times 1, 2, and 3 hours. However, there were also some particles without a core. The morphology of the core particles reflects the agglomeration state of the metal nitride nanoparticles. There were agglomerated metal nitride nanoparticles inside the shell.

The shell thickness was changed by varying the reaction time. Moreover, BF STEM images are obtained by detecting electrons that have passed through the sample. The BF STEM image contrast is primarily influenced by the amount of electron scattering, dependent on the element's atomic number. In these images, heavy atoms scatter more electrons and thus appear darker, while light atoms scatter fewer electrons and appear brighter. The BF STEM images in **Figure 3.5** show that the particle's core area appears darker than its shell area, suggesting a different atomic composition between the core and shell. These results confirmed that core-shell particles containing metal nitride core formed. However, particles that did not contain a metal nitride core were also produced, and some particles became distorted from a spherical shape due to the agglomeration of the core metal nitride nanoparticles. For particles to be used as components of structural color materials, they need to be spherical and have uniform sizes. Therefore, it was difficult to use the particles obtained as components of structural color materials.

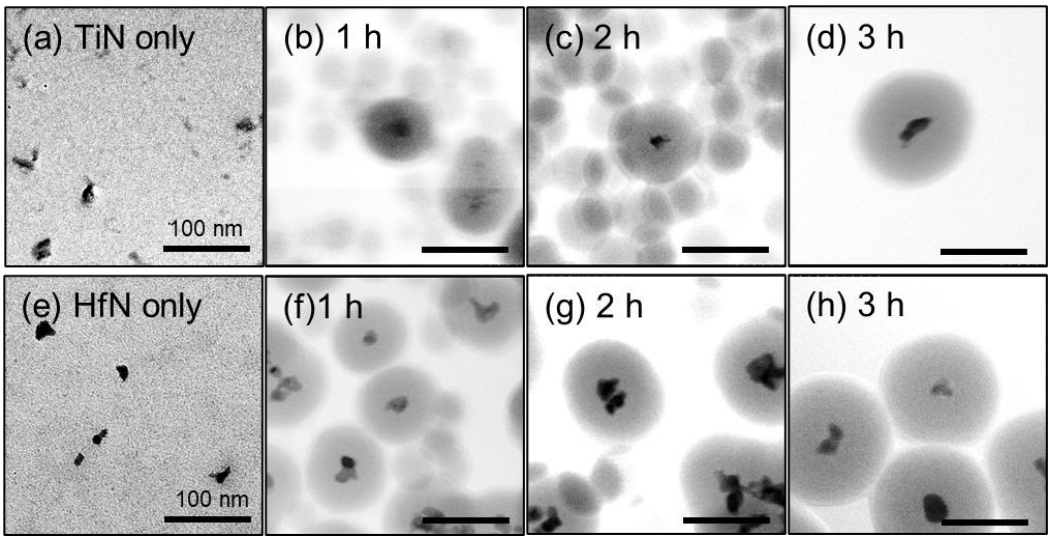

Figure 3. 5 (a) TEM micrographs of TiN nanoparticles and BF STEM micrographs of obtained particles at reaction times of 1 h, 2 h, and 3 h. **(b)** TEM micrographs of HfN nanoparticles and BF-STEM micrographs of obtained particles at reaction times of 1 h, 2 h, and 3 h.

To investigate the shell formation, Fourier transform infrared (FTIR) and Raman spectra of the products at designated reaction times were measured (**Figures 3.6** and **3.7**). The FTIR spectra at reaction times of 0 h, 1 h, 2h, and 3 h with the 1500–500 cm^{-1} range are displayed in **Figure 3.6**. **Figure 3.7** presents the Raman spectra of the products. FTIR spectra confirmed the formation of SiO_2 after 1 h, and the intensity of bands based on Si-O gradually increased with increased reaction time. These behaviors indicate that the SiO_2 network was formed with an increase in reaction time and consistent with the trends observed in **Figure 3.5**. These results suggested halo patterns observed at 24° in the XRD pattern (**Figure 3.3**) of the products after reaction time 1 h, 2 h, and 3 hours are attributable to amorphous SiO_2 that formed during the reaction. In the TiN system, the Raman spectra exhibited bands at 150 cm^{-1}, 180–220 cm^{-1}, 510–540 cm^{-1}, and 610–640 cm^{-1}, while in the HfN system, bands were observed at 130–160 cm^{-1}, 520–530 cm^{-1}, and

640–660 cm^{-1}. The sample before forming SiO_2 in the TiN system exhibited a sharp band at 150 cm^{-1} and a weak band at 610–640 cm^{-1}. After forming SiO_2, the Raman band at 150 cm^{-1} became broad and the band at 610–640 cm^{-1} was not observed. On the other hand, the relative strength of the band at 180–220 cm^{-1} and 510-540 cm^{-1} were higher. The Raman bands at 150 cm^{-1} and the bands at 610–640 cm^{-1} corresponded to Ti-O bonds,[215] the bands at 180-220 cm^{-1} and the bands at 510–540 cm^{-1} were assigned to the band of Ti-N.[216] However, the XRD profile of the sample before forming SiO_2 did not exhibit the peak corresponding to the TiO_2. From these results, it was possible that the surface of TiN was oxidized during Raman spectroscopy measurements, leading to the formation of Ti-O bonds. In this Raman scattering experiment, a 532 nm laser was used, and an attenuator filter was applied to reduce the laser power to 0.1% at the sample to avoid sample damage, with a scan time of 150 seconds. Although the laser intensity was reduced to 0.1% with the filter to minimize sample damage, the oxidation reaction could still have been accelerated during laser irradiation. As a result, TiN may have been oxidized to TiO_2, forming Ti-O bonds. In the sample after the formation of the SiO_2 shell, a peak corresponding to Ti-O bonds at 150 cm^{-1} was still observed, but the relative intensities of the peaks corresponding to Ti-N bonds at 180–220 cm^{-1} and 510–540 cm^{-1} were higher. This indicated that while the TiN core nanoparticles still underwent oxidation even after the formation of SiO_2, the TiN remained present. These results suggested that the formation of the SiO_2 shell inhibited the oxidation of the TiN core particles. In the HfN system, the major changes in the Raman spectra of the sample before forming the SiO_2 shell and after the reaction forming SiO_2 shell were not observed. The Raman spectra of the sample in HfN system exhibited the bands at 130–160 cm^{-1}, 520–540 cm^{-1}, and 640–660 cm^{-1}. These bands were assigned to the bonds of Hf-N.[217] This means the sample contained HfN at each reaction phase.

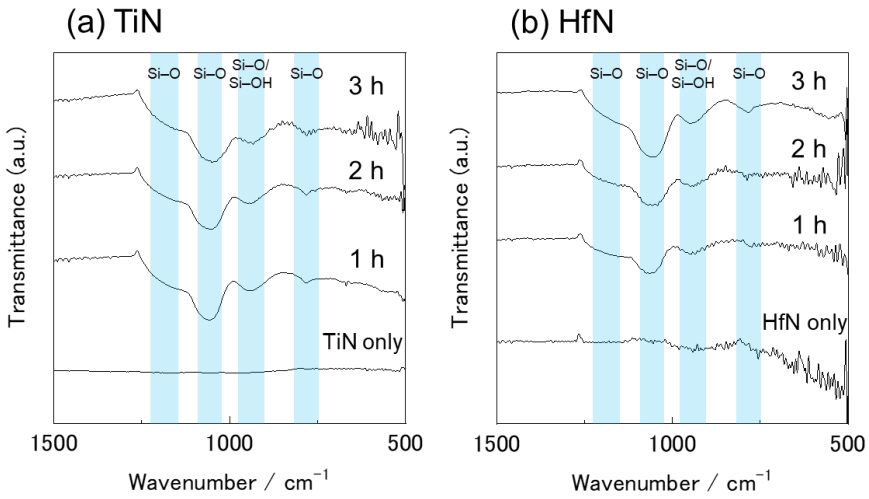

Figure 3. 6 FTIR spectra of the particles produced at the reaction times of 0 h, 1 h, 2 h, and 3 h. FTIR bands at 1200 cm^{-1}, 1070 cm^{-1}, 930 cm^{-1}, and 800 cm^{-1} correspond to the Si-O or Si-OH bonds.

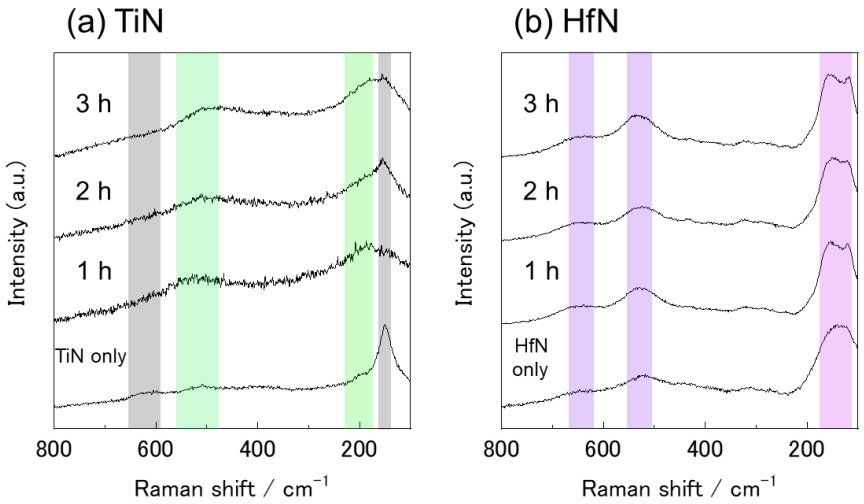

Figure 3. 7 Raman spectra of the produced particles at reaction times of 0 h, 1 h, 2 h, and 3 h. Raman bands at 150 cm^{-1} and bands at 610–640 cm^{-1} corresponded to Ti-O bonds.[215] Raman bands at 180–220 cm^{-1} are assigned to the transverse acoustic phonon of Ti-N bonds, and bands at 510–540 cm^{-1} are assigned to the optical band of Ti-N.[216] The 130–160 cm^{-1} band observed in products using HfN is assigned to the acoustic bond of Hf-N, and 520–540 cm^{-1} and 640–660 cm^{-1} are assigned to the optical bond of Hf-N.[217]

Energy-dispersive X-ray spectroscopy (EDS) was employed to determine the elemental composition more precisely across different areas of the particles as shown in **Figure 3.8.a,d**. The EDS line scan showed a concentration of Ti or Hf predominantly in the core area. This distinct elemental distribution suggests a core-shell structure, a conclusion further supported by TEM imaging, as displayed in **Figure 3.8.b,e**. The TEM images showed specific features consistent with a core-shell morphology. The electron diffraction patterns in **Figure 3.8.c,f** showed distinct spots, indicating crystallinity within the particles. Collating the data from STEM-EDS and XRD, it can be concluded that the particles synthesized possess an MN core (M=Ti or Hf) and a SiO_2 shell, designating them as MN-SiO_2 core-shell particles (M=Ti or Hf).

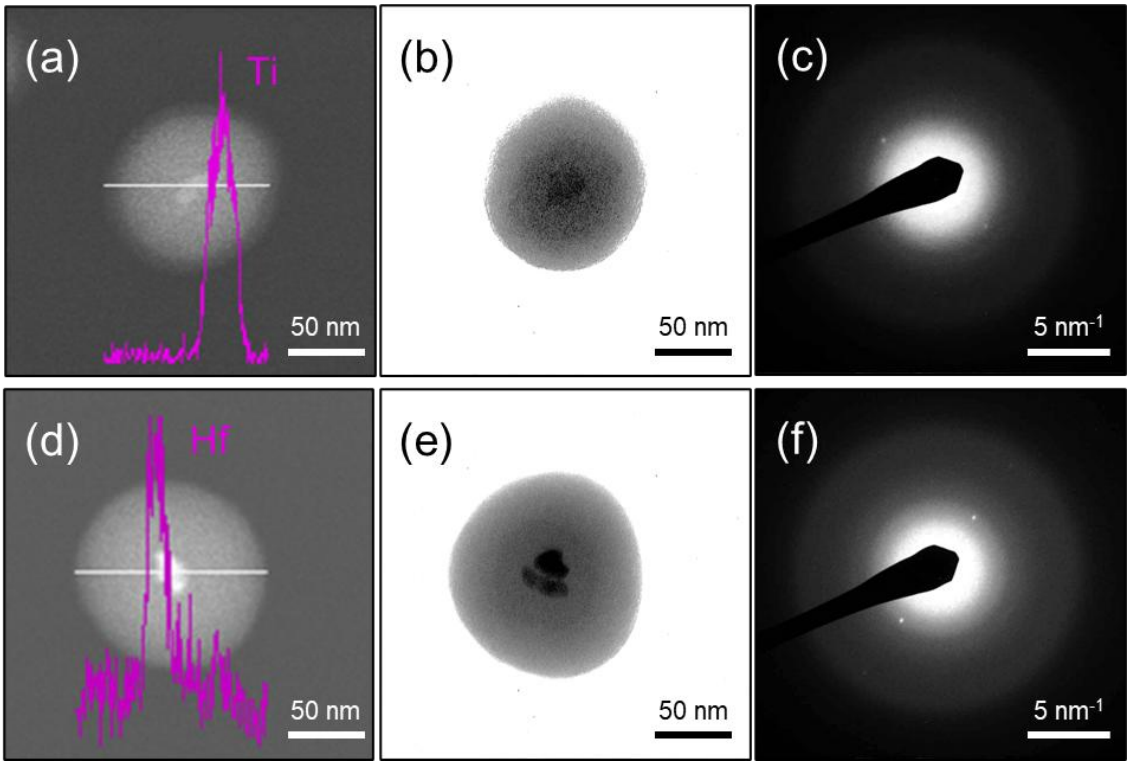

Figure 3. 8 (a) HAADF STEM image of the products using TiN nanoparticles with highlighted energy-dispersive X-ray spectroscopy (EDS) analysis line. **(b)** Transmission electron microscopy (TEM) image of the products using TiN nanoparticles. **(c)** Electron diffraction image of the products using TiN nanoparticles. **(d)** HAADF STEM image and EDS line scan of the products using HfN nanoparticle. **(e)** TEM image of the products using HfN nanoparticles. **(f)** Electron diffraction image of the products using HfN nanoparticles.

The absorption spectrum of the TiN nanoparticle dispersion and HfN nanoparticle dispersion respectively exhibits a peak at approximately 880 nm and 630 nm, as shown in **Figure 3.9**. For both TiN and HfN, the peak wavelength shifted to the shorter wavelength side after one hour of reaction time, and after that, the peak disappeared. The absorption wavelength of TiN and HfN nanoparticles due to LSPR is presumed to shift toward longer wavelengths when surrounded by SiO_2, compared to when dispersed in water for the same reasons as with the ZrN system. Indeed,

analyzing the LSPR effects in the submicron-sized core-shell particles fabricated in this study is challenging due to the dominant influence of overall particle scattering over absorption by the core's LSPR. However, as observed in the obtained images (**Figure 3.4**), specific wavelength range absorption leading to dark green and dark blue coloration of the particles is confirmed for TiN-SiO_2 core-shell particles and HfN-SiO_2 core-shell particles, respectively.

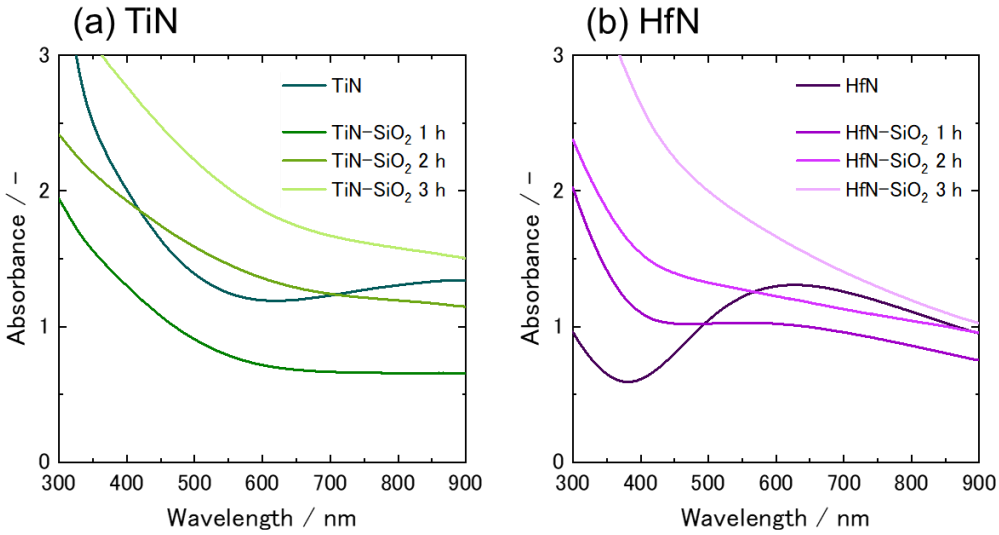

Figure 3. 9 Absorption spectra of the obtained particle dispersion at reaction times of 0 h, 1 h, 2 h, and 3 h.

The above results indicated that MN-SiO_2 core-shell particles were synthesized by liquid-phase synthesis of SiO_2 around MN nanoparticles (M=Ti or Hf), using TEOS as the raw material. Adjusting the reaction time controlled the thickness of the SiO_2 shell. Additionally, the formation of the SiO_2 shell was suggested to prevent the oxidation of the metal nitride nanoparticles.

3.3 Conclusion

TiN-SiO_2 and HfN-SiO_2 core-shell particles were fabricated by forming SiO_2 around TiN and HfN nanoparticles using the sol-gel method. The thickness of the SiO_2 shell tended to increase with reaction time; however, the morphology of the core-shell particles depended on the shape of the metal nitride core. However, it was not possible to synthesize only spherical metal nitride-SiO_2 core-shell particles suitable for use as structural color materials. Therefore, the strategy was altered in the next chapter by using SiO_2 particles as the core and adhering metal nitride nanoparticles, which absorb specific wavelengths range due to LSPR, around SiO_2 particles. Using highly monodisperse SiO_2 particles, the SiO_2-metal nitride core-shell particles exhibited both photonic effects due to the periodic structure and plasmonic effects from the surrounding metal nitride nanoparticles, aiming to evaluate these effects.

3.4 Method

3.4.1 Materials

Titanium dioxide (TiO_2, 5 nm) and Hafnium dioxide (61–81 nm) were purchased from US research Nanomaterials, Inc. Magnesium nitride (Mg_3N_2) was purchased from Sigma-Aldrich. Tetraethoxysilane (TEOS) was purchased from Fluorochem Ltd. Ammonia solution (30 wt%) was purchased from KANTO CHEMICAL CO., INC. A PDDA solution (20 wt% in H_2O) was purchased from Sigma-Aldrich. Hydrochloric acid (1 M) was purchased from KANTO CHEMICAL Co., Inc.

3.4.2 Sample preparation

3.4.2.1 MN nanoparticle dispersion (M=Ti or Hf)

MN nanoparticles were synthesized using a modified version of the process described by Karaballi et al.[163] A mixture of 1 g of metal oxide nanopowder and a 3 molar excess of Mg_3N_2 powder was mixed using an agate mortar for 5 min in an Ar glove box. The resulting mixture was transferred to an alumina combustion boat and hermetically sealed in a plastic bag with a zip. The powder confined in the plastic bag was immediately inserted into a quartz tube and heated at 1000°C for 12 h under nitrogen gas flow in a tubular furnace. After natural cooling to room temperature, 0.2 g of the final product was transferred to a beaker and mixed with 25 mL of 1.0 M HCl solution. The mixture was sonicated for 20 min and 20 mL of water was added. After stirring for 1 h, the supernatant was separated by centrifugation for 1 h at 11 000 rpm. The residual precipitate was then redispersed in 5 mL of water by sonication and centrifuged for 15 min at 3300 rpm. The colored supernatant was collected, and the precipitates were suspended in 5 mL of water by sonication. Finally, supernatants were collected.

3.4.2.2 MN-SiO_2 core-shell nanoparticles (M=Ti or Hf)

The metal nitride nanoparticles were surface coated with amorphous silica shells using a sol-gel process. A dispersion of metal nitride nanoparticles (2 mL) was mixed with 10 mL of ethanol. Under continuous stirring, 0.3 mL of ammonia solution was added dropwise to the mixture. Subsequently, TEOS (0.1 mL) was added to the reaction mixture every 20 min until the final volume reached 1 mL. The reaction was allowed to proceed for 0–3 h at room temperature with continuous stirring. The resulting particles were separated from the reaction medium by centrifugation at 3000 rpm for 15 min and resuspended in water.

3.4.3 Material characterization

3.4.3.1 X-ray diffraction

The crystalline phase was analyzed using an XRD diffractometer (Cu Kα, Mini-Flex 600, Rigaku). The diffraction angle 2θ was scanned in the range of 30–60° at a rate of 5° min^{-1}. XRD profiles of the core-shell nanoparticles were acquired at a scanning rate of 1° min^{-1} to mitigate the impact of noise.

3.4.3.2 Transmission electron microscopy

The morphologies of the metal nitride nanoparticles and core-shell nanoparticles were evaluated using TEM (JEM-2010, JEOL). The dispersions of metal nitride nanoparticles and core-shell nanoparticles were drop-cast onto copper-mesh TEM grids. The acceleration voltage of the electron gun used for the observation was 200 kV.

3.4.3.3 Scanning transmission electron microscopy

The morphology of the core-shell particles was examined using STEM with an HD-2000 instrument (HITACHI). The sample was prepared following the same procedure as for the TEM observation, and the electron gun acceleration voltage was set at 200 kV. EDS was performed using the same equipment to investigate elemental distributions of the particles.

3.4.3.4 FTIR absorption spectra measurement

The FTIR absorption spectra of the metal nitride nanoparticle and metal nitride-SiO_2 core-shell particles were measured using an FT/IR-4700 (JASCO) equipped with an Attenuated Total Reflectance (ATR) accessory. Spectra were collected in the range of 1500–500 cm^{-1} with a resolution of 4 cm^{-1}, and each spectrum was obtained by averaging 32 scans to improve the

signal-to-noise ratio. The samples were applied directly to the ATR crystal and gently pressed to ensure good contact. A background spectrum was recorded using a clean ATR crystal and was automatically subtracted from the sample spectra.

3.4.3.5 Raman spectra measurement

The Raman spectra of the samples were recorded using a Horiba XploRA Raman microscope (Horiba) equipped with a 532 nm laser. An attenuator filter was used to reduce the laser power to 0.1% at the sample to avoid sample damage. The spectra were collected in the range of 100–800 cm^{-1} with a spectral resolution of 1 cm^{-1}. Each spectrum was obtained by accumulating 10 scans with an exposure time of 150 s per scan. The samples were placed on a glass slide and examined under a 100× objective lens.

3.4.3.6 UV-vis absorption spectra measurement

The ultraviolet-visible (UV-VIS) absorption spectra of the metal nitride nanoparticle dispersions were recorded using a V-700 spectrometer (JASCO). For these measurements, the obtained metal nitride nanoparticle dispersion was diluted tenfold with water. The diluted dispersion was then placed in a 1 cm square quartz cell and mounted on a holder for measurement. Water was used as the background for absorbance measurements. The scanning rate was set at 200 nm min^{-1} and the bandwidth was 2 nm, with a range of wavelengths scanned from 300 to 900 nm.

Chapter 4 Structural Color Materials with Photonic-Plasmonic Coupling Effect Using Noble Metal-Free Plasmonic Particles in SiO_2-ZrN System

4.1 Introduction

Nanoparticles present a fascinating field of study, as they exist in a transitional range wherein materials exhibit both quantum and bulk properties. As particle size decreases, the bulk properties deteriorate owing to the emergence of discrete electronic states (quantum size effect) and increasing proportion of surface atoms. The characteristics exhibited by nanosizing are particularly evident in metal nanoparticles, in which unique electronic and magnetic properties have emerged, leading to novel applications in nonlinear optical switching,[218,219] catalysis,[220] and high-density information storage.[221] Similarly, semiconductor nanoparticles—commonly known as quantum dots[222]—display remarkable optical[223] and electrical[224,225] properties, attributed to the quantum confinement of electrons in a 3D space.

Recently, metal nitride nanoparticles have been investigated as alternatives for optical[226,227] and catalytic[228] functions—traditionally performed using precious metals such as Au, Ag, and Pt nanoparticles. Notably, group-four-element nitrides such as TiN, ZrN, and HfN was reported to exhibit LSPR[163]—a property harnessed to enhance applications in various fields. For instance, Exarhos et al. have demonstrated that the absorption wavelength of ZrN nanoparticles was tuned by coating them with silicon oxynitride.[191] ZrN-TiO_2 core-shell particles have been explored for performance enhancement in dye-sensitized solar cells.[213] ZrN-SiO_2 core-shell particles have been researched to improve the efficiency of lead-free perovskite solar cells.[192] In addition, the catalytic performances of metal nitrides were reported. In particular, ZrN nanocrystals have shown the potential to surpass the electrocatalytic efficiency of Pt in oxygen reduction reactions.[229] ZrN nanoparticles have also been examined as catalysts for methanol

oxidation[230] and water-splitting reactions.[231] Thus, metal nitride nanoparticles have emerged as viable substitutes for noble metal nanoparticles, offering comparable or enhanced chemical and physical functionalities.

I focused on integrating the LSPR properties of zirconium nitride into structurally colored materials. Structurally colored materials do not change color unless their microstructure is destroyed. Thus, the interest in the use of structural color materials for coloring, in which dyes or pigments are not used, is increasing. Structural coloration of materials is achieved through multilayer film interference,[60,232–234] interference from fine grooves and protrusions,[235] and scattering interference caused by microscopic particles.[236,237] Research on particle-based structural color has predominantly focused on synthesizable monodisperse particles, such as polystyrene[238,239] and SiO_2.[240–242] The mechanisms for expressing structural color based on particles can mainly be divided into colloidal photonic crystals and amorphous arrays. Colloidal photonic crystals are structures in which colloidal particles are periodically arranged. Because colloidal photonic crystals possess a complete periodic structure, they exhibit angle-dependent specific wavelength reflection due to Bragg diffraction. In contrast, amorphous arrays are structures with local periodic structures and exhibit noniridescent structural colors without angle dependence.[243] Enhancements in contrast and scattering suppression have been achieved by incorporating black particles, such as carbon black,[118,119] polydopamine,[121] or polypyrrole.[123] Additionally, Fe_2O_3-SiO_2 core-shell particles have been developed to combine the bandgap absorption of Fe_2O_3 with reflection at specific wavelengths owing to their periodic structures.[141] Similar approaches were reported for SiO_2-Au and SiO_2-Ag composite particles,[154,155] which utilize LSPR for specific wavelength range absorption in conjunction with periodic structure-based reflection, thereby providing an alternative to bandgap absorption.

However, the use of LSPR for specific wavelength range absorption in structurally colored materials remains relatively unexplored, particularly without the use of precious metals. In this study, I synthesized SiO_2-ZrN core-shell particles, where the ZrN nanoparticles exhibited LSPRs. ZrN nanoparticles were attached to SiO_2 cores using polyvinylpyrrolidone (PVP) modification, resulting in monodisperse SiO_2-ZrN core-shell particles capable of Bragg-diffracting light for structural coloration. SiO_2-ZrN core-shell particles produced a "photonic–plasmonic coupling effect," combining specific wavelength range absorption through LSPR by ZrN nanoparticles and diffraction owing to periodic structures without needing precious metals.

4.2 Results and Discussion

4.2.1 Preparation and Evaluation of SiO_2-ZrN Core-Shell particles

ZrN nanoparticles were synthesized via a solid-state metathesis reaction.[163] SiO_2 particles (150, 180, 210, 240, 270, and 300 nm) modified with polyvinylpyrrolidone-90 were mixed with the ZrN nanoparticle dispersion to obtain core–shell particles, as depicted in **Figure 4.1.a**. **Figure 4.1.b** shows a secondary electron (SE) scanning transmission electron microscopy (STEM) image of the obtained particles. The SE-STEM image shows that the nanoparticles were attached 3D around the large core particles. The attached nanoparticles appeared to exist as individual nanoparticles of ≈10 nm or as aggregates with a maximum size of ≈30 nm. The high-angle annular dark-field (HAADF)-STEM micrograph confirmed that nanoparticles were present only on the surface of the spherical particles (**Figure 4.2.a**). Indeed, the contrast of the HAADF-STEM image reflects the atomic weight in brighter areas containing heavier elements, meaning that large spherical particles are surrounded by compounds containing heavier atoms than those of the core particles. The bright-field (BF)-STEM micrograph (**Figure 4.2.b**) shows that the

nanoparticles were attached at the front of the spherical particles as well as at the back. **Figure 4.1.c** shows the absorption spectra of the ZrN particle aqueous dispersion and the aqueous dispersions of the obtained core-shell particles containing 150, 180, 210, 240, 270, and 300 nm SiO_2 particles as cores. The aqueous dispersion of the ZrN particles exhibited maximum absorption at 705 nm, while the aqueous dispersions of the obtained particles containing 150, 180, and 210 nm SiO_2 particles showed maximum absorption at 680, 668, and 661 nm, respectively. The X-ray diffraction (XRD) profile (**Figure 4.1.d**), the BF-STEM images of the obtained particles, energy-dispersive X-ray spectroscopy (EDS) mapping of the image (**Figure 4.1.e**), and transmission electron microscopy (TEM) and electron diffraction images (**Figure 4.1.f**) showed that the obtained particles contained ZrN as the shell. Since the ZrN nanoparticles remained adhered to the SiO_2 particles even after sample preparation for TEM, including ultrasonic dispersion in water, this demonstrated strong adhesion between the ZrN nanoparticles and SiO_2 particles. The absorption of the obtained aqueous particle dispersions containing 150, 180, and 210 nm (**Figure 4.1.c**) was attributed to ZrN nanoparticles; the obtained particles absorbed light in the 660–680 nm wavelength range through the attached ZrN nanoparticles. However, the obtained core-shell particles containing 240, 270, and 300 nm SiO_2 core particles and ZrN nanoparticles did not exhibit peaks in the absorption spectra because the influence of Mie scattering by SiO_2 core particles was greater than that of the absorption of ZrN particles attached to SiO_2 particles in the dispersion. The increase in particle size extends Mie scattering.[29] This results in a more significant influence of light loss due to scattering by Mie scattering than absorption by LSPR to exhibit no peak in the absorption spectra using 240, 270, and 300 nm SiO_2 core particles.

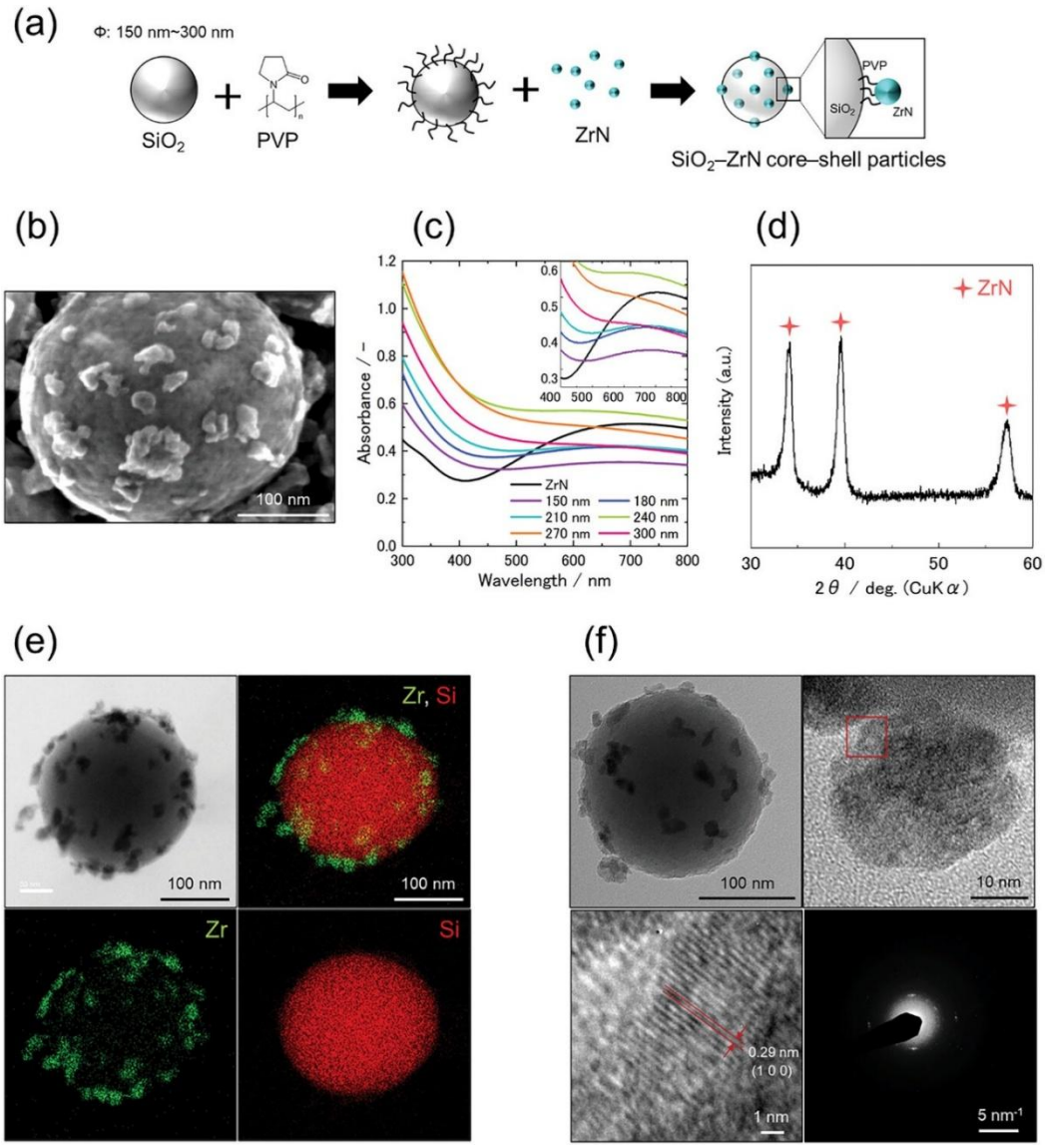

Figure 4. 1 (a) Schematic illustration of the preparation process of SiO_2-ZrN core-shell particles. **(b)** SE-STEM image of the obtained particle. **(c)** Absorption spectra of an aqueous dispersion of ZrN particles and the obtained core-shell particles containing 150, 180, 210, 240, 270, and 300 nm SiO_2 core particles. d) XRD pattern of the obtained particles. **(e)** BF-STEM image of the obtained particle and EDS mapping images highlighted by elements Zr and Si. **(f)** TEM images of the obtained particle and electron diffraction image: low magnification image, intermediate magnification image, and high magnification image of the area enclosed by the red square.

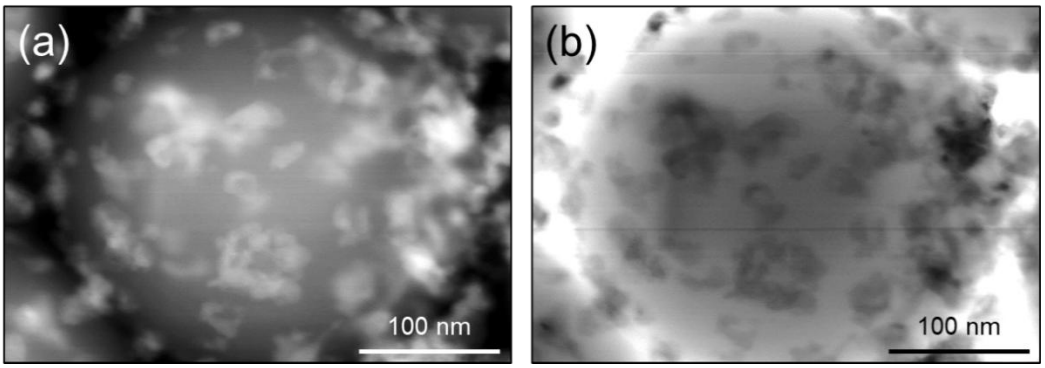

Figure 4. 2 (a) HAADF STEM micrograph and **(b)** BF STEM micrograph of one SiO_2-ZrN core-shell particle.

4.2.2 Optical Properties of Core-Shell Powders and Particle-Stacked Films

Figure 4.3 displays a photograph of the dried powder and BF-STEM images of the obtained SiO_2-ZrN core-shell particles. The BF-STEM images (**Figure 4.4**) showed that the ZrN nanoparticles were attached to the surface of the SiO_2 core particles of all sizes used, forming SiO_2-ZrN core-shell particles containing 150-300 nm of SiO_2 core. The obtained particle's size distribution (**Figure 4.5**) shows the high monodispersion of SiO_2-ZrN core-shell particle size enough to exhibit structural color since the ZrN nanoparticles were smaller compared to the core SiO_2 particles and did not significantly affect the overall diameter of the core-shell particles when attached to the surface of SiO_2. The powder of the obtained SiO_2-ZrN core-shell particles exhibited a color that depended on the particle size after drying at room temperature. The change in color depending on particle size indicated that the color originated from the aggregate structure of the particles.

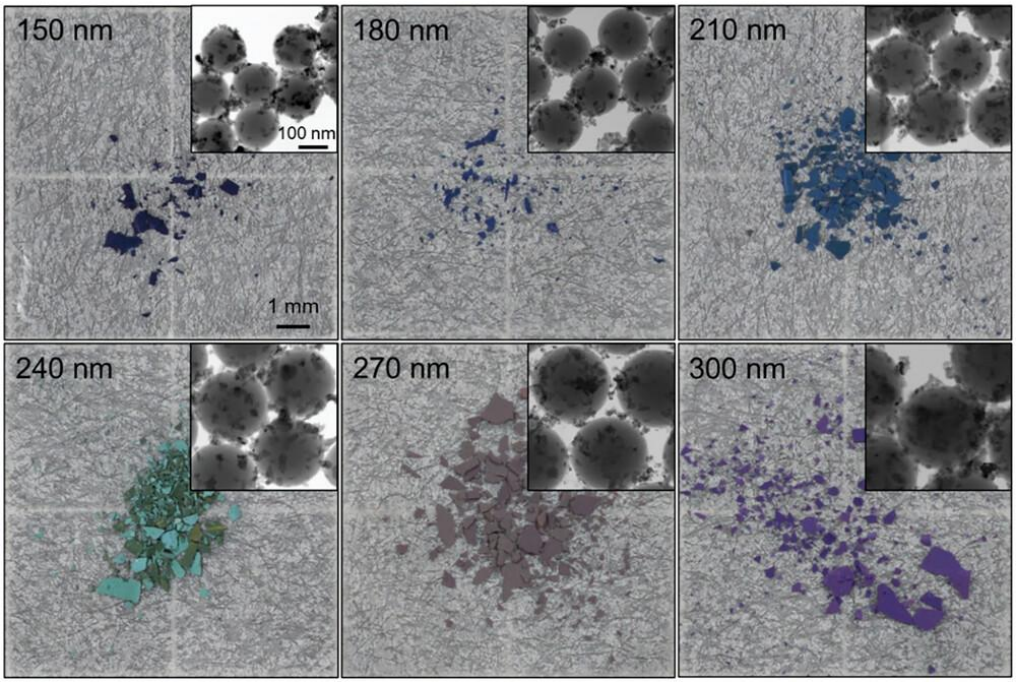

Figure 4. 3 Photographs of the obtained powder and BF-STEM images of the SiO_2-ZrN core-shell particles containing SiO_2 core particles of 150, 180, 210, 240, 270, and 300 nm.

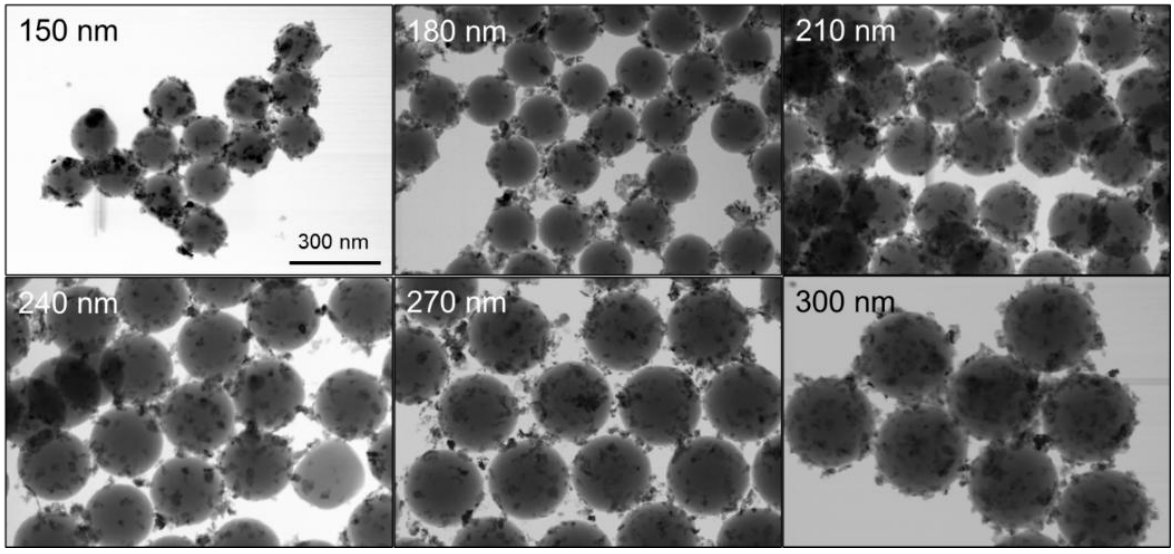

Figure 4. 4 BF STEM images of the SiO_2-ZrN core-shell particles containing SiO_2 core particles of 150, 180, 210, 240, 270, and 300 nm.

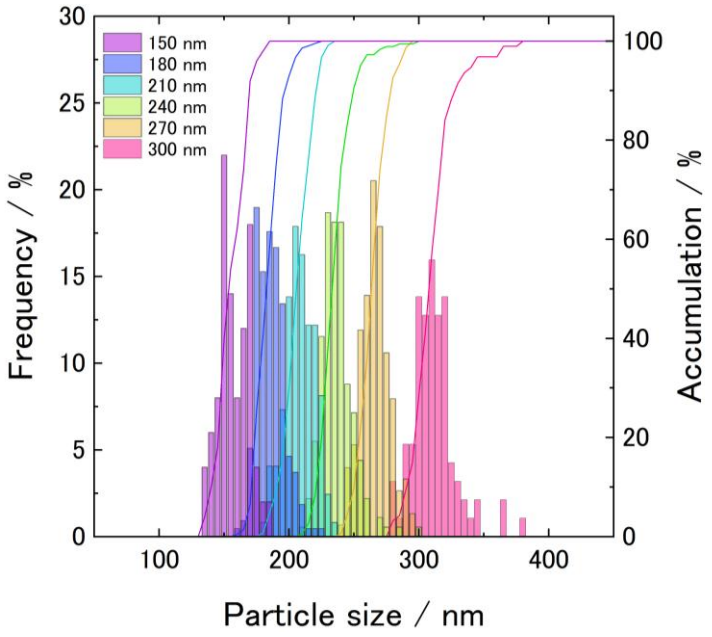

Figure 4. 5 The particle size distribution diagram of produced SiO_2-ZrN core-shell particles containing 150–300 nm SiO_2 particle as the core. The particle size distribution is derived from STEM images of produced SiO_2-ZrN core-shell particles. The Coefficient of Variation (CV) values, which indicate the monodispersity of the particles, for core particles with sizes of 150, 180, 210, 240, 270, and 300 nm are respectively 7.2, 5.7, 5.3, 5.3, 4.1, 5.5 %. The Coefficient of Variation (CV) values are derived by dividing the standard deviation of the particle size by the mean value.

Particle-stacked films with SiO_2-ZrN core-shell and SiO_2 particles were fabricated by a casting method using molds to compare the effects of ZrN nanoparticles. **Figure 4.6.a** shows photographs of the particle-stacked films with SiO_2-ZrN core-shell particles containing 150, 180, 210, 240, 270, and 300 nm core particles. To examine the angular dependence of the color of the particle-stacked film, images taken with the light source directed at 10° to the particle-stacked films and the camera rotated in 10° increments from 35° to 65° to the particle-stacked films are

also shown. **Figure 4.7.a** shows the results when SiO_2 particles were only used for particle-stacked film fabrication. Regardless of whether SiO_2-ZrN core-shell particles or SiO_2 particles were used as constituent substances, the color of the particle-stacked film changed depending on the size of the constituent particles, indicating that the color of the particle-stacked films was caused by the differences in particle size.

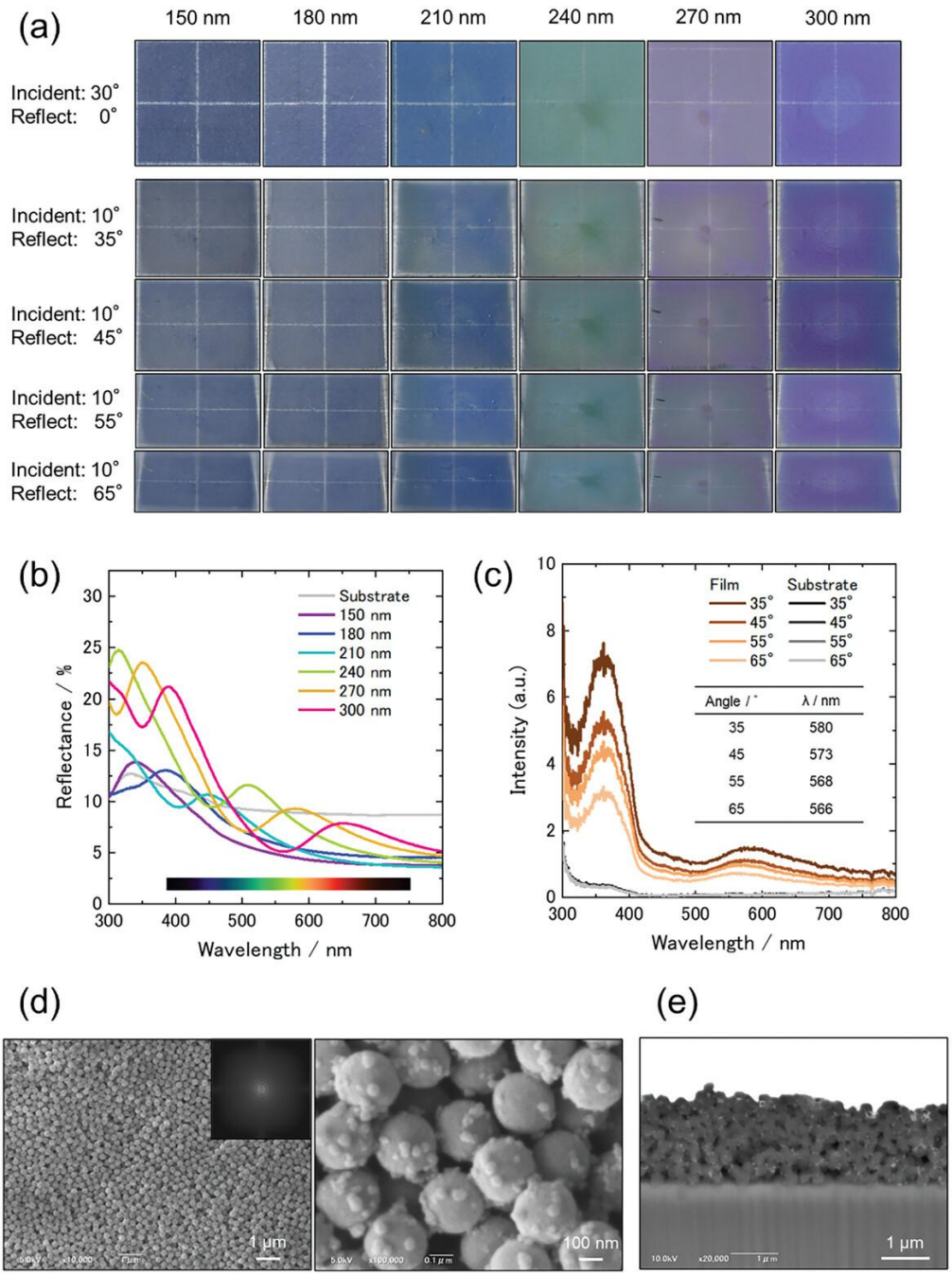

Figure 4. 6 (a) Photographs of the particle-stacked films comprising SiO_2-ZrN core-shell particles with SiO_2 core particles of 150, 180, 210, 240, 270, and 300 nm. These films were photographed on 5 mm graph paper; the cross lines in the images are grid lines of the background paper. The images show an area of 10 mm in length and 10 mm in width of the particle-stacked films. **(b)** Reflection spectra of the particle-stacked films composed of SiO_2-ZrN core-shell particles with core particles of 150–300 nm. The light was incident at 5° from the

vertical plane of the particle laminated film, with the reflected light detected with an integrating sphere unit. **(c)** Angular dependence of reflection spectra of particle-stacked films comprising SiO_2-ZrN core-shell particles with core particles of 270 nm. The reflectance intensity was measured to analyze angular dependence: the incident angle of the light source to the particle-stacked film was 10°, and the reflection angle to the detector was in 10° increments from 35° to 65°. **(d)** Surface FE-SEM images of particle-stacked films comprising SiO_2-ZrN core-shell particles with core particles of 270 nm and Fourier transform the image. **(e)** Cross-sectional FE-SEM images of particle-stacked films comprising SiO_2-ZrN core-shell particles with core particles of 270 nm.

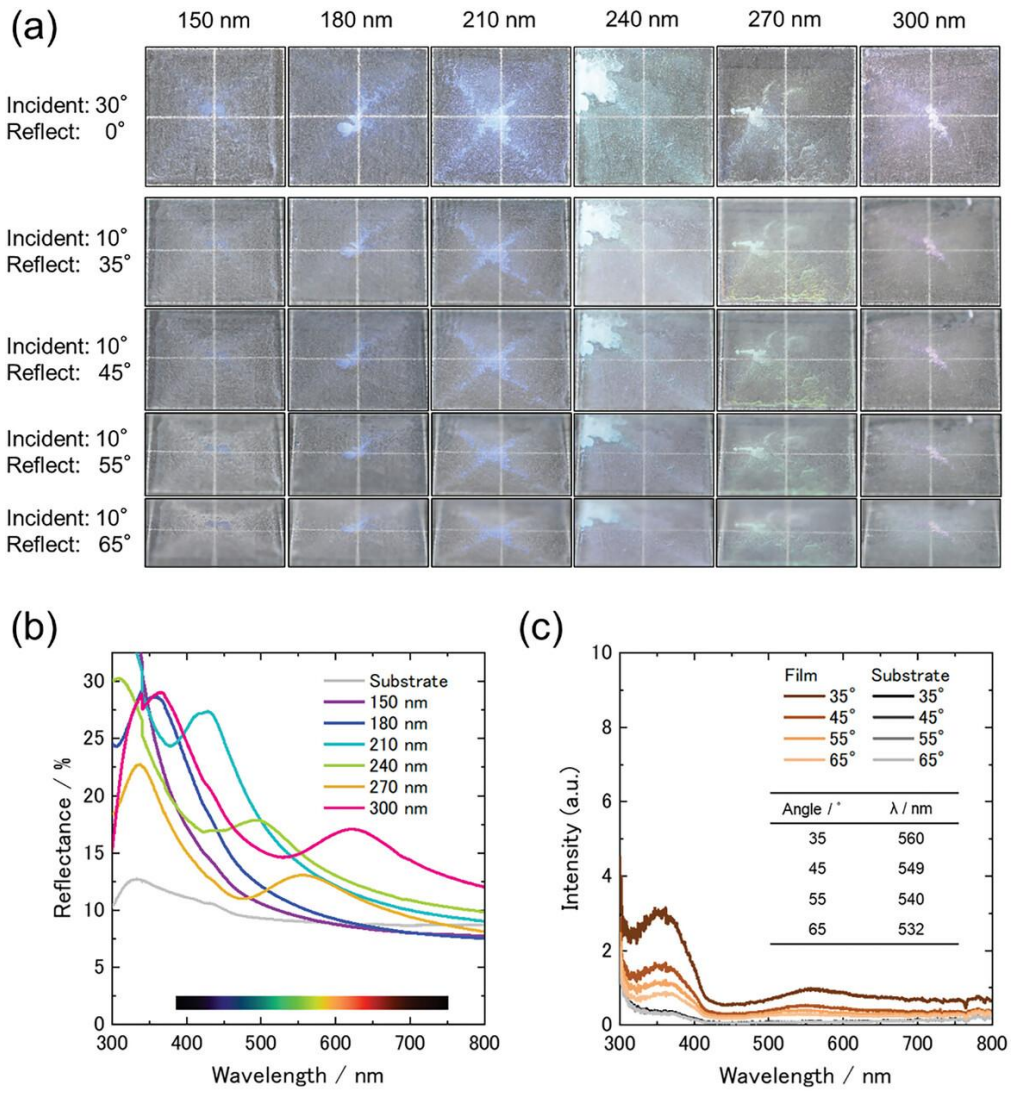

Figure 4. 7 (a) Photographs of the particle-stacked film comprising SiO_2 particles with diameters of 150, 180, 210, 240, 270, and 300 nm. These films were photographed on 5 mm graph paper; the cross lines in the images are grid lines of the background paper. The images show an area of 10 mm in length and 10 mm in width of the particle-stacked films. **(b)** Reflection spectra of the particle-stacked films composed of SiO_2 particles with diameters of 150–300 nm. The light was incident at 5° from the vertical plane of the particle laminated film, with the reflected light detected with an integrating sphere unit. **(c)** Angular dependence of reflection spectra of the particle-stacked films of SiO_2 particles with diameters of 270 nm. The reflectance intensity was measured to analyze angular dependence: the incident angle of the light source to the particle-stacked film was 10°, and the reflection angle to the detector was in 10° increments from 35° to 65°.

The optical characteristics of the particle-stacked films of the obtained particles were assessed using reflection spectra. **Figure 4.6.b** shows the reflection spectra of the stacked particles. In the case of the particle-stacked films containing SiO_2-ZrN core-shell particles with diameters of 150, 180, 210, 240, 270, and 300 nm, peaks were observed at 339, 385, 448, 506, 579, and 652 nm, respectively, in the reflection spectra. For the SiO_2-ZrN core-shell particles with diameters of 240, 270, and 300 nm, peaks at 314, 350, and 389 nm were observed on the short-wavelength side. The reflection of light within a photonic crystal follows Bragg's condition as follows:[243]

$$n\lambda = 2d\sin\theta \tag{40}$$

where n, λ, d, and θ represent the diffraction order (an integer), the wavelength of light, the lattice constant of the photonic crystal (the distance between adjacent layers), and the angle between the incident light and the normal to the layers of the photonic crystal, respectively. In amorphous arrays, the relatively broad reflection of specific wavelengths also occurs due to Bragg diffraction in the local periodic structure regions. Since the distance between layers (d) where Bragg diffraction occurs depends on the size of the particles, the wavelength (λ) of the reflected light is determined by the particle size. Therefore, the shift in the reflection peak toward longer wavelengths corresponds to an increase in the distance of the pitch in the periodic structure of the film. **Figure 4.7.b** shows the reflection spectra of particle films only from SiO_2. The particle-stacked films of SiO_2 particles with diameters of 150, 180, 210, 240, 270, and 300 nm exhibited peaks at 311, 356, 427, 492, 558, and 621 nm, respectively, in the reflection spectra. Similar to the SiO_2-ZrN core-shell particles, reflection peaks appeared on the short-wavelength side at 308, 337, and 369 nm when the particle sizes of the SiO_2 particle-stacked

films were 240, 270, and 300 nm, respectively. In the reflection spectra of the particle-stacked films, the appearance of maxima, which shifted depending on the particle size, signified that these maxima originated from structural colors, where periodic structures strongly reflected specific wavelengths. Although comparing the absolute value of the reflection intensity was impossible because the stacking state between the SiO_2-ZrN core-shell particles and SiO_2 particles was not the same, a difference in the reflection spectra was observed at ≈600 nm, corresponding to the ZrN nanoparticle absorption depending on the presence or absence of the ZrN nanoparticle shell. The reflection intensities of the particle-stacked films composed of SiO_2-ZrN core-shell particles were lower than those of the substrate films. In contrast, the reflection intensities of the particle-stacked films composed only of SiO_2 particles were higher than that of the substrate (**Figure 4.7.b**). This decrease in the reflection intensity was caused by absorption by the ZrN particles in the core.

When a structurally colored material is used as a colorant, a lower angular dependence of the visible color is desirable. Thus, the angular dependence of the reflection spectra of the particle-stacked films was evaluated. The angular dependence of the reflection spectra of the particle-stacked films composed of SiO_2-ZrN core-shell particles with core particles of 270 nm are shown in **Figure 4.6.c**, and those of only SiO_2 core particles of 270 nm are shown in **Figure 4.7.c**. Comparing the reflection spectra when changing the angle, the intensity of the SiO_2 particle-stacked film (**Figure 4.7.c**) was less than half that of the SiO_2-ZrN core-shell, although the reflection intensities of the SiO_2 particles were the same or higher than those of the SiO_2-ZrN core-shell when measured with an integrating sphere unit. Furthermore, when the angle changed from 35° to 65°, the maximum peak wavelength changed by 14 nm for the particle-stacked films composed of SiO_2-ZrN core-shell particles and 28 nm for the particle-stacked films consisting of

only SiO_2 particles. Even in the case of particle-stacked films with 240 and 300 nm particles, the shift was smaller for SiO_2-ZrN core-shell particles (**Figure 4.8** and **Figure 4.9**). These results suggested that the SiO_2-ZrN core-shell particles were stacked more randomly than the SiO_2 particles. The difference in the peak wavelength shift of the reflection spectrum between the SiO_2-ZrN core-shell particle-stacked film and SiO_2 particle-stacked film when the angle was altered by 30° was 14 nm, imperceptible to the naked eye. However, this result quantitatively demonstrated that the core-shell particle-stacked film exhibited less angular dependence than the silica particle-stacked film.

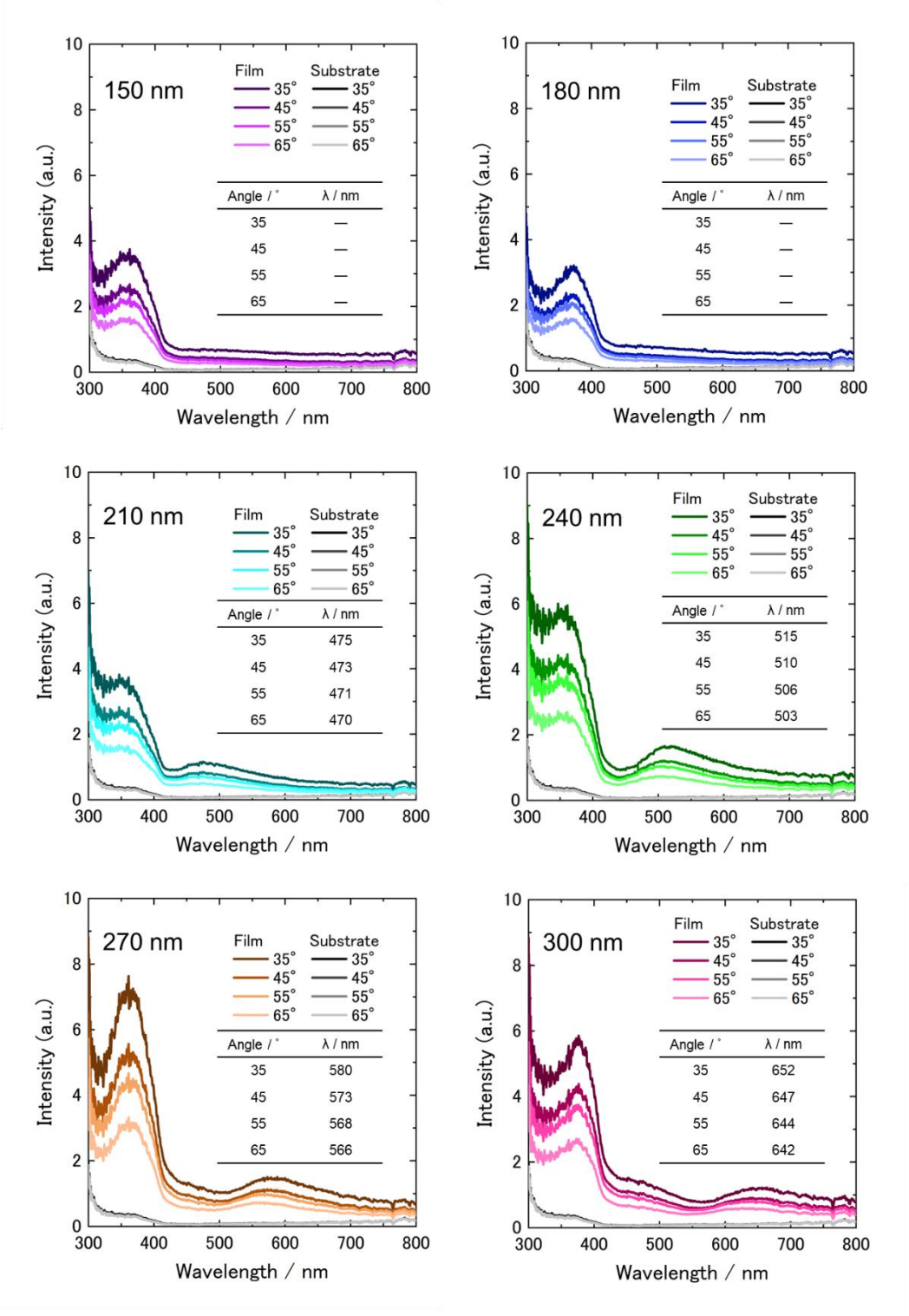

Figure 4. 8 Angular dependence of reflection spectra of particle-stacked films comprising SiO_2-ZrN core-shell particles with core particles of 150, 180, 210, 240, 270, and 300 nm.

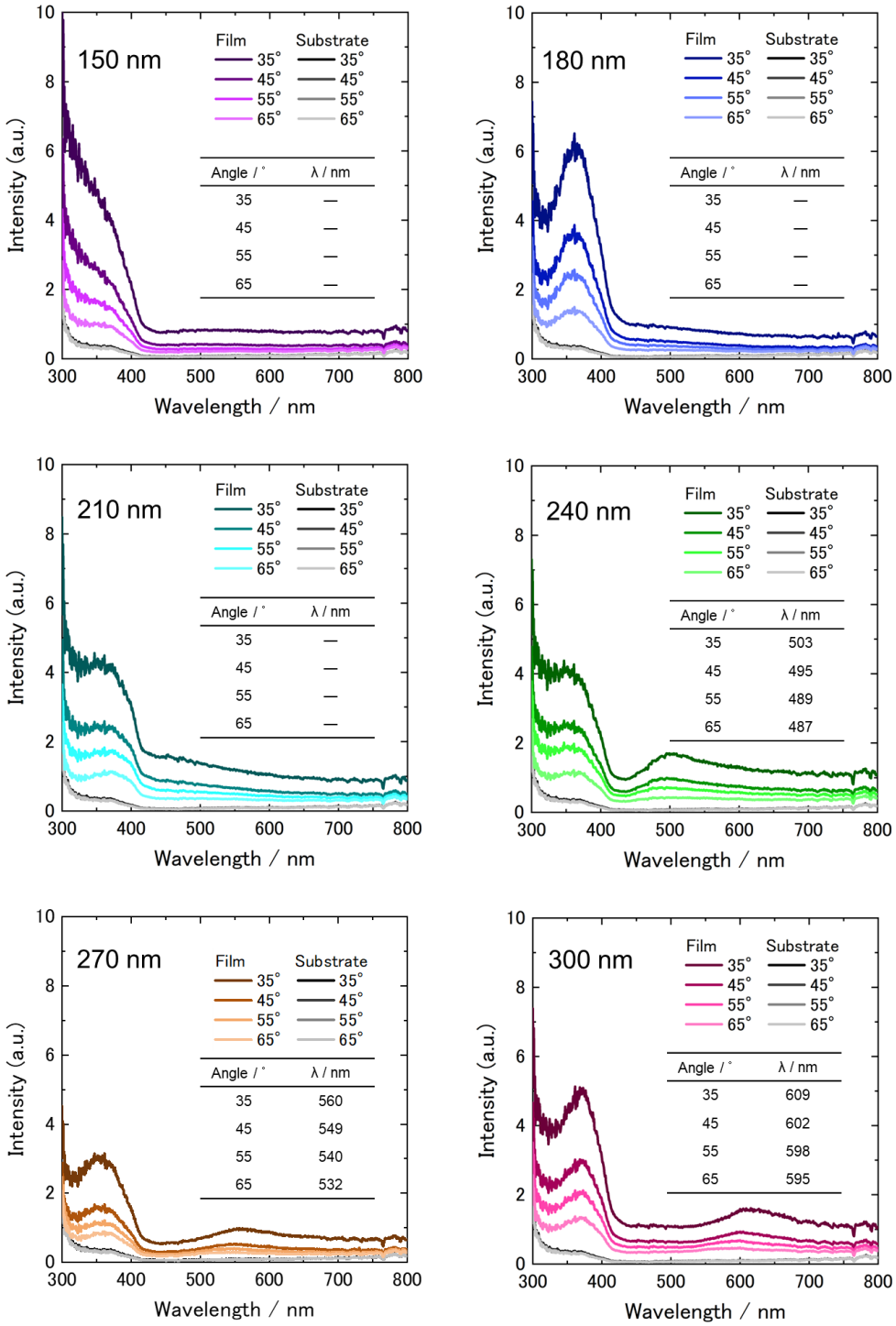

Figure 4. 9 Angular dependence of reflection spectra of particle-stacked films comprising SiO_2 particles with particle size of 150, 180, 210, 240, 270, and 300 nm.

The stacked particle films were observed using field-emission scanning electron microscopy (FE-SEM) to investigate the stacking state of the particles. **Figure 4.6.d,e** shows surface and cross-sectional FE-SEM images of the particle-stacked films. The surfaces of the particle-stacked films composed of SiO_2-ZrN core-shell particles were smoother than those of the SiO_2 particle-stacked films (**Figure 4.10**) because the particle-stacked films composed of SiO_2-ZrN core-shell particles had fewer irregularities made up of particle agglomerates than SiO_2, thus reflecting the differences in the state of particle film formation. Although no noticeable difference was observed in the surface images of the particle-stacked films at medium magnification, differences between the particle-stacked films composed of SiO_2-ZrN core-shell particles and SiO_2 particles were visible in the surface FE-SEM images at high magnification. Only spherical particles were observed in the SiO_2 particle stack (**Figure 4.11**), whereas protrusions on the particle surface were observed in the SiO_2-ZrN core-shell particles. These protrusions correspond to ZrN nanoparticles attached to SiO_2 core particles. The Fourier transform image of the surface of the SiO_2 particle-stacked film clearly exhibited rings derived from the periodic structure compared to the image of the surface of the particle-stacked film of SiO_2-ZrN core-shell particles. More distinct rings indicate higher periodicity of the constituent particles. Thus, the periodicity of the SiO_2-ZrN core-shell particles in the particle-stacked films was lower than that of the SiO_2 particle-stacked films, implying that the particle-stacked films of the SiO_2-ZrN core-shell particles had less angular dependence on reflection, consistent with the reflection spectrum results (**Figure 4.6.c**). From the cross-sectional FE-SEM images (**Figure 4.6.e**), no significant periodicity was observed in the height direction for both the particle-stacked films of the SiO_2-ZrN core-shell particles and SiO_2 particles (**Figure 4.12**). It was considered that there was no

significant difference in the monodispersity of the particle size distribution (**Figure 4.5**) and no major differences were observed in the stacked state for each particle size. In this study, quasi-amorphous structures were obtained. If a regularly arranged 3D SiO_2-ZrN core-shell microsphere photonic crystal is obtained, the peak in the reflection spectrum becomes narrower and the reflectance increases due to the regular arrangement, resulting in a relatively lower effect of specific wavelength range absorption by the ZrN shell particles' LSPR. Consequently, the influence of color based on reflection from the photonic crystals becomes more significant. The angle dependence of a photonic crystal is expected to be greater than that of the amorphous array obtained in this study.

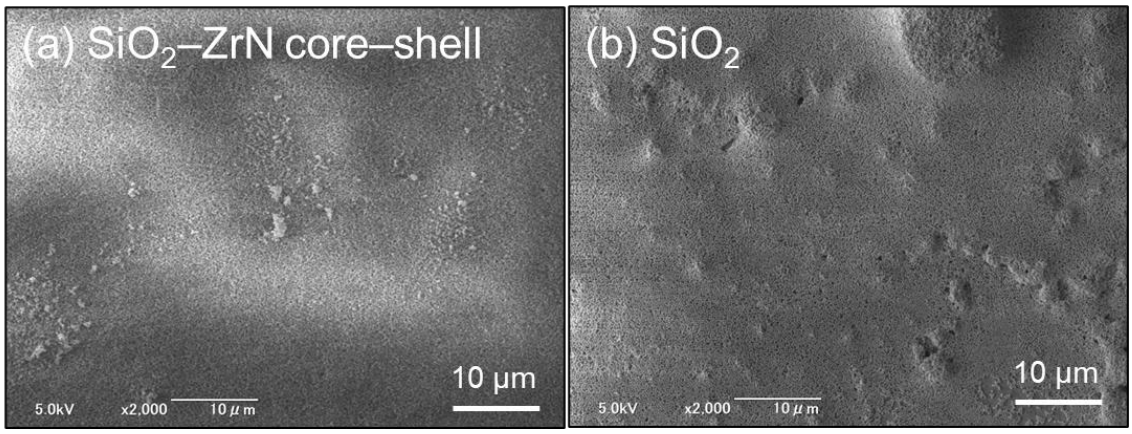

Figure 4. 10 The low magnification FE-SEM images of particle-stacked film surface. **(a)** The particle-stacked films are composed of SiO_2-ZrN core-shell particles with core particles of 270 nm, and **(b)** 270 nm SiO_2 particles.

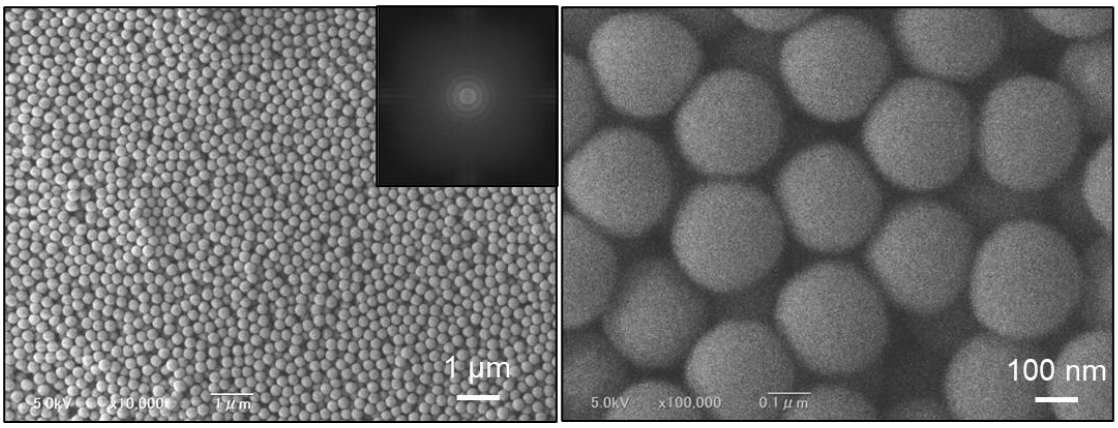

Figure 4. 11 The surface FE-SEM images of particle-stacked films composed of 270 nm SiO_2 particles and Fourier transform image.

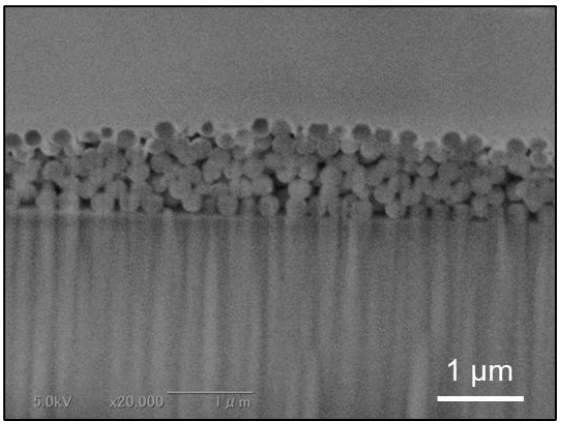

Figure 4. 12 Cross-sectional FE-SEM images of particle-stacked films composed of 270 nm SiO_2 particles.

Table 4.1 lists the maximum peaks, reflectance, and reflection intensity ratio ($R_l\ R_s^{-1}$) of the long-wavelength side (R_l) to the reflection intensity on the short-wavelength (R_s) side in the reflection spectra of particle-stacked films using SiO_2-ZrN core-shell particles and SiO_2 particles.

When comparing identical SiO_2 core particle sizes, the wavelength of the peak in the reflection spectrum of the SiO_2-ZrN core-shell particles shifted to longer wavelengths than that of the SiO_2 particles because the attachment of the ZrN particles increased the total particle size and widened the periodic interval. The reflection intensity ratio ($R_l R_s^{-1}$) of the particle-stacked films using SiO_2 particles is almost constant at 0.57–0.59 when the particle size was between 240 and 300 nm, while the ratio of SiO_2-ZrN core-shell particles decreased from 0.47 to 0.37. The prepared ZrN nanoparticles absorbed across the entire reflection band with a peak at 700 nm because the prepared ZrN nanoparticles were not completely uniform in size. As shown in **Figure 4.1.c**, the ZrN nanoparticles used in the shell exhibited a broad absorption spectrum with a peak at 700 nm. Therefore, it was considered that the fabricated SiO_2-ZrN core-shell particles also absorbed across the entire reflection band with a peak at 700 nm. The reflection intensity of the particle-stacked films using SiO_2-ZrN core-shell particles decreased as the reflection wavelength on the long-wavelength side approached 660–680 nm, corresponding to the absorption of ZrN, thus indicating that the reflection of particle-stacked films using SiO_2-ZrN core-shell particles was suppressed by the LSPR absorption of ZrN owing to the presence of ZrN particles around SiO_2. Thus, Particle-stacked films of SiO_2-ZrN core-shell particles exhibited photonic-plasmonic coupling effect. Particle-stacked films of SiO_2-ZrN core-shell particles with a high distribution density of ZrN nanoparticles (**Figure 4.13**), prepared by attaching ZrN nanoparticles to PVP-modified SiO_2 particles without washing, exhibited a more pronounced photonic-plasmonic coupling effect (**Figure 4.14**, **Table 4.2**). This suggested that the photonic-plasmonic coupling effect was tuned by the distribution density of ZrN nanoparticles in the shell. In addition, similar to how the peak of the reflection spectrum shifted with changes in the size of the core particles, a change in the shell thickness of core-shell particles is expected to change the

pitch of the periodic structure within the particle-stacked films, which may result in a shift in the peak wavelength of the reflectance spectrum.

Table 4. 1 Particle size (φ), wavelength of maximum peaks (λ), reflectance (*R*), and reflection intensity ratio ($R_l\ R_s^{-1}$) of the long wavelength side (R_l) to the reflection intensity on the short wavelength (R_s) side in the reflection spectrum of the particle-stacked films using SiO_2-ZrN core-shell particles and SiO_2 particles.

Type	**Φ / nm (core size)**	**λ / nm**	***R* / %**	$\boldsymbol{R_l\ R_s^{-1}}$ **/ –**
SiO_2-ZrN core-shell	150	339	13.84	–
	180	385	13.05	–
	210	448	10.67	–
	240	314, 509	24.77, 11.63	0.47
	270	350, 579	23.55, 9.32	0.40
	300	389, 652	21.21, 7.88	0.37
SiO_2 particles	150	311	40.09	–
	180	356	28.74	–
	210	427	27.37	–
	240	306, 485	31.31, 18.07	0.58
	270	337, 558	22. 74, 13.05	0.57
	300	369, 621	28.98, 17.10	0.59

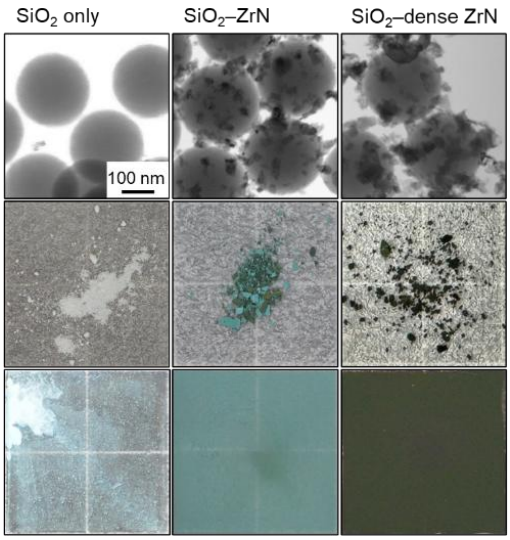

Figure 4. 13 BF-STEM images, photographs of the obtained powder, and photographs of the particle-stacked films are presented for the following samples: 240 nm SiO_2 particles, SiO_2-ZrN core-shell particles containing 240 nm SiO_2 particles as the core, and SiO_2-ZrN core-shell particles with a dense ZrN as shell and 240 nm SiO_2 particles as the core.

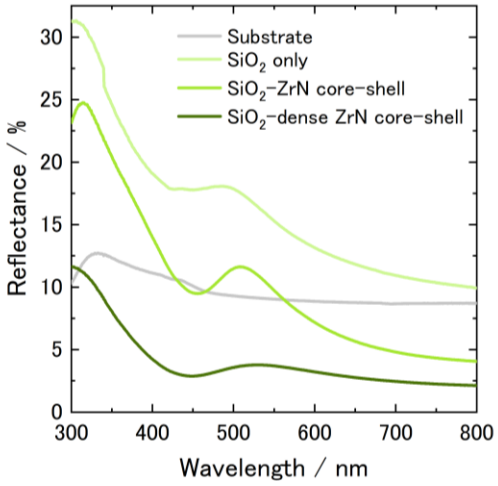

Figure 4. 14 Reflection spectra of the particle-stacked films composed of 240 nm SiO_2 particles, SiO_2-ZrN core-shell particles with core particles of 240 nm, and SiO_2-ZrN core-shell particles with a dense ZrN as shell and 240 nm SiO_2 particles as the core. The light was incident at 5° from the vertical plane of the film, with the reflected light detected with an integrating sphere unit.

Table 4. 2 Wavelength of maximum peaks of the short wavelength side (λ_s), wavelength of maximum peaks of the long wavelength side (λ_l), reflectance of the short wavelength side (R_s), reflectance of the short wavelength side (R_l), and reflection intensity ratio ($R_l\,R_s^{-1}$) of the long wavelength side (R_l) to the reflection intensity on the short wavelength (R_s) side in the reflection spectrum of the particle-stacked films using 240 nm SiO_2 particles, SiO_2-ZrN core-shell particles with core particles of 240 nm, and SiO_2-ZrN core-shell particles with a dense ZrN as shell and 240 nm SiO_2 particles as the core.

Type	λ_s **/ nm**	λ_l **/ nm**	R_s **/ %**	R_l **/ %**	$R_l\,R_s^{-1}$ **/ –**
SiO_2 only	306	485	31.31	18.07	0.58
SiO_2-ZrN core-shell	314	509	24.77	11.63	0.47
SiO_2– dense ZrN	301	530	12.92	4.20	0.33

I concluded that the synthesized core-shell particle stacked film exhibits the photonic–plasmonic coupling effect that combines photonic properties derived from the periodic structure and specific wavelength range absorption owing to LSPR. Hence, SiO_2-ZrN core-shell particles offer the potential to be effective optical materials for tuning reflection and absorption spectra owing to the combination of LSPR and the periodic structure of composites without precious metals.

4.3 Conclusion

I prepared SiO_2-ZrN core-shell particles. Color-controllable structural color materials were obtained by combining the LSPR of ZrN nanoparticles around SiO_2 core particles and the diffraction properties of periodic structures. The ZrN nanoparticles attached to the SiO_2 core absorbed the light approximately 700 nm, and SiO_2-ZrN core-shell particle-stacked films

exhibited reflection spectra with low angular dependence and a photonic–plasmonic coupling effect that combined specific wavelength range absorption through plasmon resonance and specific wavelength diffraction owing to the periodic structure. The change in the particle size enabled a shift in the structural color reflection, with the intensity of the reflection controlled by the particles as shell components. I believe that the SiO_2-ZrN core-shell particles offer the potential to be effective optical materials for tuning the reflection and absorption spectra, owing to the combination of LSPR and the periodic structure of the composites without precious metals.

4.4 Experimental Section

4.4.1 Materials

Zirconium dioxide (ZrO_2, 10 nm) was purchased from ITEC Co., Ltd. Magnesium nitride (Mg_3N_2) was purchased from Sigma Aldrich. SiO_2 particles were purchased from FUJI CHEMICAL Co., Ltd. Polyvinylpyrrolidone (PVP, K 90 Average Molecular weight. 360000) was purchased from TOKYO CHEMICAL INDUSTRY Co., Ltd. Hydrochloric acid (1 M) was purchased from KANTO CHEMICAL Co., Inc.

4.4.2 Sample Preparation

4.4.2.1 ZrN Nanoparticle Dispersion

ZrN nanoparticles were synthesized using a modified version of the process described in Chapter 2. A mixture of 1 g of zirconium dioxide nanopowder and a three-molar excess Mg_3N_2 powder was mixed for 5 min in an Ar glove box using an agate mortar. The resulting mixture was transferred to an alumina combustion boat and hermetically sealed in a plastic bag using a zip.

The powder confined in the plastic bag was immediately inserted into a quartz tube and heated at 1000 °C for 12 h under nitrogen gas flow in a tubular furnace. After natural cooling to room temperature, 0.2 g of the final product was transferred to a beaker and mixed with 25 mL of 1.0 m HCl solution. The mixture was sonicated for 20 min, and water (20 mL) was added. After stirring for 1 h, the supernatant was separated by centrifugation for 1 h at 11 000 rpm. The residual precipitate was redispersed in 5 mL of water by sonication and centrifuged for 15 min at 3300 rpm. The blue supernatant was collected to obtain a dispersion of the ZrN nanoparticles.

4.4.2.2 SiO_2-ZrN core-shell Particles

PVP 90 (0.1 g) was added to a water dispersion (50 mL) of SiO_2 particles (0.05 g) while stirring at 400 rpm. The mixture was continuously stirred for one night. Subsequently, the liquids were centrifuged at 3300 rpm for 15 min, with the supernatant discarded to remove the solution containing unattached PVP 90. The precipitate was resuspended in water (50 mL) and sonicated. The suspended liquid was centrifuged again at 3300 rpm for 15 min, with the supernatant discarded again. The residue was suspended in water (5 mL) to obtain SiO_2 particles modified with PVP 90. The ZrN dispersion (0.4 mL) was added to a 1 mL dispersion of modified SiO_2 particles. The mixture was then shaken and sonicated. The obtained dispersion was centrifuged at 3300 rpm for 15 min, with the supernatant discarded to remove the ZrN nanoparticles not attached to the SiO_2 particles. The residual precipitate was dried to obtain the SiO_2-ZrN core-shell particles.

4.4.2.3 Particle-Stacked Films

The obtained SiO_2-ZrN core-shell and SiO_2 particles were arrayed onto glass substrates by drop-casting using silicone molds. Silicone molds, with a thickness of 3 mm and a 1 cm square hole,

were pressed onto glass substrates and pasted. Nanoparticles' dispersion (0.1 wt.%, 0.3 mL) was cast into the hole of the silicon mold. After natural drying for one day, water as a dispersion medium evaporated, and the particles self-assembled to form a particle-stacked film.

4.4.3 Material Characterization

4.4.3.1 X-Ray Diffraction (XRD)

The crystalline phase was analyzed using an X-ray diffraction (XRD) diffractometer (Cu Ka, Mini-Flex 600, Rigaku, Japan). The diffraction angle 2θ was scanned in the range of 30–60° at a rate of $5°min^{-1}$.

4.4.3.2 Transmission Electron Microscopy (TEM)

The morphologies of the core-shell particles were evaluated using TEM (JEM-2010, JEOL, Japan), with the dispersion of the core-shell particles drop-cast onto copper-mesh TEM grids. The acceleration voltage of the electron gun used for the observation was 200 kV.

4.4.3.3 Scanning Transmission Electron Microscopy (STEM)

The morphology of the core-shell particles was examined using scanning transmission electron microscopy (STEM) with an HD-2000 instrument (HITACHI, Japan). The sample was prepared following the same procedure as that for the TEM observation, with the electron gun acceleration voltage set to 200 kV. Energy-dispersive X-ray spectroscopy (EDS) was performed using the same equipment to investigate the elemental distributions of the particles.

4.4.3.4 Field Emission Scanning Electron Microscope (FE-SEM)

The surface and cross-sectional morphologies of the particle-stacked films were observed using field-emission scanning electron microscopy (FE-SEM) with a JIB–4601F instrument (JEOL, Japan). The particle-stacked films were observed at an electron gun acceleration voltage of 200 kV after the films were coated with platinum. The observed cross-section was formed by the radiation of a focused ion beam onto the surface of the tungsten-coated particle-stacked film.

4.4.3.4 Spectrum Measurement

The UV–vis absorption spectra of the SiO_2-ZrN core-shell particle dispersions were recorded using a V-700 spectrometer (JASCO, Japan). The dispersion was then placed in a 1 cm square quartz cell and mounted on a holder for measurement. Water was used as the background for the absorbance measurements. The scanning rate was 200 nm min^{-1} and the bandwidth was 2 nm, with a range of wavelengths scanned from 300 to 800 nm. The reflection spectra of the particle-stacked films were measured using the same instrument equipped with an integrating spherical unit. The particle-stacked films were placed on a holder for measurement; the scanning rate was 200 nm min^{-1}, with a bandwidth of 5 nm and a range of wavelengths scanned from 300 to 800 nm. The reflectance intensity was measured to analyze the angular dependence. Variable-angle reflection measurement optics, C10027A10687 (Hamamatsu Photonics, Japan) were used to expose the particle-stacked films to white light and detect the reflected light. A xenon lamp was used as the light source to measure the reflection spectra. A photonic multichannel analyzer C10027 (Hamamatsu Photonics, Japan) was used to analyze the detected signals. The incident angle of the light source to the particle-stacked film was 10°, with the reflection angle to the detector varied in 10° increments from 35° to 65°.

Chapter 5 Photonic-Plasmonic Coupling Color Materials Using SiO_2-MN Core-shell Particles (M=Ti, Hf)

5.1 Introduction

Nature abounds with a vast array of colors, and throughout history, humanity has developed and utilized various techniques for coloring objects. Dyes and pigments are representative examples of such colorants. These technologies typically involve dissolving or dispersing chemical compounds that determine color through the absorption of light, either according to the structure's conjugated system or due to the energy absorption related to the compound's bandgap. However, organic dyes and pigments face challenges related to color longevity due to photodegradation under ultraviolet light. Inorganic pigments, while stable, sometimes contain metals that are harmful to human health, and the mining and refining of certain metals can lead to environmental and social issues. In response, recent research has focused on alternative techniques that generate colors through physical phenomena. Structural color materials, which utilize interference phenomena derived from periodic structures, show significant potential for enhancing color stability and reducing environmental impact. Structural colors arise from the interference of light by fine surface structures, are not reliant on specific chemicals, thus mitigating issues of fading associated with chemical colorants, and are environmentally benign. Moreover, structural color is widely observed in nature, such as in bird feathers and insect wings, and efforts are underway to mimic these natural structures to reproduce colors artificially.[244] Several types of structural color materials exist, ranging from those that utilize thin film interference to those with periodic microstructures and to those composed of periodically arranged particles. In the case of film-based structural colors, there were reports of structures consisting of stacked organic or inorganic thin films,[50,234] as well as lamellar

hydrogels.[60,232,233,245] For particle-based systems, structures filled with polymer particles like polystyrene,[238,239] hydrogel,[246] or inorganic particles such as silica[240–242] are used. However, these materials utilizing interference to those with periodic microstructures suffer from angle-dependent reflection spectra, making it difficult to achieve coloration independent of viewing angle. Introducing black materials such as carbon black,[118–120] polydopamine[121] polypyrrole,[123] or Fe_3O_4[124,125] into the matrix to suppress incoherent scattering and disrupt particle arrangement has developed particle-based structural color materials with reduced angle dependency.[247,248] Furthermore, photonic balls have been prepared by incorporating photonic structures into particle systems to reduce angle dependency.[249,250] Research in structural color materials has primarily focused on suppressing incoherent scattering by incorporating materials that absorb across the visible spectrum. More recently, advancements have been made in developing structural color materials that achieve selective control over reflection suppression by incorporating components that absorb specific wavelengths. In Fe_2O_3-SiO_2 core-shell particles, coloration is utilized that combines absorption derived from the Fe_2O_3 bandgap with reflection from the periodic structure.[141] Color control is also achieved by introducing particles exhibiting LSPR, a phenomenon where the collective oscillation of electrons on the particle surface occurs in response to an electric field, absorbing specific energies. LSPR is known to occur in nanoparticles of noble metals such as gold,[143,144] silver,[145,146] and palladium.[147,148] The introduction of these nanoparticles into particle-based structural color materials allows for tuned coloration,[153] and there are examples of using these photonic and plasmonic properties in catalytic materials.[135–140] However, these noble metals are costly due to their rarity and compete with uses in jewelry and electronic components. Therefore, to utilize plasmonic properties

without the use of precious metals, the materials incorporating ZrN nanoparticles as a plasmonic source into structural color materials were previously reported in the Chapter 4.[251]

While noble metals have traditionally dominated specific wavelength range absorption through LSPR in visible light, Reem A. Karaballi, Mita Dasog, and colleagues reported plasmonic properties in Group-4 metal nitride nanoparticles, prepared by solid-state metathesis reaction.[163] Previously, the metal nitrides were predominantly prepared by nitriding oxides under high-temperature conditions in an ammonia flow[252–255] or by plasma reactions in the gas phase[256–258]. However, the selection of reactive starting materials has enabled the synthesis of several metal nitrides through solid-state metathesis reactions without the need for ammonia gas or plasma reactors.[193,259] Metal nitrides have been highlighted as a new source of plasmons and as catalysts without the use of precious metals.[226,260–264] For instance, TiN has been researched as light-trapping plasmonic material in solar cells. [265,266] Meanwhile, ZrN-oxide core-shell particles have been researched to enhance the efficiency of solar cells.[192,213] Additionally, the synthesis process of ZrN-SiO_2 core-shell particles was reported.[214] It was proven that the absorption wavelength of ZrN nanoparticles can be tuned by coating them with silicon nitride, offering a process to control optical properties.[191] HfN-based nanoparticles have been researched as a novel multifunctional agent for photothermal therapy using plasmonic properties.[217] As catalysts, TiN was reported to be an efficient catalyst for hydrogen evolution reactions.[267] ZrN nanocrystals have shown the potential to surpass the electrocatalytic efficiency of Pt in oxygen reduction reactions.[229] ZrN nanoparticles have been considered as catalysts for methanol oxidation[230] and water-splitting reactions.[231] HfN nanoparticles were reported to be potential catalysts for electrocatalytic oxygen evolution reactions.[268] Thus, metal nitride nanoparticles have emerged as practical alternatives to noble metal nanoparticles, providing enhanced chemical and physical functionalities.

In the previous chapter, I showed SiO_2-ZrN core-shell particles demonstrating LSPR were synthesized, and SiO_2-ZrN core-shell particles produced a "photonic–plasmonic coupling effect" by combining specific wavelength range absorption through plasmon resonance with diffraction from periodic structures without the need for precious metals.[251] In this chapter, I have extended the range of metal nitride species to include TiN and HfN, preparing SiO_2-metal nitride core-shell particles that exhibit both photonic and plasmonic properties through a particle-stacked structure. This chapter aimed to confirm that by using metal nitride materials with different absorption wavelength regions, the color of SiO_2-MN core-shell particle-stacked films were controlled by varying the type of metal nitride. The TiN, ZrN, and HfN nanoparticles differ in their absorption wavelength ranges of LSPR, allowing the reflective spectrum to be tuned according to the metal nitride species incorporated. Additionally, the periodic structure changes with the size of the SiO_2 particles, altering the reflective spectrum according to particle size. I have developed materials that display a broad color spectrum by controlling the core particle size (photonic effect) and the type of metal nitride species adhered to (plasmonic effect). This material serves as a colorant showing diverse hues without relying on precious or hazardous heavy metals.

5.2 Results and Discussion

5.2.1 Preparation and Evaluation of SiO_2-TiN Core-shell Particles and SiO_2-HfN Core-shell Particles

TiN nanoparticles and HfN nanoparticles were synthesized via a solid-state metathesis reaction. XRD diffraction measurements confirmed the products TiN and HfN (**Figure 5.1**). The particle size of obtained TiN nanoparticles and HfN nanoparticles were approximately 10–20 nm and

10–40 nm, respectively (**Figure 5.2**). The dispersion of obtained TiN nanoparticles exhibited absorption at 830 nm, and that of HfN nanoparticles exhibited absorption at 610 nm (**Figure 5.3**). The absorption of metal nitride nanoparticles at specific wavelength ranges indicated that the obtained TiN nanoparticle and HfN nanoparticle showed plasmonic properties. SiO_2 particles (150, 180, 210, 240, 270, and 300 nm) modified with polyvinylpyrrolidone K90 (average molecular weight 360,000) were mixed with the TiN nanoparticle dispersion and HfN nanoparticle dispersion to obtain core-shell particles, as depicted in **Figure 5.4.a**. **Figure 5.4.b,c** show a secondary electron (SE) scanning transmission electron microscopy (STEM) image of the obtained particles using TiN nanoparticle dispersion and HfN nanoparticle dispersion. The SE-STEM image shows that the nanoparticles are three-dimensionally attached around the large sphere particles corresponding to SiO_2 particles. In the case of particles prepared using TiN nanoparticle dispersion, the attached nanoparticles either existed individually at approximately 10 nm or formed aggregates up to 30 nm in size. The SiO_2-HfN core-shell particles contained HfN nanoparticles, either individually approximately 10 nm in size or as aggregates up to 40 nm. High-angle annular dark-field (HAADF) STEM images and bright-field (BF)-STEM micrographs emphasize the contrast of the core-shell particles, clearly showing nanoparticles' presence around the spherical particles (**Figure 5.5**). **Figure 5.4.d** shows the absorption spectra of the TiN particle aqueous dispersion and the aqueous dispersions of the obtained core-shell particles containing 150, 180, 210, 240, 270, and 300 nm SiO_2 particles as cores. The aqueous dispersion of the TiN particles exhibited maximum absorption at 830 nm, while the aqueous dispersions of the obtained particles containing SiO_2 particles did not show maximum absorption. In the case of SiO_2-HfN system, dispersion containing only HfN nanoparticles exhibited absorption at 610 nm, the dispersion containing core-shell particles did not show the

maximum absorption. However, the dispersions of core-shell particles containing 150 nm and 180 nm showed an increasing trend of absorbance at the wavelength corresponding to the absorption of HfN. The X-ray diffraction (XRD) profile (**Figure 5.1d**) shows the obtained core-shell particles contained TiN or HfN.

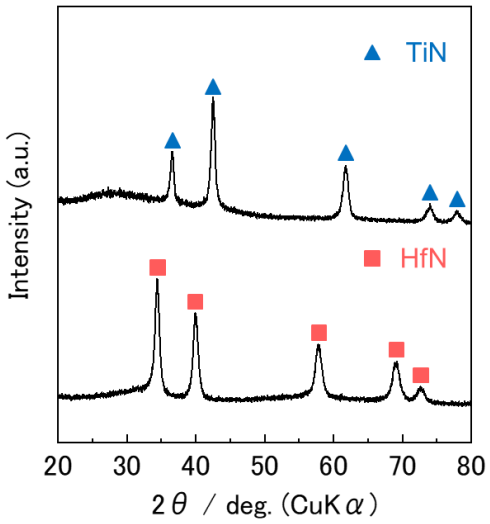

Figure 5. 1 XRD profiles of washed products from Mg_3N_2 and MO_2 (M=Ti and Hf).

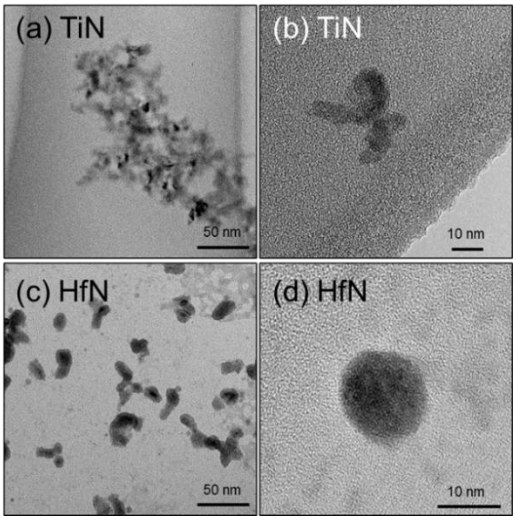

Figure 5. 2 (a) TEM micrograph of obtained TiN particles and **(b)** high-magnification image of TiN particles. **(c)** TEM image of obtained HfN particles and **(d)** high-magnification image.

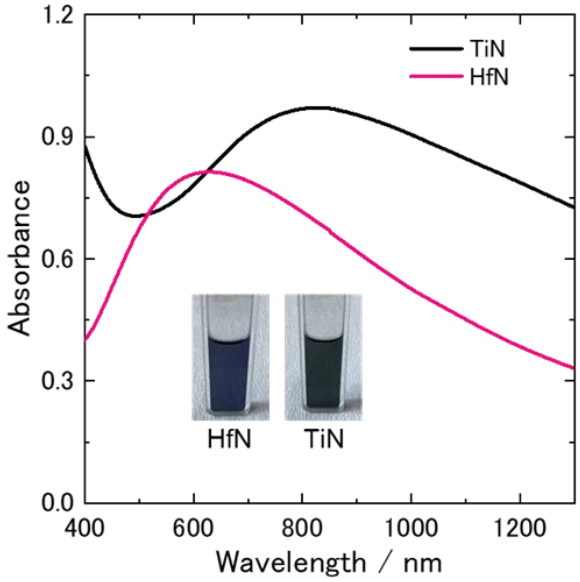

Figure 5. 3 Absorbance spectra of obtained TiN nanoparticle dispersion and HfN nanoparticle dispersion.

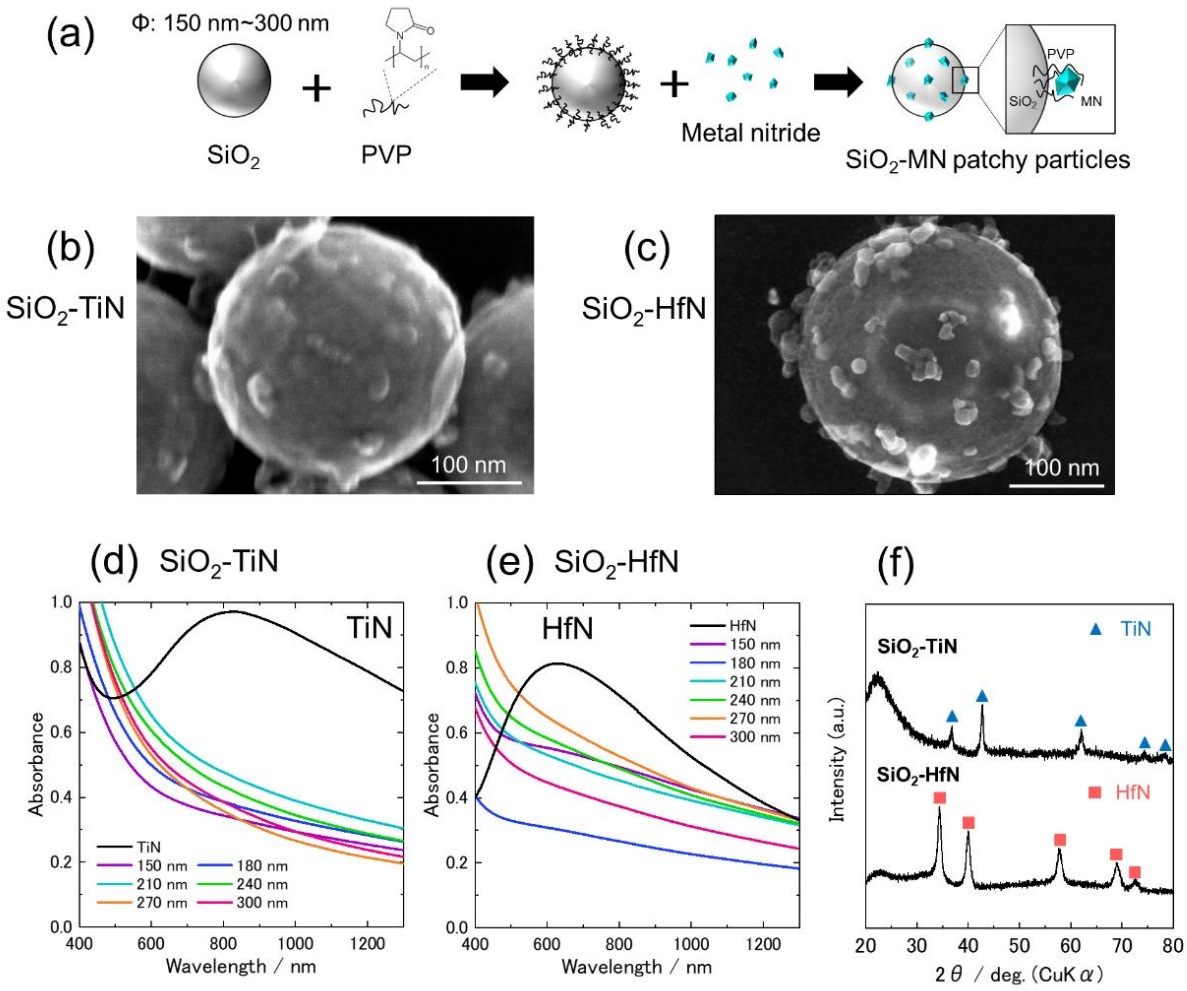

Figure 5. 4 (a) Schematic illustration of the preparation process of SiO_2-MN core-shell particles. SE-STEM images of the obtained particle using **(b)** TiN nanoparticle dispersion and **(c)** HfN nanoparticle dispersion. **(d)** Absorption spectra of aqueous dispersions of TiN nanoparticles and the obtained core-shell particles containing 150, 180, 210, 240, 270, and 300 nm SiO_2 core particles, and **(e)** HfN nanoparticles and obtained particles using them. **(f)** XRD pattern of the obtained particles.

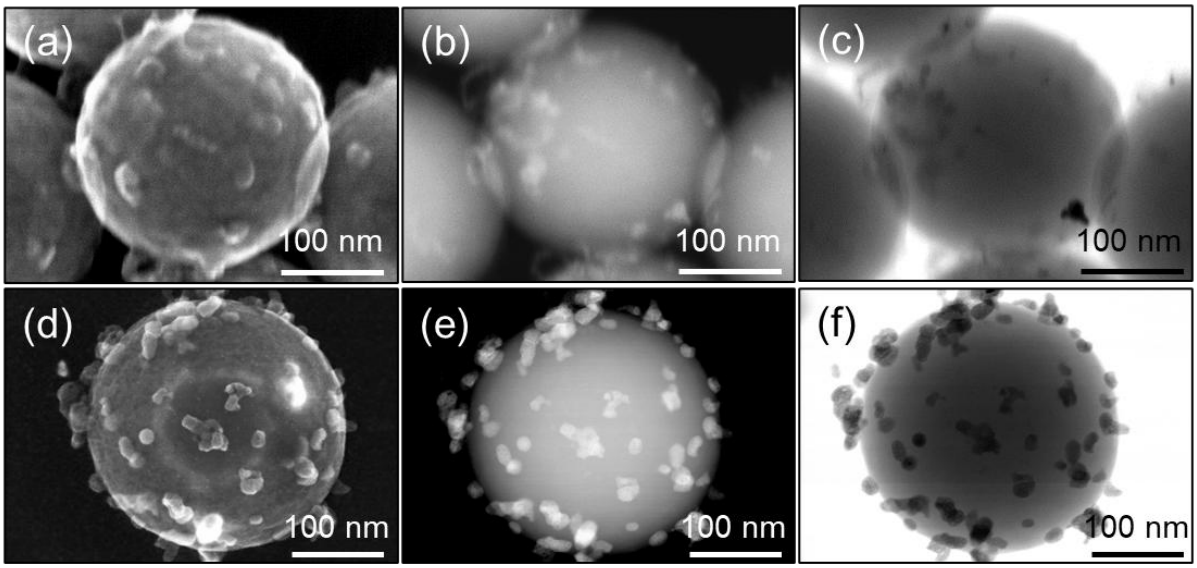

Figure 5. 5 (a) SE-STEM images, **(b)** HAADF STEM image, and **(c)** BF STEM image of the SiO_2-TiN core-shell particles. **(d)** SE STEM images, **(e)** HAADF STEM image, and **(f)** BF STEM image of the SiO_2-HfN core-shell particles.

The BF-STEM images of the obtained particles and energy-dispersive X-ray spectroscopy (EDS) mapping of the image (**Figure 5.6.a,b**) showed nanoparticles adhered to sphere particle containing Ti and Hf. The high magnification HAADF STEM images (**Figure 5.6.c,d**) of nanoparticles give crystal face {011} of TiN and {100} of HfN, respectively. These results confirmed the obtained particles were SiO_2-TiN core-shell particles and SiO_2-HfN core-shell particles. The metal nitride nanoparticles were strongly attached to SiO_2 particles, as the metal nitride nanoparticles remained adhered to SiO_2 particles even after ultrasonic dispersion in water during sample preparation for electron micrograph observation. The absorption at approximately 650 nm of the obtained aqueous SiO_2-HfN particle dispersions containing 150 nm and 180 nm SiO_2 core particles (**Figure 5.4.e**) was attributed to HfN nanoparticles; the obtained particles absorbed light in the 600–700 nm wavelength range through the attached HfN nanoparticles. For

the SiO_2-TiN dispersion diluted four times, an increasing trend at 800–900 nm in absorbance was observed (**Figure 5.7**). The absorption was from the LSPR of TiN nanoparticles adhered to SiO_2 particles. However, the obtained SiO_2-TiN core-shell particles and SiO_2-HfN core-shell particles containing 210 nm, 240 nm, 270 nm, and 300 nm SiO_2 core particles did not exhibit peaks in the absorption spectra because the influence of Mie scattering[29] by SiO_2 core particles was greater than that of the absorption of TiN nanoparticles and HfN nanoparticles attached to SiO_2 particles in the dispersion. The increase in particle size and concentration of particles extends Mie scattering. This resulted in a more significant influence of light loss due to Mie scattering than absorption by LSPR of metal nitride nanoparticles to exhibit no peak in the absorption spectra using 210 nm, 240 nm, 270 nm, and 300 nm SiO_2 core particles.

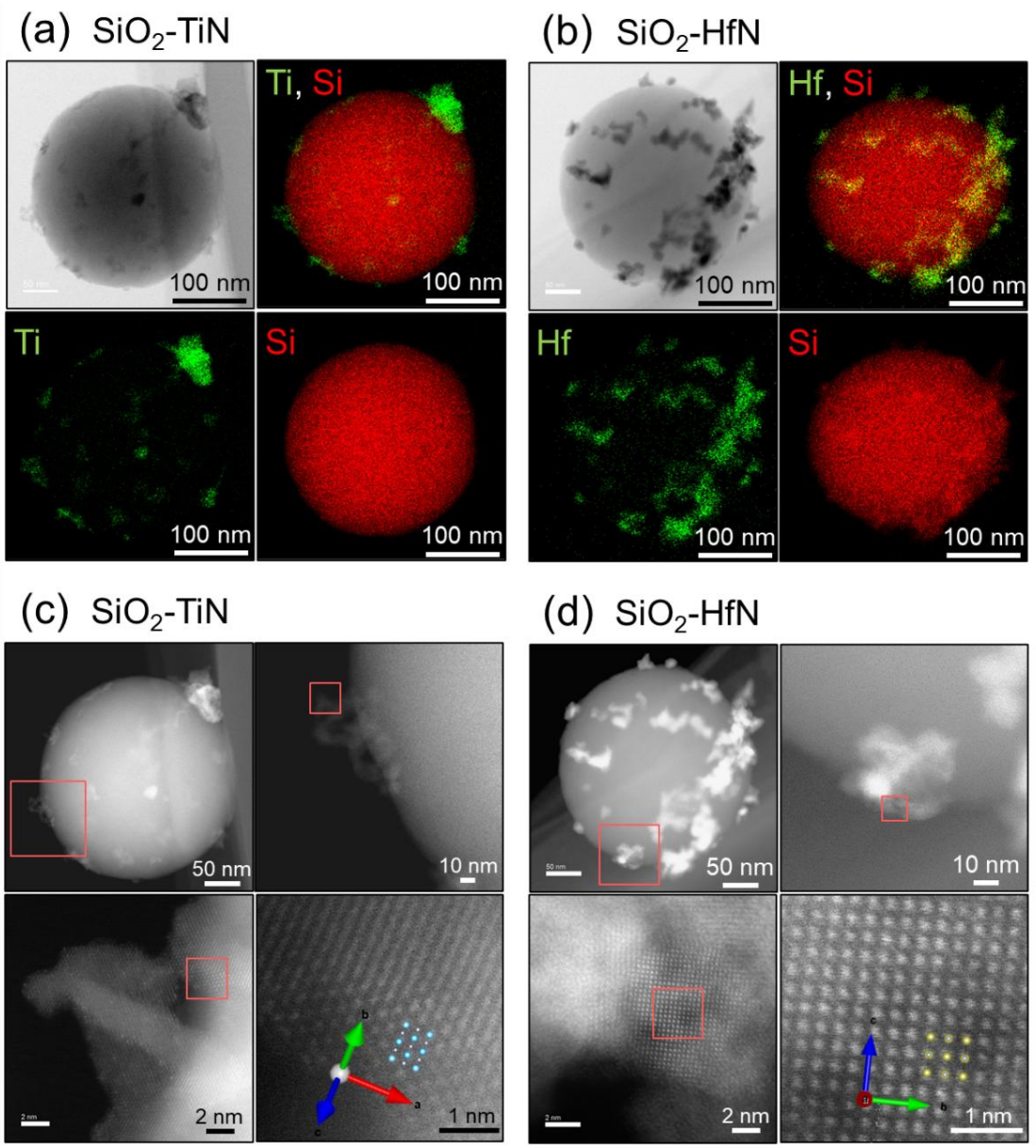

Figure 5. 6 (a) BF-STEM image of the obtained particle containing TiN nanoparticles and EDS mapping images highlighted by elements Ti and Si, and **(b)** BF-STEM image of the obtained particle containing HfN nanoparticles and EDS mapping images highlighted by elements Hf and Si. **(f)** HAADF-STEM images of the obtained particle containing **(c)** TiN nanoparticles and **(d)** HfN nanoparticles: overall view of particle, low magnification image, intermediate magnification image, and high magnification image of the area enclosed by the red square.

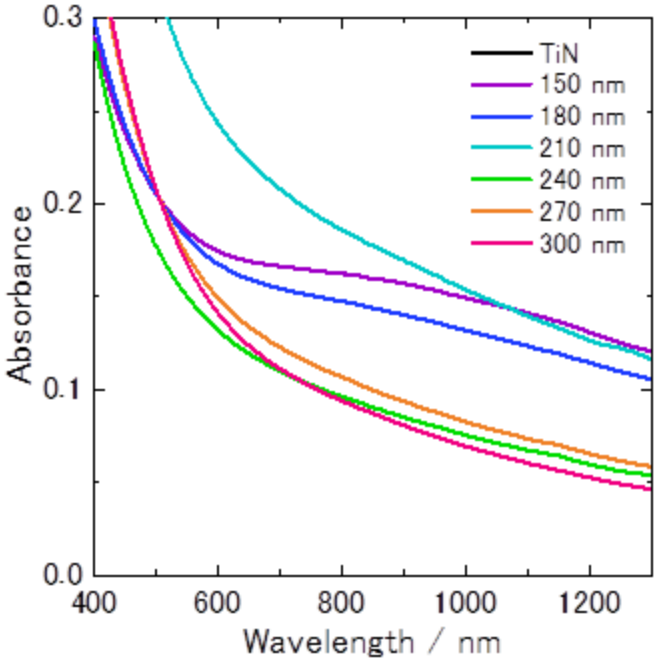

Figure 5. 7 Absorption spectra of aqueous dispersions of SiO_2-TiN shell particles containing 150, 180, 210, 240, 270, and 300 nm SiO_2 core particles (0.125 wt.%).

5.2.2 Optical Properties of Powders and Particle-stacked Films of SiO_2-TiN Core-shell Particles and SiO_2-HfN Core-shell Particles

Figure 5.8.a,c shows photographs of the dried powder, and **Figure 5.8.b,d** shows BF-STEM images of the obtained SiO_2-TiN core-shell particles and SiO_2-HfN core-shell particles containing 150, 180, 210, 240, 270, and 300 nm SiO_2 core particles. In the case of SiO_2 particles alone with nothing attached to them, the powder was white (**Figure 5.9**), whereas the powder of SiO_2-metal nitride core-shell particles, which had metal nitride nanoparticles attached around the SiO_2 particles, was colored. It was found that a sufficient distribution density of metal nitride nanoparticles was attached around the SiO_2 particles to observe the coloring behavior of the

SiO_2-metal nitride core-shell particle powder. The BF-STEM images (**Figure 5.8.b,d**, **Figure 5.10**, and **Figure 5.11**) prove that the TiN nanoparticles and HfN nanoparticles were attached to the surface of SiO_2 core particles of all sizes used, forming SiO_2-TiN core-shell particles and SiO_2-HfN core-shell particles containing 150-300 nm of SiO_2 core. The obtained particle's size distribution (**Figure 5.12**, **Figure 5.13**) confirmed that the metal nitride particles adhered to the SiO_2 core particles to an extent that did not compromise monodispersity of the SiO_2 particles. The powder of the obtained SiO_2-TiN core-shell particles and SiO_2-HfN core-shell particles exhibited a color that depended on the particle size after drying at room temperature. The change in color depending on particle size indicated that the color originated from the aggregate structure of the particles. In addition, when the amount of metal nitride nanoparticles attached to the SiO_2-metal nitride core-shell particles was small, the color of the SiO_2-metal nitride core-shell particle powder became lighter and closer to white (**Figure 5.9**). These results indicate that the color of SiO_2-metal nitride core-shell particle powder can be adjusted by changing the amount of metal nitride nanoparticles attached around the SiO_2 particles.

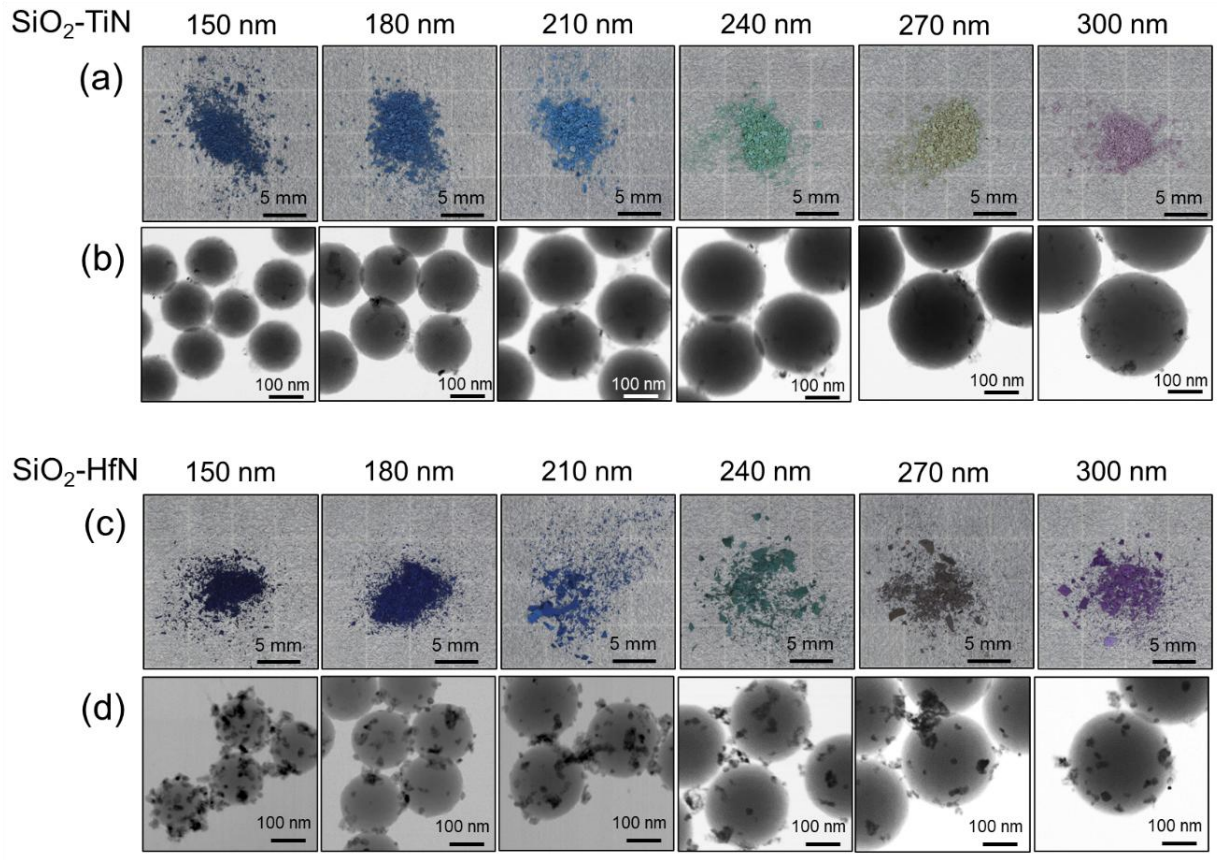

Figure 5. 8 (a) Photographs of the obtained powder and **(b)** BF-STEM images of the SiO_2-TiN core-shell particles, which contain SiO_2 core particles of 150, 180, 210, 240, 270, and 300 nm. **(c)** shows photographs of the obtained powder and **(d)** presents BF-STEM images of the SiO_2-HfN core-shell particles with SiO_2 core particles of the same sizes.

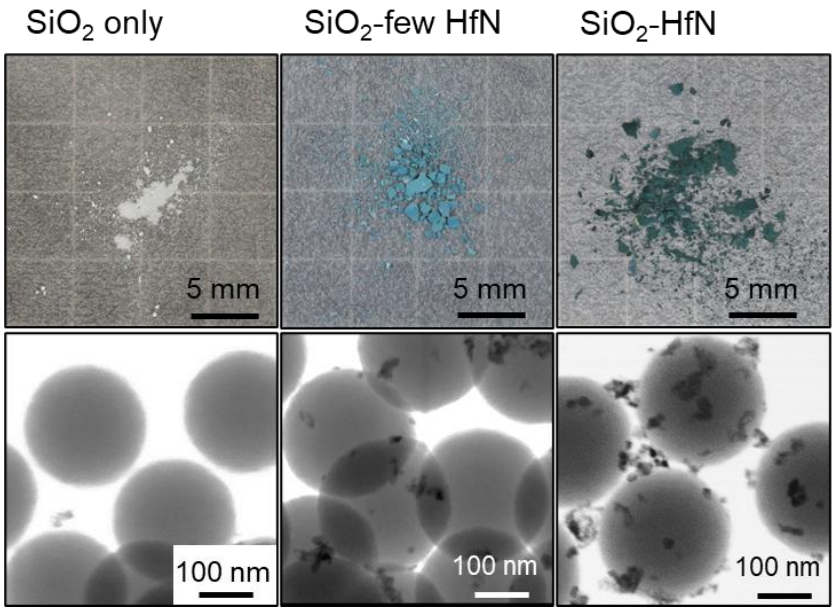

Figure 5. 9 Photographs and BF-STEM images of the obtained powder for the following samples: 240 nm SiO_2 particles, SiO_2-few HfN core-shell particles and SiO_2-HfN core–shell particles containing 240 nm SiO_2 particles as the core.

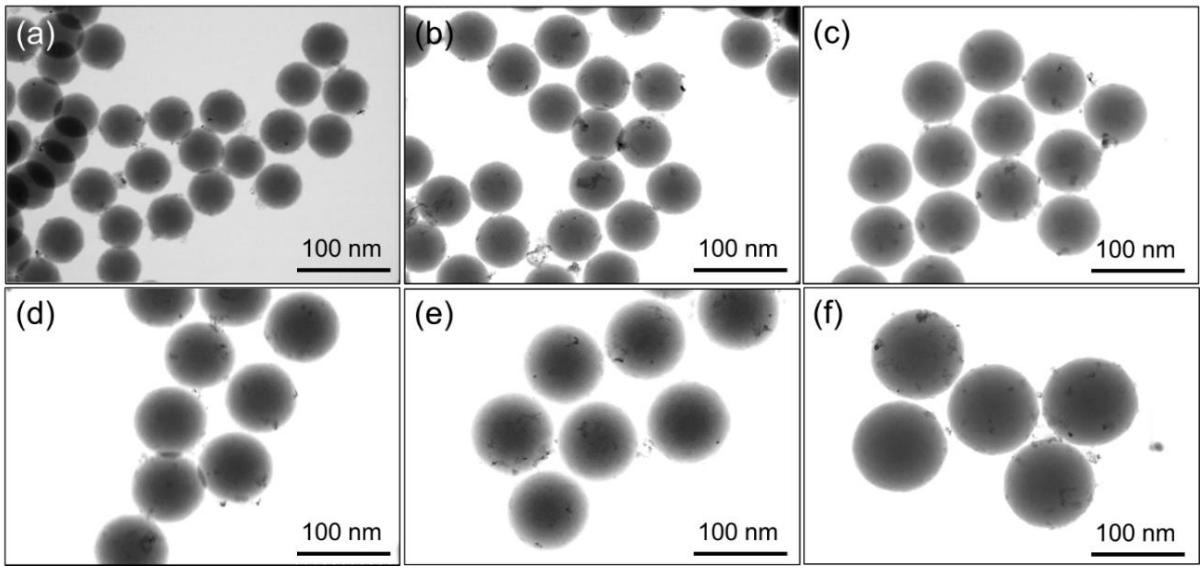

Figure 5. 10 BF-STEM images of the SiO_2-TiN core-shell particles containing SiO_2 core particles of (a) 150, (b) 180, (c) 210, (d) 240, (e) 270, and (f) 300 nm.

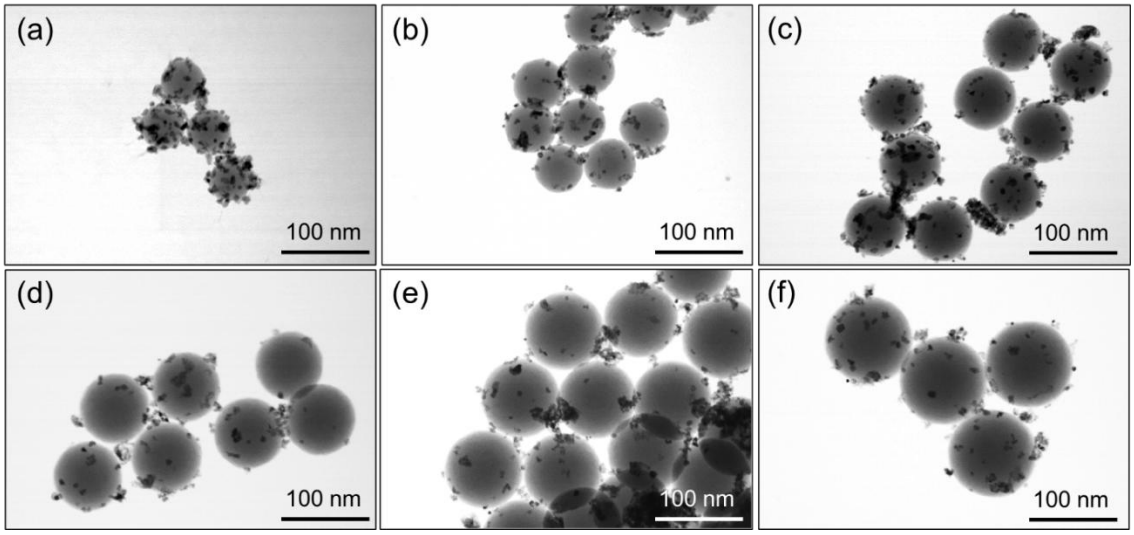

Figure 5. 11 BF-STEM images of the SiO_2-HfN core-shell particles containing SiO_2 core particles of (a) 150, (b) 180, (c) 210, (d) 240, (e) 270, and (f) 300 nm.

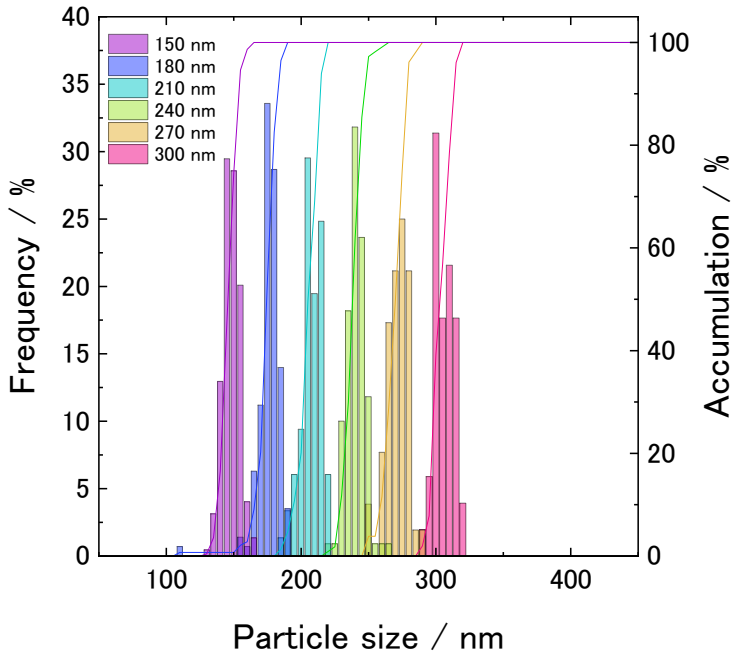

Figure 5. 12 The particle size distribution diagram of produced SiO_2-TiN core-shell particles containing 150–300 nm SiO_2 particle as the core. The particle size distribution is derived from STEM images of produced SiO_2-TiN core-shell particles.

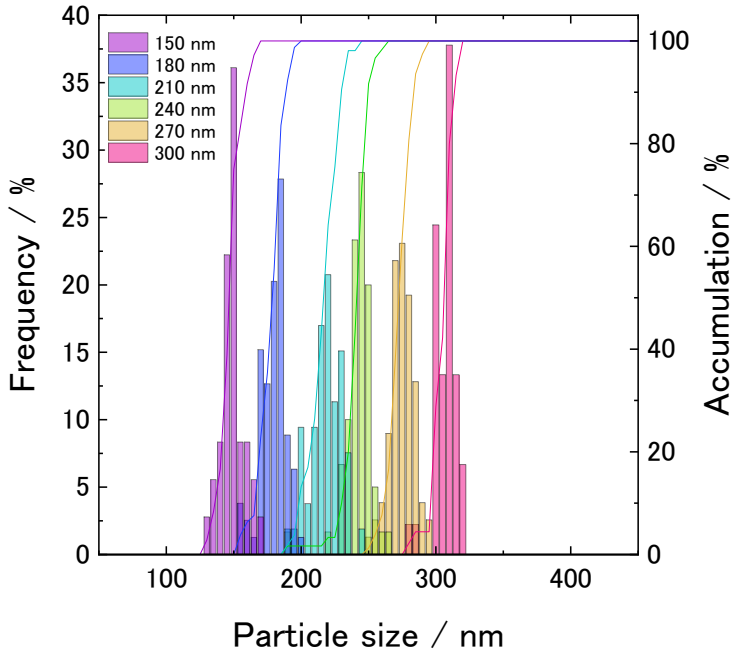

Figure 5. 13 The particle size distribution diagram of produced SiO_2-HfN core-shell particles containing 150–300 nm SiO_2 particle as the core. The particle size distribution is derived from STEM images of produced SiO_2-HfN core-shell particles.

Particle-stacked films with SiO_2-TiN core-shell particles and SiO_2-HfN core-shell particles were fabricated by a casting method using molds to compare the effects of TiN nanoparticles and HfN nanoparticles. **Figure 5.14** shows photographs of the particle-stacked films with SiO_2-metal nitride core-shell particles containing 150, 180, 210, 240, 270, and 300 nm core particles. To examine the angular dependence of the color of the particle-stacked film, images taken with the light source directed at 10° to the particle-stacked films and the camera rotated in 10° increments from 35° to 65° to the particle-stacked films are also shown. **Figure 5.14.a** shows the results when SiO_2-TiN core-shell particles were used for particle-stacked film fabrication, and **Figure**

5.14.b shows the photographs in the case of using SiO_2-HfN core-shell particles. Regardless of whether SiO_2-TiN core-shell particles or SiO_2-HfN core-shell particles were used as constituent substances, the particle-stacked films were colored and did not show a white area caused by localized aggregation of particles observed in SiO_2 particle-stacked films (**Figure 4.7**). The color of both films containing SiO_2-TiN core-shell particles and SiO_2-HfN core-shell particles changed depending on the size of the constituent particles, indicating that the differences in particle size caused the color of the particle-stacked films.

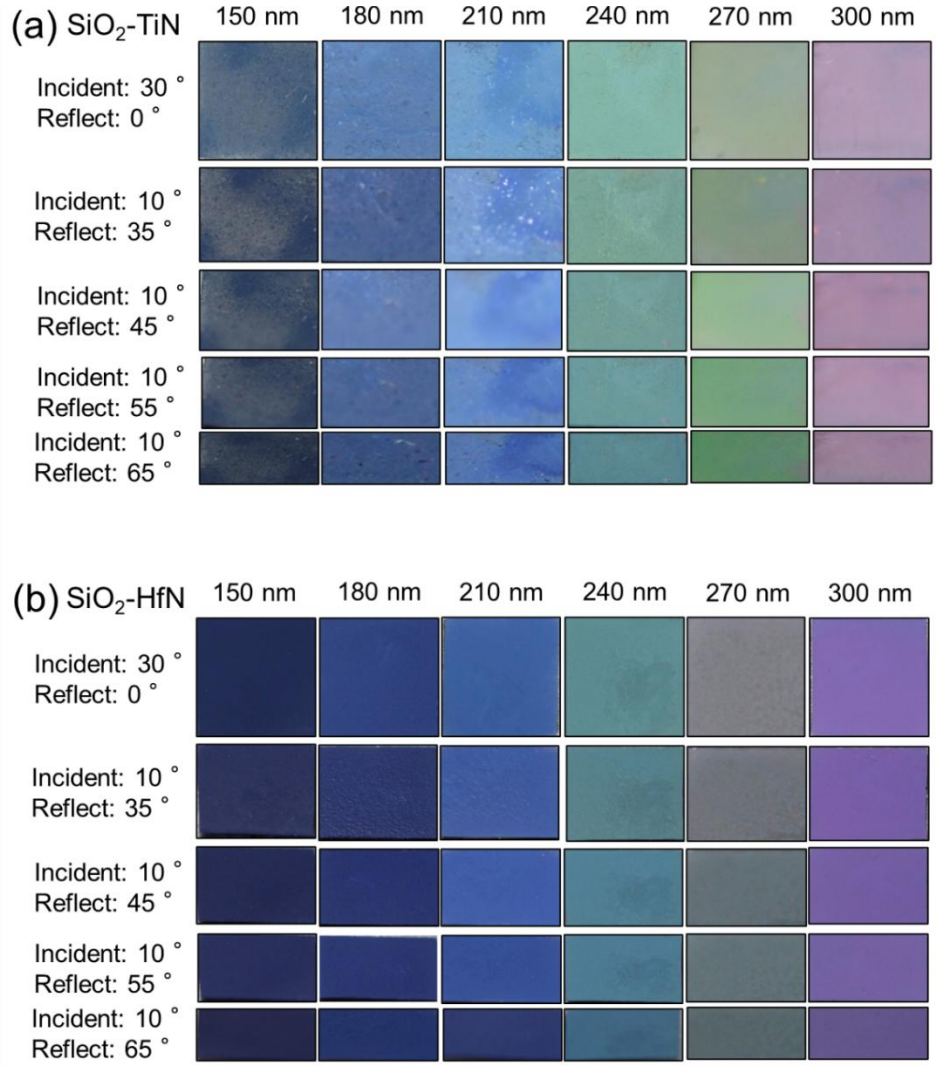

Figure 5. 14 (a) Photographs of the particle-stacked films comprising SiO_2-TiN core-shell particles with SiO_2 core particles of 150, 180, 210, 240, 270, and 300 nm. **(b)** Photographs of the particle-stacked film comprising SiO_2-HfN core-shell particles with SiO_2 diameters of 150, 180, 210, 240, 270, and 300 nm. For panels (a) and (b), the topmost photographs were taken with the camera positioned perpendicular to the particle-stacked films, and the light source inclined at 30° from the front of the film. The photographs in the subsequent rows were captured with the light source tilted at 10° from the front of the film, and the camera angled at 35°, 45°, 55°, and 65° from the front of the particle-stacked film, respectively.

The optical characteristics of the particle-stacked films of the obtained particles were assessed using reflection spectra. **Figure 5.15.a** shows the reflection spectra of the SiO_2-TiN core-shell particles stacked particles. In the case of the particle-stacked films containing SiO_2-TiN core-shell particles with diameters of 150, 180, 210, 240, 270, and 300 nm, peaks were observed at 334, 376, 442, 503, 564, and 621 nm, respectively, in the reflection spectra. For the SiO_2-TiN core-shell particles with diameters of 240, 270, and 300 nm, peaks at 316, 340, and 378 nm were observed on the short-wavelength side. As discussed in Chapter 4, the reflection of light within a photonic crystal follows Bragg's condition (Equation 40).[243] This relationship, expressed as

$$n\lambda = 2d\sin\theta \tag{40}$$

where n, λ, d, and θ represent the diffraction order, the wavelength of light, the lattice constant, and the angle between the incident light and the normal to the layers, respectively. In the case of amorphous arrays, the relatively broad reflection of specific wavelengths occurs due to Bragg diffraction in the local periodic structure regions, as explained in Chapter 4. The particle size determines the wavelength of the reflected light because the distance between layers where Bragg diffraction occurs depends on the size of the particles. Therefore, the shift of the wavelength in the reflection peak towards longer wavelengths corresponds to an increase in the distance of the pitch in the periodic structure of the particle-stacked films. **Figure 5.15.b** shows the reflection spectra of particle films from SiO_2-HfN core-shell particles. The particle-stacked films of SiO_2-HfN core-shell particles with SiO_2's diameters of 150, 180, 210, 240, 270, and 300 nm exhibited peaks at 322, 372, 436, 497, 566, and 634 nm, respectively, in the reflection spectra. Similar to the SiO_2-TiN core-shell particles, reflection peaks appeared on the short-wavelength side at 306, 344, and 380 nm when the particle sizes of the SiO_2 particle-stacked films were 240, 270, and 300 nm, respectively. In the reflection spectra of the particle-stacked films, the appearance of maxima, which shifted depending on the particle size, signified that

these maxima originated from structural colors, where periodic structures strongly reflected specific wavelengths.

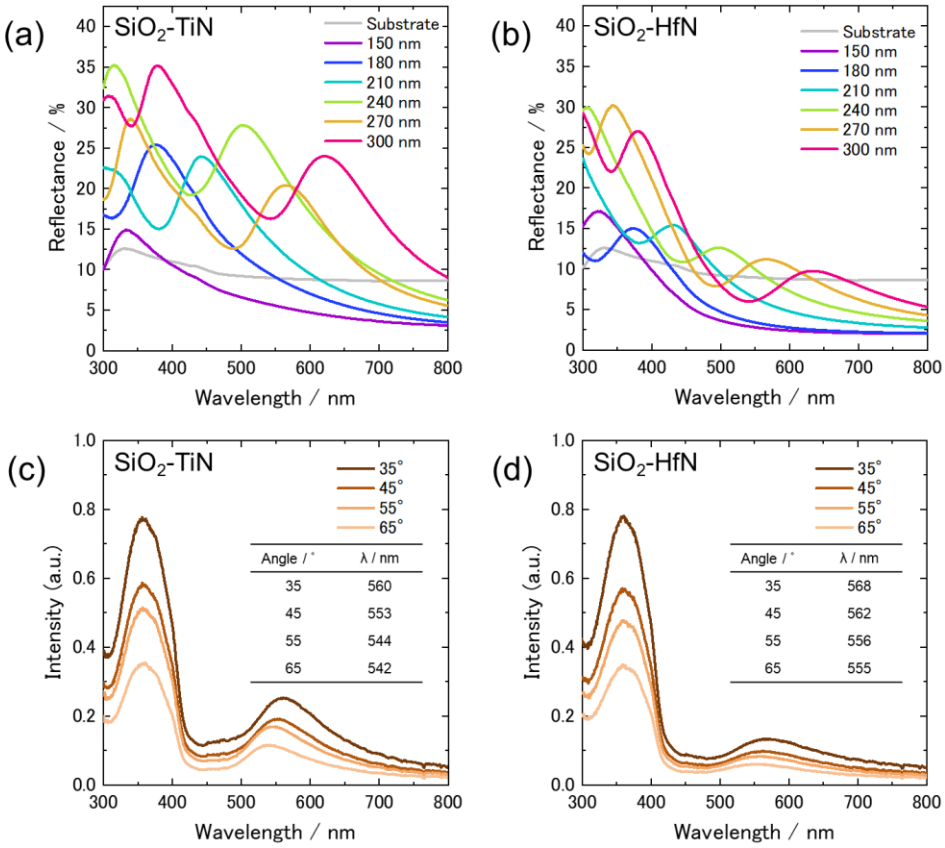

Figure 5. 15 Reflection spectra of the **(a)** SiO_2-TiN core-shell particle-stacked films and **(b)** SiO_2-HfN core-shell particle-stacked films composed of SiO_2 particles with diameter of 150–300 nm. The light was incident at 5° from the vertical plane of the particle laminated film, with the reflected light detected with an integrating sphere unit. Angular dependence of reflection spectra of the **(c)** SiO_2-TiN core-shell particle-stacked film and **(d)** SiO_2-HfN core-shell particle-stacked film of SiO_2 particles with diameters of 270 nm. The reflectance intensity was measured to analyze angular dependence: the incident angle of the light source to the particle-stacked film was 10°, and the reflection angle to the detector was in 10° increments from 35° to 65°.

Table 5.1 lists the maximum peaks, reflectance, and reflection intensity ratio ($R_l\ R_s^{-1}$) of the long-wavelength side (R_l) to the reflection intensity on the short-wavelength (R_s) side in the reflection spectra of particle-stacked films using SiO_2-TiN core-shell particles and SiO_2-HfN core-shell particles. The reflection intensity ratio ($R_l\ R_s^{-1}$) of the particle-stacked films using SiO_2-TiN core-shell particles decreased from 0.79 to 0.68 when the particle size was between 240 and 300 nm, unlike the case of using only SiO_2, whose values were constant at approximately 0.58 (**Table 4.1**). The ratio of SiO_2-HfN core-shell particles decreased from 0.42 to 0.37 when the particle size was between 240 and 300 nm, and the value was almost constant from particle size 270 nm to 300 nm. The prepared TiN nanoparticles absorbed across the entire reflection band with a peak at 830 nm because of LSPR. Therefore, the fabricated SiO_2-TiN core-shell particles also absorbed across reflection as the whole band with a peak at 830 nm. The reflection intensity of the particle-stacked films using SiO_2-TiN core-shell particles decreased as the reflection wavelength on the long-wavelength side approached long-wavelength (830 nm corresponding to the absorption of TiN), thus indicating that the reflection of particle-stacked films using SiO_2-TiN core-shell particles was suppressed by the LSPR absorption of TiN owing to the presence of TiN particles around SiO_2. In the case of HfN, the prepared HfN nanoparticles absorbed across the entire reflection band with a peak at 610 nm. As shown in **Figure 5.15.e**, the HfN nanoparticles used as shell particles exhibit a broad absorption around 610 nm. Thus, the fabricated SiO_2-HfN core-shell particles absorbed around 600 nm across the reflection. The reflection intensity of the particle-stacked films using SiO_2-HfN core-shell decreased as the reflection wavelength approached 610 nm, corresponding to the absorption of HfN, indicating that the reflection of particle-stacked films using SiO_2-HfN core-shell particles was suppressed

by the LSPR absorption of HfN owing to the presence of HfN particles around SiO_2, in a manner similar to the SiO_2-TiN core-shell particle system. The color of the SiO_2-metal nitride core-shell particle powder depended on the distribution density of metal nitride nanoparticles attached around the SiO_2 particles (**Figure 5.9**), and previous chapter showed that particle-stacked films of SiO_2-ZrN core-shell particles with a higher distribution density of ZrN nanoparticles exhibited a more pronounced photonic-plasmonic coupling effect. [251] Therefore, the photonic-plasmonic coupling effect of the SiO_2-metal nitride particle-stacked films was tuned by the distribution density of metal nitride nanoparticles as shell particles.

Table 5. 1 Particle size (φ), wavelength of maximum peaks (λ), reflectance (*R*), and reflection intensity ratio ($R_l\ R_s^{-1}$) of the long wavelength side (R_l) to the reflection intensity on the short wavelength (R_s) side in the reflection spectrum of the particle-stacked films using SiO_2-TiN core-shell particles and SiO_2-HfN core-shell particles.

Type	**φ / nm (core size)**	**λ / nm**	***R* / %**	$\boldsymbol{R_l\ R_s^{-1}}$ **/ –**
SiO_2-TiN core-shell particles	150	334	14.87	–
	180	376	25.43	–
	210	442	23.95	–
	240	316, 503	35.23, 27.84	0.79
	270	340, 564	28.63, 20.41	0.71
	300	378, 621	35.16, 24.00	0.68
SiO_2-HfN core-shell particles	150	322	17.13	–
	180	372	15.02	–
	210	432	15.41	–
	240	306, 497	29.97, 12.62	0.42
	270	344, 566	30.19, 11.19	0.37
	300	380, 634	27.00, 9.75	0.36

When a structurally colored material is used as a colorant, a lower angular dependence of the visible color is desirable. Thus, the angular dependence of the reflection spectra of the particle-stacked films was evaluated. The angular dependence of the reflection spectra of the particle-stacked films composed of SiO_2-TiN core-shell particles with core particles of 270 nm are shown in **Figure 5.15.c**, and those of SiO_2-HfN core-shell particles core particles of 270 nm are shown in **Figure 5.15.d**. When the angle changed from 35° to 65°, the maximum peak wavelength changed by 18 nm for the particle-stacked films composed of SiO_2-TiN core-shell particles and 13 nm for the particle-stacked films consisting of SiO_2-HfN core-shell particles. In both cases, the shift was smaller than the value of the films composed of only SiO_2 (**Figure 4.7**).[251] Even in particle-stacked films with 240 and 300 nm particles, the shift was smaller for SiO_2-TiN core-shell particles and SiO_2-HfN core-shell particles (**Figure 5.16**, **Figure 5.17**). These results suggest that the SiO_2-TiN core-shell particles and SiO_2-HfN core-shell particles were stacked more randomly than the SiO_2 particles, similar to the results with 270 particles. Thus, the core-shell particle-stacked film exhibited less angular dependence than the silica particle-layered film.

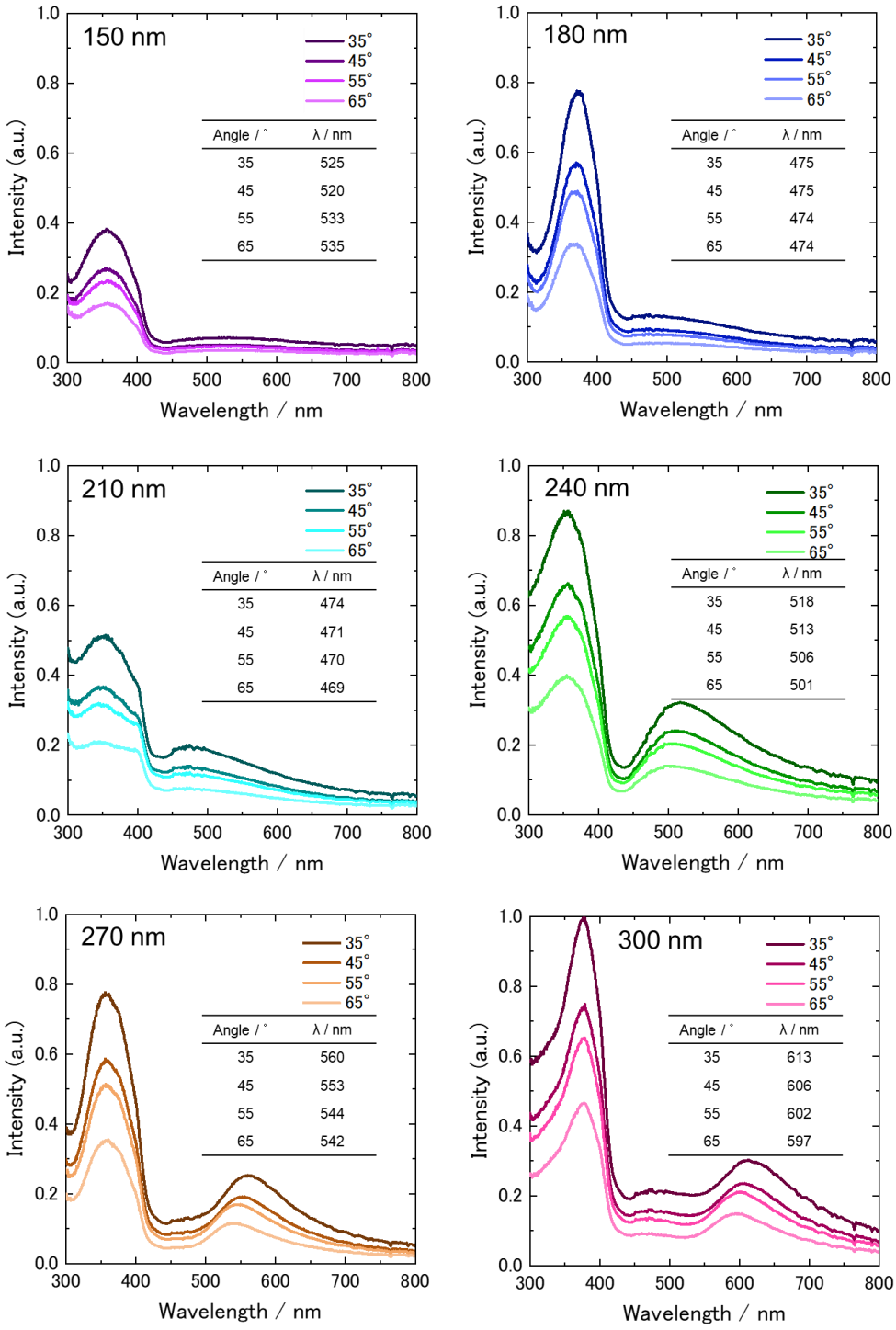

Figure 5. 16 Angular dependence of reflection spectra of particle-stacked films comprising SiO_2-TiN core-shell particles with core particles of 150, 180, 210, 240, 270, and 300 nm.

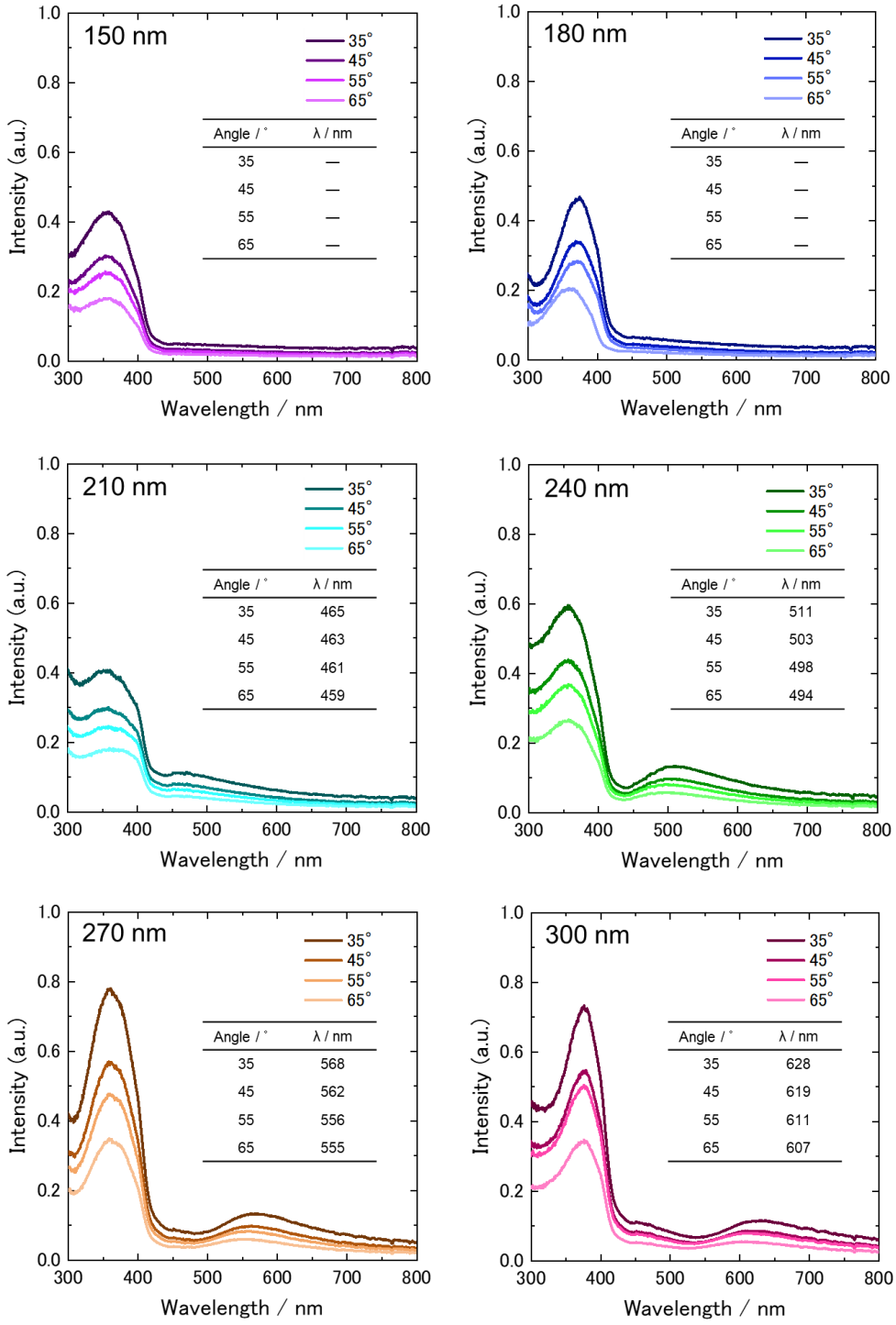

Figure 5. 17 Angular dependence of reflection spectra of particle-stacked films comprising SiO_2-HfN core-shell particles with core particles of 150, 180, 210, 240, 270, and 300 nm.

The stacked particle films were observed using field-emission scanning electron microscopy (FE-SEM) to investigate the stacking state of the particles. **Figure 5.18** shows surface and cross-sectional FE-SEM images of the particle-stacked films. For both the SiO_2-TiN and SiO_2-HfN particle-stacked films, the lack of a periodic arrangement of particles was evident from the surface images (**Figure 5.18.a,d**), and the fact that the Fourier transform images did not show distinct spots further confirmed that the particles were distributed randomly. Protrusions on the particle surface were observed in both SiO_2-TiN and SiO_2-HfN particle-stacked films from high-magnification images (**Figure 5.18.b,e**). These protrusions correspond to TiN nanoparticles and HfN nanoparticles attached to SiO_2 core particles. From the cross-sectional FE-SEM images (**Figure 5.18.c,f**), no significant periodicity was observed in the height direction for both the particle-stacked films of the SiO_2-TiN core-shell particles and SiO_2-HfN core-shell particles. Thus, quasi-amorphous structures were obtained in both cases using the SiO_2-TiN core-shell particles and SiO_2-HfN core-shell particles. The periodicity of the SiO_2-TiN particles and SiO_2-HfN particles in the particle-stacked films was low, implying that the particle-stacked films of the SiO_2-TiN particles and SiO_2-HfN particles had little angular dependence on reflection, consistent with the reflection spectrum results (**Figure 5.18.c,d**).

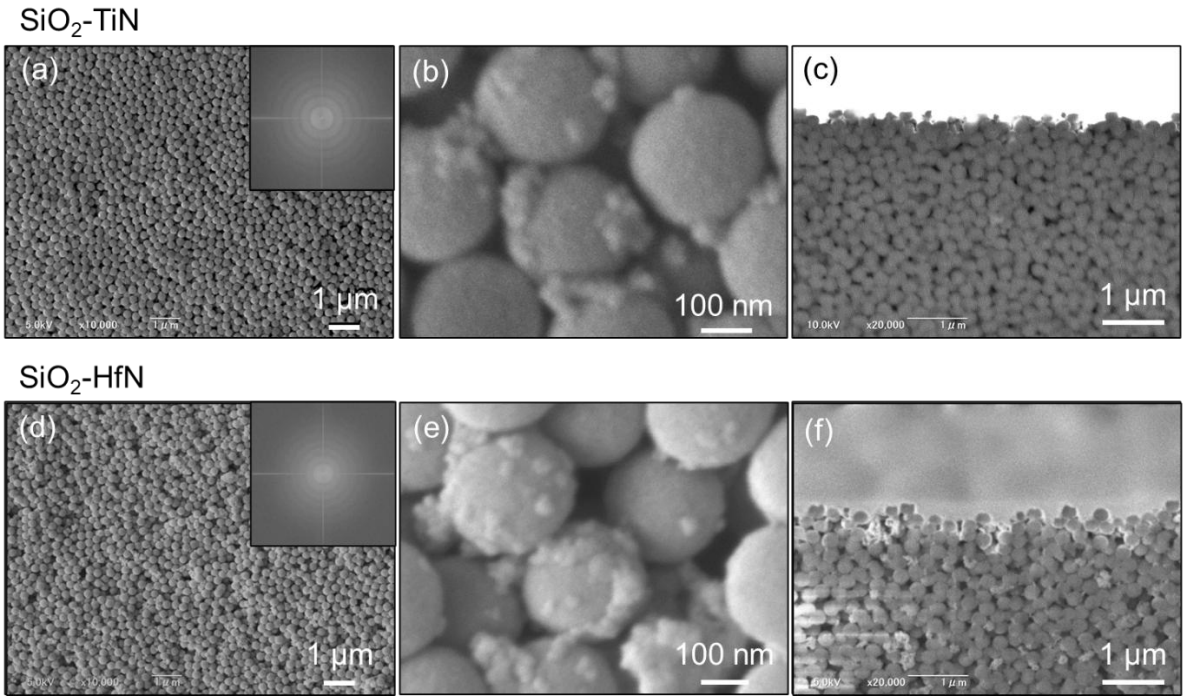

Figure 5. 18 Surface FE-SEM images of particle-stacked films comprising **(a)** SiO_2-TiN core-shell particles and **(d)** SiO_2-HfN core-shell particles with core particles of 270 nm and Fourier transform image. **(b)** and **(e)** show the high-magnification FE-SEM images of particle-stacked films consisting of SiO_2-TiN core-shell particles and SiO_2-HfN core-shell particles, respectively. Cross-sectional FE-SEM images of particle-stacked films comprising **(c)** SiO_2-TiN core-shell particles and **(f)** SiO_2-HfN core-shell particles with core particles of 270 nm.

To evaluate the hue of particle-stacked films, the chromaticity of the colors exhibited by each particle-stacked film was compared. **Figure 5.19.a,b** show the chromaticity diagrams of SiO_2-TiN core-shell particle-stacked films and SiO_2-HfN core-shell particle-stacked films composed of SiO_2 particles with diameters of 150–300 nm. Compared to particle-stacked films of SiO_2 only (**Figure 5.19.d**), the SiO_2-TiN core-shell particle-stacked films tended to show (x, y) coordinates positioned further outward, relative to the central point (0.33, 0.33) corresponding to the light

source. When comparing SiO_2-HfN core-shell particle-stacked films with particle-stacked films of only SiO_2, the x and y values tended to be lower than those in particle-stacked films of SiO_2 only for cores with SiO_2 particles. The SiO_2-ZrN core-shell particle-stacked films described in Chapter 4 were found to be positioned at lower x values and y values on the chromaticity diagram (**Figure 5.19.c**) compared to the SiO_2 particle-stacked films.

When incoherent scattering is suppressed across the entire visible spectrum, the chromaticity coordinates (x, y) position further outward than SiO_2 particle-stacked films relative to the central point (0.33, 0.33) corresponding to the light source. This is because suppression of incoherent scattering decreases the effects other than coherent scattering in the reflection spectrum. For the samples prepared in this study, the phenomenon of (x, y) positioning more outward applied to SiO_2-TiN core-shell particle-stacked films, likely because of the absorption of TiN nanoparticles at peak in the near-infrared, which did not significantly alter the intensity of visible light absorption. Differing from SiO_2-TiN core-shell particle-stacked films, SiO_2-ZrN and SiO_2-HfN core-shell particle-stacked films tended not to position further outward but to show lower x and y values than SiO_2 particle-stacked films. This was because the metal nitride nanoparticles attached to the core's surface exhibited absorption with a peak in the visible spectrum. The attached metal nitride nanoparticles enhanced the contrast of the particle-stacked films ((x, y) was positioned more outward relative to the central point (0.33, 0.33) corresponding to the light source) when the particle-stacked films exhibiting reflection peaks at wavelengths far from the absorption peaks of metal nitride nanoparticles were used. In SiO_2-ZrN core-shell particle-stacked films and SiO_2-HfN core-shell particle-stacked films with particle sizes of 240–300 nm, differing trends were noted because of the different absorption wavelengths of ZrN and HfN nanoparticles. SiO_2-HfN particle-stacked films with 240 nm SiO_2 core particles showed

decreased x values without significant change in y values. SiO_2-ZrN particle-stacked films with 240 nm SiO_2 core particles showed decreased x and y values. In the case of the particle-stacked films with 270 nm SiO_2 core particles, SiO_2-HfN particle-stacked films showed slightly a decreased x value and decreased y value, and SiO_2-ZrN particle-stacked films showed a decreased x value and a slightly decreased y value. In the particle-stacked films with 300 nm SiO_2 core particles, both x and y values decreased in SiO_2-HfN particle-stacked films, and SiO_2-ZrN core-shell particle-stacked films showed a slight decrease in x value but a significant reduction in y value. As shown in **Figure 5.15**, Particle-stacked films containing SiO_2 particles ranging from 240–300 nm exhibited two peaks in the reflection spectrum between 300-800 nm. The intensity ratio of these peaks varied depending on the type of metal nitride nanoparticles attached to SiO_2 core particles, and this ratio affected the position of the chromaticity coordinates. Consequently, films with 240–300 nm SiO_2 particles showed different trends of chromaticity coordinates specific to each type of metal nitride nanoparticles.

As the results indicate, the chromaticity of particle-stacked films greatly depended on the size of the SiO_2 core particles used, and further changed due to the type of metal nitride species attached around the SiO_2 core particles. The dependency on the size of the SiO_2 core particles was because the size of the particles altered the periodic pitch in the particle-stacked films, which in turn changed the reflected wavelength. The variation in chromaticity due to the attached metal nitride species occurred because the attachment of metal nitride nanoparticles suppressed reflection in the absorption wavelength region through LSPR of the metal nitride nanoparticles. Since different metal nitride species absorbed at different wavelengths, the chromaticity changed depending on the kind of metal nitrides when SiO_2 core particles of the same size were used.

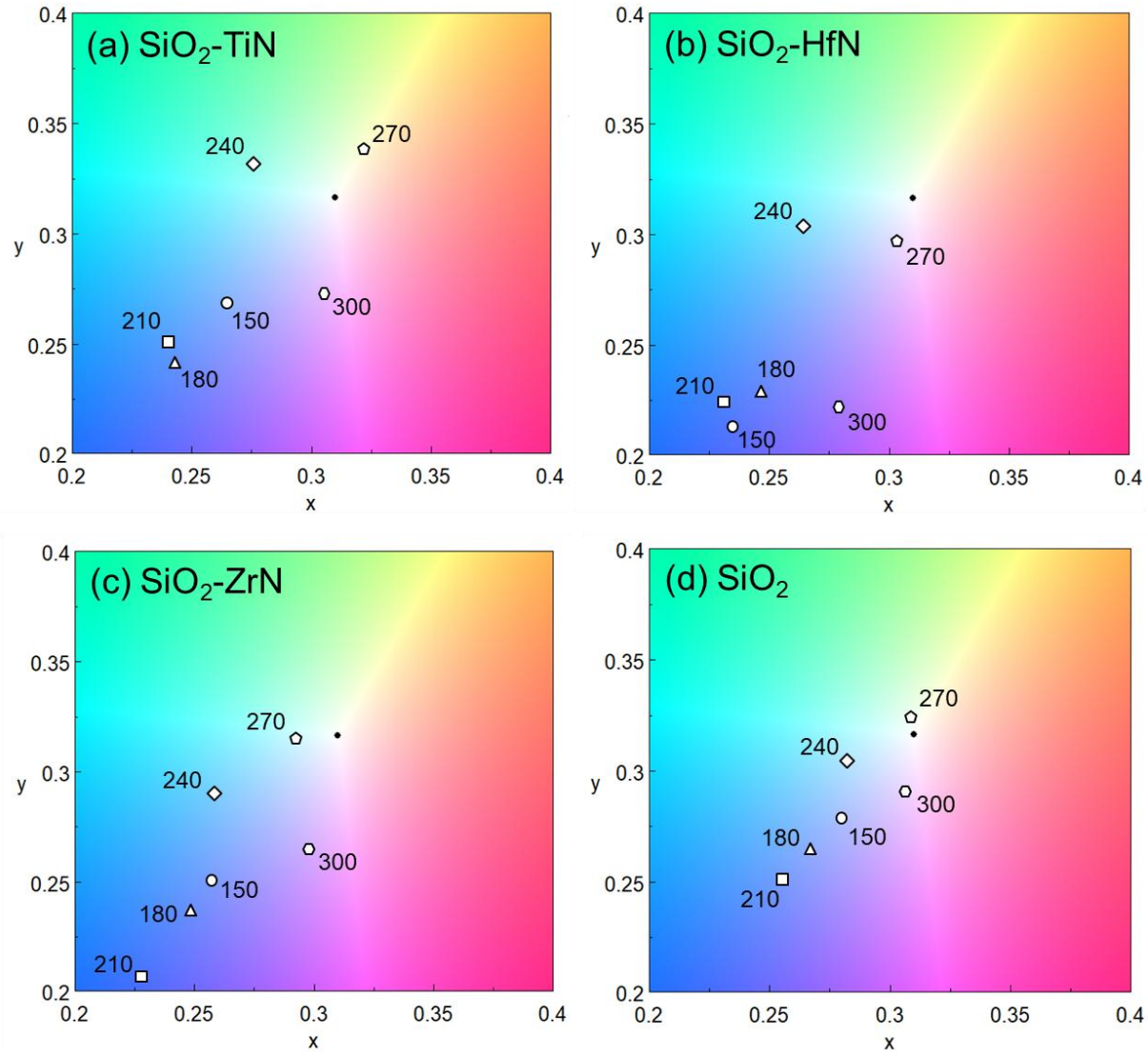

Figure 5. 19 Chromaticity diagrams of **(a)** SiO_2-TiN core-shell particle-stacked films, **(b)** SiO_2-HfN core-shell particle-stacked films, **(c)** SiO_2-ZrN core-shell particle-stacked films, and **(d)** SiO_2 particle-stacked films composed of SiO_2 particles with diameters of 150–300 nm.

To investigate the effect of metal nitride species on the coloration of core-shell particle-stacked films, the chromaticity of the SO_2 particle-stacked film, SiO_2-TiN core-shell particle-stacked film, SiO_2-ZrN core-shell particle-stacked film, and SiO_2-HfN core-shell particle-stacked film was compared. **Figure 5.20** shows the coloration of these films on a chromaticity diagram, which includes SiO_2 particles ranging from 150–300 nm. In the range of particle sizes used for the films, a film consisting only of SiO_2 particles exhibited colors in the x range of 0.26–0.31 and y range of 0.25–0.33 on the x-y chromaticity diagram. However, by adhering metal nitride nanoparticles around the particles, the particle-stacked films expressed colors within an x range of 0.23–0.32 and a y range of 0.21–0.34. That was, the attachment of metal nitride nanoparticles exhibiting LSPR to SiO_2 particles expanded the area of color that the particle-stacked films exhibited by coupling photonic properties and plasmonic properties. Therefore, the reflection of SiO_2-metal nitride core-shell particle-stacked films was controlled by not only choosing the particle size but also suppressing reflection due to specific wavelength absorption of LSPR by adding metal nitride species. Reflection control was possible by changing the type of metal nitride species used and by changing the amount of metal nitrides adhered to SiO_2 particles. SiO_2-metal nitride core-shell particles are materials capable of controlling color based on the three kinds of parameters of the SiO_2 particle size, the type of metal nitride species adhered to the SiO_2 particle, and the amount of metal nitride nanoparticles adhered.

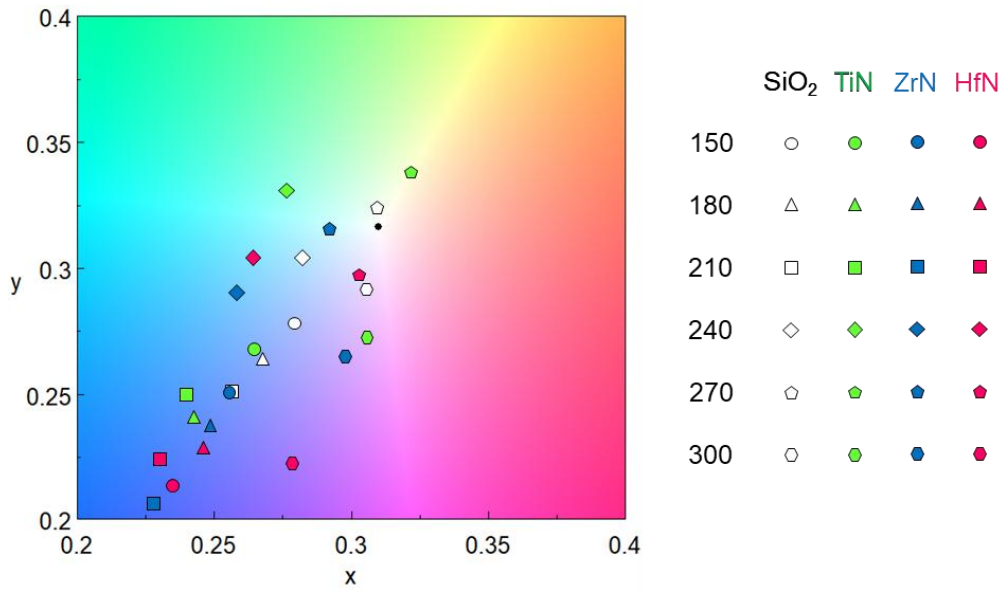

Figure 5. 20 Chromaticity diagram of SiO_2 particle-stacked films, SiO_2-TiN core-shell particle-stacked films, SiO_2-ZrN core-shell particle-stacked films, and SiO_2-HfN core-shell particle-stacked films composed of SiO_2 particles with diameters of 150–300 nm.

5.3 Conclusion

SiO_2-TiN core-shell particles and SiO_2-HfN core-shell particles were prepared. Color-controllable structural color materials were obtained by combining the specific wavelength range absorption through LSPR of the metal nitride nanoparticles around SiO_2 core particles and the photonic properties of periodic structures. The SiO_2-metal nitride core-shell particle-stacked films showed low angular dependence and photonic-plasmonic coupling effect capable of controlling color based on the three kinds of parameters of the SiO_2 particle size, the type of metal nitride species adhered to the SiO_2 particle, and the distribution density of metal nitride nanoparticles adhered. That was, the SiO_2-metal nitride core-shell particles were able to tune the reflection and absorption spectra by these parameters. The ability to tune the optical properties

through the coupling of plasmonic effects and photonic properties without precious metal not only enhances the aesthetic value of these materials but also opens possibilities for applications where the control of light-matter interactions can be crucial as the low cost and the social and environmental problem free materials.

5.4 Experimental Section

5.4.1 Materials

Titanium dioxide (TiO_2, 5 nm) and Hafnium dioxide (61-81 nm) were purchased from US research Nanomaterials, Inc. Magnesium nitride (Mg_3N_2) was purchased from Sigma Aldrich. SiO_2 particles were purchased from FUJI CHEMICAL Co., Ltd. Polyvinylpyrrolidone K 90 (PVP, Average Molecular Wt. 360000) was purchased from TOKYO CHEMICAL INDUSTRY Co., Ltd. Hydrochloric acid (1 M) was purchased from KANTO CHEMICAL Co., Inc.

5.4.2 Sample preparation

5.4.2.1 MN particle dispersion (M=Ti, Hf)

MN nanoparticles were synthesized using a modified version of the process described in our previous report. A mixture of 0.1 g of metal dioxide (TiO_2 or HfO_2) nano powder and a three-molar excess Mg_3N_2 powder was mixed for 5 min in an Ar glove box using an agate mortar. The resulting mixture was transferred to an alumina combustion boat and hermetically sealed in a plastic bag using a zip. The powder confined in the plastic bag was immediately inserted into a quartz tube and heated at 1000 °C for 12 h under nitrogen gas flow in a tubular furnace. After natural cooling to room temperature, the final product was transferred to a beaker and mixed with 25 mL of 1.0 M HCl solution. The mixture was sonicated for 20 min, and water (20 mL)

was added. After stirring for 1 h, the supernatant was separated by centrifugation for 1 h at 11000 rpm. The residual precipitate was redispersed in 5 mL of water by sonication and centrifuged for 15 min at 3300 rpm. The supernatant was collected in different colors to obtain nanoparticle dispersions: green for TiN using TiO_2 as the precursor, and purple for HfN using HfO_2 as the precursor.

5.4.2.2 SiO_2-TiN core-shell particles and SiO_2-HfN core-shell particles

PVP 90 (0.1 g) was added to a water dispersion (50 mL) of SiO_2 particles (0.05 g) while stirring at 400 rpm. The mixture was continuously stirred for one night. Subsequently, the liquids were centrifuged at 3300 rpm for 15 min, with the supernatant discarded to remove the solution containing unattached PVP 90. The precipitate was resuspended in water (50 mL) and sonicated. The suspended liquid was centrifuged again at 3300 rpm for 15 min, with the supernatant discarded again. The residue was suspended in water (5 mL) to obtain SiO_2 particles modified with PVP 90. The TiN dispersion (0.7 mL) or HfN dispersion (0.7 mL) was added to a 1 mL dispersion of modified SiO_2 particles. The mixture was then shaken and sonicated. The obtained dispersion was centrifuged at 3300 rpm for 15 min, with the supernatant discarded to remove the metal nitride nanoparticles not attached to the SiO_2 particles. The residual precipitate was dried to obtain the SiO_2-TiN core-shell particles or SiO_2-HfN core-shell particles.

5.4.2.3 Particle-stacked films

The obtained SiO_2-TiN core-shell particles and SiO_2-HfN core-shell particles were arrayed onto glass substrates by drop-casting using silicone molds. Silicone molds, with a thickness of 3 mm and a 1 cm square hole, were pressed onto glass substrates and pasted. The particles' dispersion (0.5 wt.%, 0.3 mL) was cast into the hole of the silicon mold. After natural drying for one day,

water used as a dispersion medium evaporated, and the particles self-assembled to form a particle-stacked film.

5.4.3 Material Characterization

5.4.3.1 X-ray Diffraction (XRD)

The crystalline phase was analyzed using an X-ray diffraction (XRD) diffractometer (Cu Ka, Mini-Flex 600, Rigaku, Japan). The diffraction angle 2θ was scanned in the range of 30–60° at a rate of 5° min^{-1}.

5.4.3.2 Transmission Electron Microscopy (TEM)

The morphologies of the core-shell particles were evaluated using TEM (JEM-2010, JEOL, Japan), with the dispersion of the core-shell particles drop-cast onto copper-mesh TEM grids. The acceleration voltage of the electron gun used for the observation was 200 kV.

5.4.3.3 Scanning Transmission Electron Microscopy (STEM)

The morphology of the core-shell particles was examined using scanning transmission electron microscopy (STEM) with an HD-2000 instrument (HITACHI, Japan). The sample was prepared following the same procedure as that for the TEM observation, with the electron gun acceleration voltage set to 200 kV. Energy-dispersive X-ray spectroscopy (EDS) was performed using the same equipment to investigate the elemental distributions of the particles.

5.4.3.4 Field Emission Scanning Electron Microscope (FE-SEM)

The surface and cross-sectional morphologies of the particle-stacked films were observed using field-emission scanning electron microscopy (FE-SEM) with a JIB–4601F instrument (JEOL,

Japan). The particle-stacked films were observed at an electron gun acceleration voltage of 200 kV after the films were coated with platinum. The observed cross-section was formed by the radiation of a focused ion beam onto the surface of the tungsten-coated particle-stacked film.

5.4.3.5 Spectrum measurement

The UV-Vis/NIR absorption spectra of the TiN particle dispersions, the HfN particle dispersions, the SiO_2-TiN core-shell particle dispersions, and the SiO_2-HfN core-shell particle dispersions were recorded using a V-770 spectrometer (JASCO, Japan). The dispersion was then placed in a 1 cm square quartz cell and mounted on a holder for measurement. Water was used as the background for the absorbance measurements. The scanning rate was 200 nm min^{-1} and the bandwidth was 2 nm, with a range of wavelengths scanned from 400 nm to 1300 nm. The reflection spectra of the particle-stacked films were measured using a V-700 spectrometer (JASCO, Japan) with an integrating spherical unit. The particle-stacked films were placed on a holder for measurement; the scanning rate was 200 nm min^{-1}, with a bandwidth of 5 nm and a range of wavelengths scanned from 300 nm to 900 nm. The plotting on the chromaticity diagram was performed using JASCO's color evaluation software (V-750/A011961799), based on the calculated values derived from the measured reflectance spectrum. The following conditions were applied: the color system used was XYZ, the light source was C (standard: CIE 15:2004), the standard observer function followed ASTM (American Society for Testing and Materials) E308:2008, the field of view was set to 2 degrees, the calculation range was 380–780 nm, and the data interval was 5 nm. The reflectance intensity was measured to analyze the angular dependence. Variable-angle reflection measurement optics, C10027A10687 (Hamamatsu Photonics, Japan) were used to expose the particle-stacked films to white light and detect the reflected light. A xenon lamp was used as the light source to measure the reflection spectra. A

photonic multichannel analyzer C10027 (Hamamatsu Photonics, Japan) was used to analyze the detected signals. The incident angle of the light source to the particle-stacked film was 10°, with the reflection angle to the detector varied in 10° increments from 35° to 65°.

Chapter 6 General Conclusion

This dissertation described the construction of particle-based structural color materials that combined reflective properties from periodic structures with specific wavelength range absorption through LSPR by metal nitride nanoparticles. The phenomenon exhibiting both photonic properties from periodic structures and specific wavelength range absorption of LSPR was defined as photonic–plasmonic coupling in this dissertation, and materials demonstrating this property were prepared using silica and metal nitride nanoparticles as structure and plasmonic sources, respectively. By developing these materials, this study aimed to achieve tunable optical properties through the combined adjustment of photonic and plasmonic characteristics without relying on noble or heavy metals.

Chapter 1 provides an overview of coloring materials, discussing the research background and positioning the present study within the context of existing work.

In Chapter 2, ZrN nanoparticles exhibiting LSPR were synthesized as cores, and SiO_2 formed around ZrN nanoparticles as shells to prepare monodisperse ZrN-SiO_2 core-shell particles for potential application as structural color materials. However, the monodispersity of the ZrN-SiO_2 core-shell particles was insufficient for structural color applications, making it difficult to evaluate the photonic effects arising from periodic structures in combination with specific wavelength range absorption through the LSPR by the ZrN nanoparticles.

Chapter 3 expands on the metal nitride-SiO_2 core-shell particle system discussed in the previous chapter by extending the investigation to other metal nitrides, specifically titanium nitride (TiN) and hafnium nitride (HfN). Similar to ZrN-based systems, achieving TiN-SiO_2 core-shell particles or HfN-SiO_2 core-shell particles with uniform size was difficult, and verifying the combined effects of plasmonic and photonic interactions remained impossible.

In Chapter 4, the SiO_2 and metal nitride relations were reversed, and SiO_2-ZrN core-shell particles were fabricated. The size of SiO_2 particles used as structural materials was on the order of several hundred nanometers, whereas the metal nitride nanoparticles used as wavelength-absorbing components were just a few tens of nanometers in size. The structural colors of the resulting particle-assembled films were evaluated. Compared to the reflection spectra of particle-packed films composed of SiO_2 particles only, the reflection spectra of SiO_2-ZrN core-shell particle-stacked films exhibited lower angular dependence. The optical properties of SiO_2-ZrN core-shell particle-stacked films demonstrated the combined effects of the LSPR by the ZrN nanoparticles used as shells and the photonic effects arising from the uniformity of SiO_2 particle sizes.

Chapter 5 further extended the study to include TiN and HfN as metal nitride species, evaluating the optical properties of the core-shell particles. The prepared structural color materials exhibited low angular dependence and plasmonic-photonic coupling effects, with tunable coloration controlled by three parameters: the type of metal nitride, the distribution density of metal nitride nanoparticles, and the particle size of SiO_2.

As mentioned above, this dissertation has explored the synthesis and characterization of core-shell particles containing metal nitride nanoparticles and SiO_2 for use in structural color materials. The chapters addressed the preparation of particles that exhibited LSPR by metal nitride nanoparticles and maintained a uniform particle size, which is crucial for exhibiting photonic properties.

Preparing core-shell particles using ZrN nanoparticles as core highlighted difficulties in the uniformity of ZrN-SiO_2 core-shell particles, and subsequent chapters expanded the scope to

include TiN and HfN nanoparticles as the core, providing a broader understanding of the preparation and characterization of metal nitride-SiO_2 core-shell particles. TiN-SiO_2 core-shell particles, ZrN-SiO_2 core-shell particles, and HfN-SiO_2 core-shell particles were prepared, and opportunities for tuning the plasmonic properties of metal nitride-SiO_2 core-shell particles through control of reaction time were indicated.

By adhering metal nitride to the surroundings of monodisperse SiO_2, the production of SiO_2-metal nitride core-shell particles was achieved. The SiO_2-metal nitride core-shell particles were prepared by attaching an amount of metal nitride nanoparticles around monodisperse SiO_2 core particles that did not significantly affect the monodispersity of the whole particles. As a result, although the diameter of the core-shell particles was slightly larger than that of the SiO_2 particles alone, the overall monodispersity was maintained. These SiO_2-metal nitride core-shell particles demonstrated specific wavelength range absorption attributable to LSPR of the metal nitride nanoparticles. The reflection spectra of SiO_2-metal nitride core-shell particle-stacked films exhibited low angular dependence. The reflection spectra of the particle-stacked films showed that the specific wavelength reflections caused by the periodic structures were tuned by the LSPR in metal nitride nanoparticles. This indicated that the fabricated SiO_2-metal nitride core-shell particle-stacked films exhibited photonic-plasmonic coupling properties. The photonic properties were controlled by the size of the core particles, while the plasmonic properties were adjusted based on the metal types of metal nitrides and the distribution density of metal nitride present. A photonic–plasmonic coupling color material was constructed, which combined the structural colors of a particle system with specific wavelength range absorption by the LSPR in metal nitride nanoparticles. This material featured tunable optical properties, controlled by three

elements: the size of the core particles, the types of metal nitrides, and the distribution density of metal nitride particles.

Future research will need to control the wider range of chromaticity and assess these materials' mechanical strength and chemical durability for use as colorants. Additionally, the potential uses of these materials extend beyond mere colorants to include applications such as photocatalytic materials that combine photonic and plasmonic properties.

This study on the construction of particle-based structural color materials integrating photonic and plasmonic properties contributes to the field of materials science by demonstrating the feasibility of using metal nitride nanoparticles in structural color applications, opening new pathways for developing colorants with tunable optical properties. Furthermore, materials with photonic-plasmonic coupling properties set the stage for the development of further functional materials leveraging these optical properties.

ACKOWLEDGMENT

At this moment, I would like to express my sincere gratitude to the many individuals who have supported me throughout my Ph.D. journey.

First and foremost, I wish to thank my supervisor, Prof. Kiyoharu Tadanaga, for providing me with the opportunity to embark on this incredible journey. He introduced me to the fascinating field of inorganic materials chemistry and guided me with his profound philosophy of research. It has been an honor and a privilege to have him as my supervisor.

I would also like to extend my heartfelt thanks to my exceptional collaborators. Dr. Milena Lama made significant contributions to the evaluation of the angular dependence of the samples, while Dr. Yongming Wang's expertise in TEM was invaluable for observing the samples. I am also deeply grateful to Ms. Yuko Mori and Ms. Naomi Hirai for their assistance with STEM observations, and to Mr. Atsuki Sawa for his support with FIB-SEM operations. My thanks also go to Mr. Daisuke Yazaki for his help with Raman spectroscopy measurements and to Mr. Satoru Kimura for his assistance with FT-IR spectroscopy. Additionally, I am grateful to Mr. Tomokazu Yoshizawa for his help with SAXS measurements and to Mr. Ryohei Takizawa and Dr. Yuichi Kitagawa for their support in measuring UV-Vis/NIR absorption spectrum.

I would like to express my gratitude to the members of my Ph.D. thesis jury for their insightful discussions and encouraging feedback.

My appreciation also goes to Dr. Takayuki Nonoyama and Prof. Jian Ping Gong for their invaluable guidance during my internship at the Graduate School of Advanced Life Science, Hokkaido University.

I am deeply grateful to Prof. Alessandro Martucci for his mentorship during my study abroad at the University of Padua in Italy. My heartfelt thanks also go to Dr. Maria Bosso, Dr. Elena Colusso, Dr. Carlotta Micale, Mr. Lorenzo Facco, and Mr. Riccardo Anversa for their kind support and assistance during my research at the University of Padua.

My gratitude extends to Prof. Koichiro Ishimori, who provided me with opportunities to gain a wide range of experiences during my graduate studies, as well as to the professors and staff of the Leading Program, including Ms. Schuko Ohtsu, for their support.

I would also like to thank the friends and research colleagues I met during my graduate studies, including Dr. Nataly Carolina Rosero Navarro, Dr. Marcela Calpa, and Ms. Sara Giraldo Montoya, whose camaraderie and collaboration enriched my experience. I am also deeply thankful to Ms. Makiko Abe, the laboratory secretary, for her administrative assistance, which was crucial for the smooth progression of my studies. I am equally indebted to the members of the laboratory I belong to. I feel especially fortunate to have had the opportunity to work alongside and form bonds with Fumiya Hoshino, Yohei Saika, Wakana Kobayashi, and Shota Sugioa.

Most importantly, I wish to thank my parents, Sachiyo Noguchi and Katsuyasu Noguchi. Their love, devotion, and understanding have been my constant source of strength. Without their encouragement, I could not pursue my dreams and arrived at this point.

Last but not least, I extend my heartfelt gratitude to my peer, Tong Fang. She has been my greatest source of encouragement throughout my doctoral journey. Her unwavering support and kindness were the light that brightened the dark in my Ph.D. journey, bringing color to my world. Thanks to her, I was able to come this far. With her by my side, I feel confident in facing any challenges that life may bring.

REFERENCES

(1) Hovers, E.; Ilani, S.; Bar-Yosef, O.; Vandermeersch, B. An Early Case of Color Symbolism: Ochre Use by Modern Humans in Qafzeh Cave. *Curr Anthropol* **2003**, *44* (4), 491–522. https://doi.org/10.1086/375869.

(2) Berke, H. Chemistry in Ancient Times: The Development of Blue and Purple Pigments. *Angewandte Chemie - International Edition*. July 15, 2002, pp 2483–2487. https://doi.org/10.1002/1521-3773(20020715)41:14<2483::AID-ANIE2483>3.0.CO;2-U.

(3) Mocquard, J.; Le Lamer, A. C.; Fabre, P. L.; Mathieu, C.; Chastrette, C.; Vitrai, A.; Vandenbossche, V. Indigo Dyeing from Isatis Tinctoria L.: From Medieval to Modern Use. *Dyes and Pigments*. Elsevier Ltd November 1, 2022. https://doi.org/10.1016/j.dyepig.2022.110675.

(4) Hatton, G. D.; Shortland, A. J.; Tite, M. S. The Production Technology of Egyptian Blue and Green Frits from Second Millennium BC Egypt and Mesopotamia. *J Archaeol Sci* **2008**, *35* (6), 1591–1604. https://doi.org/10.1016/j.jas.2007.11.008.

(5) Jackson, C. M. Making Colourless Glass in the Roman Period. *Archaeometry* **2005**, *47* (4), 763–780. https://doi.org/10.1111/j.1475-4754.2005.00231.x.

(6) Mounier, A.; Daniel, F. Pigments & Dyes in a Collection of Medieval Illuminations (14th–16th Century). *Color Res Appl* **2017**, *42* (6), 807–822. https://doi.org/10.1002/col.22146.

(7) Aislin, E. (; Reynolds,). *The Development of Stained Glass in Gothic Cathedrals*; 2012; Vol. 4. http://scholarspace.jccc.edu/honors_journalhttp://scholarspace.jccc.edu/honors_journal/vol4/iss1/3.

(8) Runge, F. F. Ueber Einige Produkte Der Steinkohlendestillation. *Annalen der Physik und Chemie* **1834**, *31* (5), 308–328.

(9) John J. Beer. A. W. Hofmann and the Founding of the Royal College of Chemistry. *J Chem Educ* **1960**, *37* (5), 248.

(10) Travis, A. S. Perkin's Mauve: Ancestor of the Organic Chemical Industry. *Technol Cult* **1990**, *31* (1), 51–82. https://doi.org/10.2307/3105760.

(11) Rosati, A.; Fedel, M.; Rossi, S. NIR Reflective Pigments for Cool Roof Applications: A Comprehensive Review. *Journal of Cleaner Production*. Elsevier Ltd September 1, 2021. https://doi.org/10.1016/j.jclepro.2021.127826.

(12) Ashfaq, A.; Anjum, Z.; Younis, K. Chapter 5 - Natural Pigments-Based Biodegradable Food Packaging Films. In *Renewable Dyes and Pigments*; Ul Islam, S., Ed.; Elsevier, 2024; pp 77–92. https://doi.org/https://doi.org/10.1016/B978-0-443-15213-9.00005-3.

(13) Benkhaya, S.; M'rabet, S.; El Harfi, A. Classifications, Properties, Recent Synthesis and Applications of Azo Dyes. *Heliyon*. Elsevier Ltd January 1, 2020. https://doi.org/10.1016/j.heliyon.2020.e03271.

(14) Dahlen, M. A. *A New Class of Synthetic Pigments and Dyes*. https://pubs.acs.org/sharingguidelines.

(15) Borges, M. E.; Tejera, R. L.; Díaz, L.; Esparza, P.; Ibáñez, E. Natural Dyes Extraction from Cochineal (Dactylopius Coccus). New Extraction Methods. In *Food Chemistry*; 2012; Vol. 132, pp 1855–1860. https://doi.org/10.1016/j.foodchem.2011.12.018.

(16) Habib, N.; Batool, F.; Adeel, S.; Naveed, M.; Ali, A.; Mia, R.; Assiri, M. A. Green Extraction and Application of Yellow Natural Curcumin Colorant from Curcuma Aromatica Rhizomes for Silk Dyeing. *Sci Rep* **2024**, *14* (1). https://doi.org/10.1038/s41598-024-63927-7.
(17) Groeneveld, I.; Kanelli, M.; Ariese, F.; van Bommel, M. R. Parameters That Affect the Photodegradation of Dyes and Pigments in Solution and on Substrate – An Overview. *Dyes and Pigments*. Elsevier Ltd February 1, 2023. https://doi.org/10.1016/j.dyepig.2022.110999.
(18) Pfaff, G. Iron Oxide Pigments. *Physical Sciences Reviews* **2021**, *6* (10), 535–548. https://doi.org/doi:10.1515/psr-2020-0179.
(19) Pfaff, G. Titanium Dioxide Pigments. *Physical Sciences Reviews* **2021**, *6* (11), 679–696. https://doi.org/doi:10.1515/psr-2020-0199.
(20) Akira Fujishima; Kenichi Honda. Electrochemical Photolysis of Water at a Semiconductor Electrode. *Nature* **1972**, *238*, 37–38.
(21) Pfaff, G. Cadmium Sulfide / Selenide Pigments. *Physical Sciences Reviews* **2021**, *6* (6), 211–216. https://doi.org/doi:10.1515/psr-2020-0151.
(22) Pfaff, G. Chromium Oxide Pigments. *Physical Sciences Reviews* **2022**, *7* (2), 103–108. https://doi.org/doi:10.1515/psr-2020-0159.
(23) Pfaff, G. Ultramarine Pigments. *Physical Sciences Reviews* **2021**, *6* (12), 879–885. https://doi.org/doi:10.1515/psr-2020-0201.
(24) Pfaff, G. The World of Inorganic Pigments. *ChemTexts*. Springer Science and Business Media Deutschland GmbH August 1, 2022. https://doi.org/10.1007/s40828-022-00166-1.
(25) Li, R.; Zhang, S.; Zhang, R. Recent Progress in Artificial Structural Colors and Their Applications in Fibers and Textiles. *Chemistry-Methods*. John Wiley and Sons Inc September 1, 2023. https://doi.org/10.1002/cmtd.202200081.
(26) Zhang, D.; Zhang, W.; Gu, J.; Fan, T.; Liu, Q.; Su, H.; Zhu, S. Inspiration from Butterfly and Moth Wing Scales: Characterization, Modeling, and Fabrication. *Progress in Materials Science*. Elsevier Ltd 2015, pp 67–96. https://doi.org/10.1016/j.pmatsci.2014.10.003.
(27) Stavenga, D. G.; Leertouwer, H. L.; Marshall, N. J.; Osorio, D. Dramatic Colour Changes in a Bird of Paradise Caused by Uniquely Structured Breast Feather Barbules. *Proceedings of the Royal Society B: Biological Sciences* **2010**, *278* (1715), 2098–2104. https://doi.org/10.1098/rspb.2010.2293.
(28) The Editors of Encyclopaedia Britannica. Rayleigh Scattering. *Encyclopedia Britannica*; 2023.
(29) Gustav Mie. Beiträge Zur Optik Trüber Medien, Speziell Kolloidaler Metallösungen. *Ann Phys* **1908**, *330* (3), 377–445. https://doi.org/10.1002/andp.19083300302.
(30) Shang, L.; Zhang, W.; Xu, K.; Zhao, Y. Bio-Inspired Intelligent Structural Color Materials. *Materials Horizons*. Royal Society of Chemistry June 1, 2019, pp 945–958. https://doi.org/10.1039/c9mh00101h.
(31) Kirchner, E.; Cramer, W. Making Sense of Measurement Geometries for Multi-Angle Spectrophotometers. *Color Res Appl* **2012**, *37* (3), 186–198. https://doi.org/10.1002/col.20679.
(32) Hunter, R. S. Photoelectric Color Difference Meter*. *J Opt Soc Am* **1958**, *48* (12), 985–995. https://doi.org/10.1364/JOSA.48.000985.

(33) Bull, D. R.; Zhang, F. Chapter 4 - Digital Picture Formats and Representations. In *Intelligent Image and Video Compression (Second Edition)*; Bull, D. R., Zhang, F., Eds.; Academic Press: Oxford, 2021; pp 107–142. https://doi.org/https://doi.org/10.1016/B978-0-12-820353-8.00013-X.
(34) T Smith; J Guild. The C.I.E. Colorimetric Standards and Their Use. *Transactions of the Optical Society* **1931**, *33* (3), 73. https://doi.org/10.1088/1475-4878/33/3/301.
(35) Ramanath, R.; Kuehni, R. G.; Snyder, W. E.; Hinks, D. Spectral Spaces and Color Spaces. *Color Res Appl* **2004**, *29* (1), 29–37. https://doi.org/10.1002/col.10211.
(36) KAMIYAMA, M.; TAGUCHI, A. HSI Color Space with Same Gamut of RGB Color Space. *IEICE Transactions on Fundamentals of Electronics, Communications and Computer Sciences* **2017**, *E100.A* (1), 341–344. https://doi.org/10.1587/transfun.E100.A.341.
(37) Chen, Z.; Wang, Z.; Sheng, B.; Li, C.; Shen, R.; Li, P. Dynamic RGB-to-CMYK Conversion Using Visual Contrast Optimisation. *IET Image Process* **2017**, *11* (7), 539–549. https://doi.org/10.1049/iet-ipr.2016.0989.
(38) Lei, T.; Wang, Y.; Fan, Y.; Zhao, J. Vector Morphological Operators in HSV Color Space. *Science China Information Sciences* **2013**, *56* (1), 1–12. https://doi.org/10.1007/s11432-011-4475-5.
(39) Falomir, Z.; Museros, L.; Gonzalez-Abril, L.; Sanz, I. A Model for Qualitative Colour Comparison Using Interval Distances. *Displays* **2013**, *34* (4), 250–257. https://doi.org/10.1016/j.displa.2013.07.004.
(40) McLAREN, K. XIII—The Development of the CIE 1976 (L* A* B*) Uniform Colour Space and Colour-Difference Formula. *Journal of the Society of Dyers and Colourists* **1976**, *92* (9), 338–341. https://doi.org/https://doi.org/10.1111/j.1478-4408.1976.tb03301.x.
(41) Billmeyer Jr., F. W. Color Science: Concepts and Methods, Quantitative Data and Formulae, 2nd Ed., by Gunter Wyszecki and W. S. Stiles, John Wiley and Sons, New York, 1982, 950 Pp. Price: $75.00. *Color Res Appl* **1983**, *8* (4), 262–263. https://doi.org/https://doi.org/10.1002/col.5080080421.
(42) BORN, M. A. X.; WOLF, E. CHAPTER VII - ELEMENTS OF THE THEORY OF INTERFERENCE AND INTERFEROMETERS. In *Principles of Optics (Sixth Edition)*; BORN, M. A. X., WOLF, E., Eds.; Pergamon, 1980; pp 256–369. https://doi.org/https://doi.org/10.1016/B978-0-08-026482-0.50014-1.
(43) Wu, J.; Zhu, J. One-Step Preparation of Color-Tuned Surface Coatings on Magnesium Alloy with Corrosion Resistance. *J Alloys Compd* **2024**, *976*. https://doi.org/10.1016/j.jallcom.2023.173300.
(44) Liu, L.; Lei, J.; Li, L.; Zhang, X.; Li, N.; Pan, F. Constructing Colorful Surfaces with Mechanical Robustness for Magnesium Alloys via a Reagent-Free Method. *ACS Appl Mater Interfaces* **2020**, *12* (42), 48206–48215. https://doi.org/10.1021/acsami.0c14359.
(45) Margaret A. Duncan; Landin Barney; Mariama Rebello Sousa Dias; Marina S. Leite. Refractory Metals and Oxides for High-Temperature Structural Color Filters. *ACS Appl Mater Interfaces* **2022**, *14* (50), 55745–55752. https://doi.org/10.1021/acsami.2c14613.
(46) Kats, M. A.; Sharma, D.; Lin, J.; Genevet, P.; Blanchard, R.; Yang, Z.; Qazilbash, M. M.; Basov, D. N.; Ramanathan, S.; Capasso, F. Ultra-Thin Perfect Absorber Employing a Tunable Phase Change Material. *Appl Phys Lett* **2012**, *101* (22). https://doi.org/10.1063/1.4767646.

(47) Kats, M. A.; Blanchard, R.; Genevet, P.; Capasso, F. Nanometre Optical Coatings Based on Strong Interference Effects in Highly Absorbing Media. *Nat Mater* **2013**, *12* (1), 20–24. https://doi.org/10.1038/nmat3443.
(48) Luo, J.; Li, S.; Hou, B.; Lai, Y. Loss/Gain-Induced Ultrathin Antireflection Coatings. *Sci Rep* **2016**, *6*. https://doi.org/10.1038/srep28681.
(49) Kats, M. A.; Byrnes, S. J.; Blanchard, R.; Kolle, M.; Genevet, P.; Aizenberg, J.; Capasso, F. Enhancement of Absorption and Color Contrast in Ultra-Thin Highly Absorbing Optical Coatings. *Appl Phys Lett* **2013**, *103* (10). https://doi.org/10.1063/1.4820147.
(50) England, G. T.; Russell, C.; Shirman, E.; Kay, T.; Vogel, N.; Aizenberg, J. The Optical Janus Effect: Asymmetric Structural Color Reflection Materials. *Advanced Materials* **2017**, *29* (29). https://doi.org/10.1002/adma.201606876.
(51) Sahiner, N.; Butun, S.; Ilgin, P. Hydrogel Particles with Core Shell Morphology for Versatile Applications: Environmental, Biomedical and Catalysis. *Colloids Surf A Physicochem Eng Asp* **2011**, *386* (1–3), 16–24. https://doi.org/10.1016/J.COLSURFA.2011.06.023.
(52) H. Angus MacLeod. *Thin-Film Optical Filters*; Series in Optics and Optoelectronics; CRC Press, 2001.
(53) Wei, H.; Xu, Q.; Chen, D.; Chen, M.; Chang, M.; Ye, X. Easy Preparation of Anodic Aluminum Oxide Photonic Crystal Films with Tunable Structural Colors. *Opt Mater (Amst)* **2021**, *122*. https://doi.org/10.1016/j.optmat.2021.111722.
(54) Bu, Y.; Ou, W.; Bu, X.; Xiao, X.; Chen, Y.; Mao, Z.; Lu, J. Bio-Inspired Homologous Magnesium-Based Reflective Filters with Angular Heterochromatic Structural Colors. *Adv Opt Mater* **2023**, *11* (20). https://doi.org/10.1002/adom.202300674.
(55) Priscilla, N.; Smith, D.; Della Gaspera, E.; Song, J.; Wesemann, L.; James, T.; Roberts, A. Optical Janus Effect in Large Area Multilayer Plasmonic Films. *Adv Photonics Res* **2022**, *3* (5). https://doi.org/10.1002/adpr.202100333.
(56) Park, C. S.; Shrestha, V. R.; Lee, S. S.; Choi, D. Y. Trans-Reflective Color Filters Based on a Phase Compensated Etalon Enabling Adjustable Color Saturation. *Sci Rep* **2016**, *6*. https://doi.org/10.1038/srep25496.
(57) Chen, J.; Wang, Z.; Liu, C.; Chen, Z.; Tang, X.; Wu, Q.; Zhang, S.; Song, G.; Cong, S.; Chen, Q.; Zhao, Z. Mimicking Nature's Butterflies: Electrochromic Devices with Dual-Sided Differential Colorations. *Advanced Materials* **2021**, *33* (14). https://doi.org/10.1002/adma.202007314.
(58) Wu, B.; Liu, Z.; Liu, X.; Liu, G.; Tang, P.; Yuan, W.; Fu, G. Large-Scale Reflective Optical Janus Color Materials. *Nanotechnology* **2020**, *31* (22). https://doi.org/10.1088/1361-6528/ab7649.
(59) Kang, Y.; Walish, J. J.; Gorishnyy, T.; Thomas, E. L. Broad-Wavelength-Range Chemically Tunable Block-Copolymer Photonic Gels. *Nature Materials*. Nature Publishing Group 2007, pp 957–960. https://doi.org/10.1038/nmat2032.
(60) Yue, Y.; Kurokawa, T.; Haque, A.; Nakajima, T.; Nonoyama, T.; Li, X.; Kajiwara, I.; Gong, J. P. Mechano-Actuated Ultrafast Full-Colour Switching in Layered Photonic Hydrogels. *Nat Commun* **2014**, *5* (4659). https://doi.org/10.1038/ncomms5659.
(61) Novotny, L.; Hecht, B. *Principles of Nano-Optics*; Principles of Nano-optics; Cambridge University Press, 2012.
(62) Yu, T.; Bi, J.; Wei, W.; Su, X. Monodisperse Colloidal Spheres with a High Refractive Index: Their Synthesis, Assembly and Application in Structural Colored Materials.

Journal of Materials Chemistry C. Royal Society of Chemistry October 21, 2022, pp 17451–17471. https://doi.org/10.1039/d2tc03726b.
(63) Zhu, K.; Fang, C.; Pu, M.; Song, J.; Wang, D.; Zhou, X. Recent Advances in Photonic Crystal with Unique Structural Colors: A Review. *Journal of Materials Science and Technology*. Chinese Society of Metals April 1, 2023, pp 78–99. https://doi.org/10.1016/j.jmst.2022.08.044.
(64) Du, X.; He, J. Facile Size-Controllable Syntheses of Highly Monodisperse Polystyrene Nano- and Microspheres by Polyvinylpyrrolidone-Mediated Emulsifier-Free Emulsion Polymerization. *J Appl Polym Sci* **2008**, *108* (3), 1755–1760. https://doi.org/10.1002/app.27774.
(65) Gu, Z. Z.; Chen, H.; Zhang, S.; Sun, L.; Xie, Z.; Ge, Y. Rapid Synthesis of Monodisperse Polymer Spheres for Self-Assembled Photonic Crystals. *Colloids Surf A Physicochem Eng Asp* **2007**, *302* (1–3), 312–319. https://doi.org/10.1016/j.colsurfa.2007.02.064.
(66) Debord, J. D.; Lyon, L. A. Thermoresponsive Photonic Crystals. *Journal of Physical Chemistry B* **2000**, *104* (27), 6330–6331. https://doi.org/10.1021/jp001238c.
(67) Zhou, M.; Xing, F.; Ren, M.; Feng, Y.; Zhao, Y.; Qiu, H.; Wang, X.; Gao, C.; Sun, F.; He, Y.; Ma, Z.; Wen, P.; Gao, J. A Facile Method to Assemble PNIPAM-Containing Microgel Photonic Crystals. *ChemPhysChem* **2009**, *10* (3), 523–526. https://doi.org/10.1002/cphc.200800323.
(68) Li, F.; Tang, B.; Wu, S.; Zhang, S. Facile Synthesis of Monodispersed Polysulfide Spheres for Building Structural Colors with High Color Visibility and Broad Viewing Angle. *Small* **2017**, *13* (3). https://doi.org/10.1002/smll.201602565.
(69) Yamauchi, H.; Ishikawa, T.; Kondo, S. *Surface Characterization of Ultramicro Spherical Particles of Silica Prepared by W/O Microemulsion Method*; 1989; Vol. 37.
(70) Dubey, R. S.; Rajesh, Y. B. R. D.; More, M. A. Synthesis and Characterization of SiO2 Nanoparticles via Sol-Gel Method for Industrial Applications. In *Materials Today: Proceedings*; Elsevier Ltd, 2015; Vol. 2, pp 3575–3579. https://doi.org/10.1016/j.matpr.2015.07.098.
(71) Bogush, G. H.; Zukoski Iv, C. F. *Studies of the Kinetics of the Precipitation of Uniform Silica Particles through the Hydrolysis and Condensation of Silicon Alkoxides*; 1991.
(72) Stöber, W.; Fink, A.; Bohn, E. Controlled Growth of Monodisperse Silica Spheres in the Micron Size Range. *J Colloid Interface Sci* **1968**, *26* (1), 62–69. https://doi.org/10.1016/0021-9797(68)90272-5.
(73) Pal, M.; Serrano, J. G.; Santiago, P.; Pal, U. Size-Controlled Synthesis of Spherical TiO2 Nanoparticles: Morphology, Crystallization, and Phase Transition. *Journal of Physical Chemistry C* **2007**, *111* (1), 96–102. https://doi.org/10.1021/jp0618173.
(74) Jean, J. H.; Ring, T. A. *Nucleation and Growth of Monosized Ti02 Powders from Alcohol Solution*; 1986; Vol. 2. https://pubs.acs.org/sharingguidelines.
(75) Jeong, U.; Xia, Y. Photonic Crystals with Thermally Switchable Stop Bands Fabricated from Se@Ag2Se Spherical Colloids. *Angewandte Chemie - International Edition* **2005**, *44* (20), 3099–3103. https://doi.org/10.1002/anie.200462906.
(76) Liu, L.; Peng, Q.; Li, Y. Preparation of Monodisperse Se Colloid Spheres and Se Nanowires Using Na2SeSO3 as Precursor. *Nano Res* **2008**, *1* (5), 403–411. https://doi.org/10.1007/s12274-008-8040-5.

(77) Zhang, J.; Liu, J.; Peng, Q.; Wang, X.; Li, Y. Nearly Monodisperse Cu2O and CuO Nanospheres: Preparation and Applications for Sensitive Gas Sensors. *Chemistry of Materials* **2006**, *18* (4), 867–871. https://doi.org/10.1021/cm052256f.
(78) Bai, Y.; Yang, T.; Gu, Q.; Cheng, G.; Zheng, R. Shape Control Mechanism of Cuprous Oxide Nanoparticles in Aqueous Colloidal Solutions. *Powder Technol* **2012**, *227*, 35–42. https://doi.org/10.1016/j.powtec.2012.02.008.
(79) Zhang, S.; Jiang, R.; Xie, Y. M.; Ruan, Q.; Yang, B.; Wang, J.; Lin, H. Q. Colloidal Moderate-Refractive-Index Cu2O Nanospheres as Visible-Region Nanoantennas with Electromagnetic Resonance and Directional Light-Scattering Properties. *Advanced Materials* **2015**, *27* (45), 7432–7439. https://doi.org/10.1002/adma.201502917.
(80) Bi, J.; Wu, Y.; Li, L.; Zhang, S.; Wu, S. Asymmetric Structural Colors Based on Monodisperse Single-Crystal Cu2O Spheres. *Nanoscale* **2020**, *12* (5), 3220–3226. https://doi.org/10.1039/c9nr09472e.
(81) Wang, Y.; Cai, L.; Xia, Y. Monodisperse Spherical Colloids of Pb and Their Use as Chemical Templates to Produce Hollow Particles. *Advanced Materials* **2005**, *17* (4), 473–477. https://doi.org/10.1002/adma.200401416.
(82) Wang, Y.; Xia, Y. Bottom-up and Top-down Approaches to the Synthesis of Monodispersed Spherical Colloids of Low Melting-Point Metals. *Nano Lett* **2004**, *4* (10), 2047–2050. https://doi.org/10.1021/nl048689j.
(83) Cheng, H. M.; Hsu, H. C.; Chen, S. L.; Wu, W. T.; Kao, C. C.; Lin, L. J.; Hsieh, W. F. Efficient UV Photoluminescence from Monodispersed Secondary ZnO Colloidal Spheres Synthesized by Sol-Gel Method. *J Cryst Growth* **2005**, *277* (1–4), 192–199. https://doi.org/10.1016/j.jcrysgro.2004.12.133.
(84) Barick, K. C.; Aslam, M.; Dravid, V. P.; Bahadur, D. Self-Aggregation and Assembly of Size-Tunable Transition Metal Doped ZnO Nanocrystals. *Journal of Physical Chemistry C* **2008**, *112* (39), 15163–15170. https://doi.org/10.1021/jp802361r.
(85) Waterhouse, G. I. N.; Metson, J. B.; Idriss, H.; Sun-Waterhouse, D. Physical and Optical Properties of Inverse Opal CeO2 Photonic Crystals. *Chemistry of Materials* **2008**, *20* (3), 1183–1190. https://doi.org/10.1021/cm703005g.
(86) Kim, M. H.; Lim, B.; Lee, E. P.; Xia, Y. Polyol Synthesis of Cu2O Nanoparticles: Use of Chloride to Promote the Formation of a Cubic Morphology. *J Mater Chem* **2008**, *18* (34), 4069–4073. https://doi.org/10.1039/b805913f.
(87) Xu, Y.; Wang, H.; Yu, Y.; Tian, L.; Zhao, W.; Zhang, B. Cu2O Nanocrystals: Surfactant-Free Room-Temperature Morphology-Modulated Synthesis and Shape-Dependent Heterogeneous Organic Catalytic Activities. *Journal of Physical Chemistry C* **2011**, *115* (31), 15288–15296. https://doi.org/10.1021/jp204982q.
(88) Liu, J.; Gao, Z.; Han, H.; Wu, D.; Xu, F.; Wang, H.; Jiang, K. Mesoporous Cu 2O Submicro-Spheres, Facile Synthesis and the Selective Adsorption Properties. *Chemical Engineering Journal* **2012**, *185–186*, 151–159. https://doi.org/10.1016/j.cej.2012.01.064.
(89) Pang, M.; Zeng, H. C. Highly Ordered Self-Assemblies of Submicrometer Cu2O Spheres and Their Hollow Chalcogenide Derivatives. *Langmuir* **2010**, *26* (8), 5963–5970. https://doi.org/10.1021/la904292t.
(90) Gou, X.; Wang, G.; Park, J.; Liu, H.; Yang, J. Monodisperse Hematite Porous Nanospheres: Synthesis, Characterization, and Applications for Gas Sensors. *Nanotechnology* **2008**, *19* (12). https://doi.org/10.1088/0957-4484/19/12/125606.

(91) Zou, B.; Liu, Y.; Wang, Y. Facile Synthesis of Highly Water-Dispersible and Monodispersed Fe 3O4 Hollow Microspheres and Their Application in Water Treatment. *RSC Adv* **2013**, *3* (45), 23327–23334. https://doi.org/10.1039/c3ra42716a.
(92) Cheng, L.; Ruan, W.; Zou, B.; Liu, Y.; Wang, Y. Chemical Template-Assisted Synthesis of Monodisperse Rattle-Type Fe3O4@C Hollow Microspheres as Drug Carrier. *Acta Biomater* **2017**, *58*, 432–441. https://doi.org/10.1016/j.actbio.2017.06.007.
(93) Sugimoto, T.; Dirige, G. E.; Muramatsu, A. *Formation Mechanism of Uniform CdS Particles from Condensed Cd(OH) 2 Suspension*; 1995; Vol. 176.
(94) Griesebock, B.; Egen, M.; Zentel, R. Large Photonic Films by Crystallization on Fluid Substrates. *Chemistry of Materials* **2002**, *14* (10), 4023–4025. https://doi.org/10.1021/cm025613k.
(95) Gu, Z. Z.; Fujishima, A.; Sato, O. Fabrication of High-Quality Opal Films with Controllable Thickness. *Chemistry of Materials* **2002**, *14* (2), 760–765. https://doi.org/10.1021/cm0108435.
(96) Mayoral, R.; Requena, J.; Moya, J. S.; López, C.; Cintas, A.; Míguez, H.; Meseguer, F.; Vázquez, L.; Holgado, M.; Blanco, Á. 3D Long-Range Ordering in an SiO2 Submicrometer-Sphere Sintered Superstructure. *Advanced Materials* **1997**, *9* (3), 257–260. https://doi.org/10.1002/adma.19970090318.
(97) Han, M. G.; Shin, C. G.; Jeon, S. J.; Shim, H.; Heo, C. J.; Jin, H.; Kim, J. W.; Lee, S. Full Color Tunable Photonic Crystal from Crystalline Colloidal Arrays with an Engineered Photonic Stop-Band. *Advanced Materials* **2012**, *24* (48), 6438–6444. https://doi.org/10.1002/adma.201203211.
(98) Ge, J.; Hu, Y.; Yin, Y. Highly Tunable Superparamagnetic Colloidal Photonic Crystals. *Angewandte Chemie - International Edition* **2007**, *46* (39), 7428–7431. https://doi.org/10.1002/anie.200701992.
(99) Ge, J.; Yin, Y. Magnetically Tunable Colloidal Photonic Structures in Alkanol Solutions. *Advanced Materials* **2008**, *20* (18), 3485–3491. https://doi.org/10.1002/adma.200800657.
(100) Yang, D.; Ye, S.; Ge, J. Solvent Wrapped Metastable Colloidal Crystals: Highly Mutable Colloidal Assemblies Sensitive to Weak External Disturbance. *J Am Chem Soc* **2013**, *135* (49), 18370–18376. https://doi.org/10.1021/ja405670r.
(101) Wang, F.; Zhang, X.; Lin, Y.; Wang, L.; Qin, Y.; Zhu, J. Fabrication and Characterization of Structurally Colored Pigments Based on Carbon-Modified ZnS Nanospheres. *J Mater Chem C Mater* **2016**, *4* (15), 3321–3327. https://doi.org/10.1039/c5tc04192a.
(102) Han, Y.; Meng, Z.; Wu, Y.; Zhang, S.; Wu, S. Structural Colored Fabrics with Brilliant Colors, Low Angle Dependence, and High Color Fastness Based on the Mie Scattering of Cu2O Spheres. *ACS Appl Mater Interfaces* **2021**, *13* (48), 57796–57802. https://doi.org/10.1021/acsami.1c17288.
(103) Wang, J.; Wang, L.; Song, Y.; Jiang, L. Patterned Photonic Crystals Fabricated by Inkjet Printing. *J Mater Chem C Mater* **2013**, *1* (38), 6048–6058. https://doi.org/10.1039/c3tc30728j.
(104) McGrath, J. G.; Bock, R. D.; Cathcart, J. M.; Lyon, L. A. Self-Assembly of "Paint-on" Colloidal Crystals Using Poly(Styrene-Co-N-Isopropylacrylamide) Spheres. *Chemistry of Materials* **2007**, *19* (7), 1584–1591. https://doi.org/10.1021/cm061931y.
(105) Kuang, M.; Wang, J.; Bao, B.; Li, F.; Wang, L.; Jiang, L.; Song, Y. Inkjet Printing Patterned Photonic Crystal Domes for Wide Viewing-Angle Displays by Controlling the

Sliding Three Phase Contact Line. *Adv Opt Mater* **2014**, *2* (1), 34–38. https://doi.org/10.1002/adom.201300369.
(106) Colson, P.; Cloots, R.; Henrist, C. Experimental Design Applied to Spin Coating of 2d Colloidal Crystal Masks: A Relevant Method? *Langmuir* **2011**, *27* (21), 12800–12806. https://doi.org/10.1021/la202284a.
(107) Mihi, A.; Ocaña, M.; Míguez, H. Oriented Colloidal-Crystal Thin Films by Spin-Coating Microspheres Dispersed in Volatile Media. *Advanced Materials* **2006**, *18* (17), 2244–2249. https://doi.org/10.1002/adma.200600555.
(108) Li, X. H.; Li, J. X.; Li, G. D.; Liu, D. P.; Chen, J. S. Controlled Synthesis, Growth Mechanism, and Properties of Monodisperse CdS Colloidal Spheres. *Chemistry - A European Journal* **2007**, *13* (31), 8754–8761. https://doi.org/10.1002/chem.200700754.
(109) García, P. D.; Sapienza, R.; López, C. Photonic Glasses: A Step beyond White Paint. *Advanced Materials* **2010**, *22* (1), 12–19. https://doi.org/10.1002/adma.200900827.
(110) Forster, J. D.; Noh, H.; Liew, S. F.; Saranathan, V.; Schreck, C. F.; Yang, L.; Park, J. C.; Prum, R. O.; Mochrie, S. G. J.; O'Hern, C. S.; Cao, H.; Dufresne, E. R. Biomimetic Isotropic Nanostructures for Structural Coloration. *Advanced Materials* **2010**, *22* (26–27), 2939. https://doi.org/10.1002/adma.200903693.
(111) Aguirre, C. I.; Reguera, E.; Stein, A. Colloidal Photonic Crystal Pigments with Low Angle Dependence. *ACS Appl Mater Interfaces* **2010**, *2* (11), 3257–3262. https://doi.org/10.1021/am100704f.
(112) Noh, H.; Liew, S. F.; Saranathan, V.; Mochrie, S. G. J.; Prum, R. O.; Dufresne, E. R.; Cao, H. How Noniridescent Colors Are Generated by Quasi-Ordered Structures of Bird Feathers. *Advanced Materials* **2010**, *22* (26–27), 2871–2880. https://doi.org/10.1002/adma.200903699.
(113) Meng, F.; Wang, Z.; Zhang, S.; Ju, B.; Tang, B. Bioinspired Quasi-Amorphous Structural Color Materials toward Architectural Designs. *Cell Rep Phys Sci* **2021**, *2* (7), 100499. https://doi.org/10.1016/J.XCRP.2021.100499.
(114) Shi, L.; Zhang, Y.; Dong, B.; Zhan, T.; Liu, X.; Zi, J. Amorphous Photonic Crystals with Only Short-Range Order. *Advanced Materials* **2013**, *25* (37), 5314–5320. https://doi.org/10.1002/adma.201301909.
(115) Gu, H.; Zhao, Y.; Cheng, Y.; Xie, Z.; Rong, F.; Li, J.; Wang, B.; Fu, D.; Gu, Z. Tailoring Colloidal Photonic Crystals with Wide Viewing Angles. *Small* **2013**, *9* (13), 2266–2271. https://doi.org/10.1002/smll.201203179.
(116) Takeoka, Y. Angle-Independent Structural Coloured Amorphous Arrays. *J Mater Chem* **2012**, *22* (44), 23299–23309. https://doi.org/10.1039/c2jm33643j.
(117) Ge, D.; Yang, L.; Wu, G.; Yang, S. Spray Coating of Superhydrophobic and Angle-Independent Coloured Films. *Chemical Communications* **2014**, *50* (19), 2469–2472. https://doi.org/10.1039/c3cc48962k.
(118) Liu, B.; Fan, J.; Liu, W.; Zhang, G.; Wu, Z. Controllable in Situ Generated Carbon Black Hollow Silica (C@h-SiO2) Photonic Crystal Inks with Highly Saturated Structural Colors. *Dyes and Pigments* **2022**, *208*. https://doi.org/10.1016/j.dyepig.2022.110810.
(119) Sakai, M.; Kim, H.; Arai, Y.; Teratani, T.; Kawai, Y.; Kuwahara, Y.; Abe, K.; Kuwana, Y.; Ikeda, K.; Yamada, K.; Takeoka, Y. Monodisperse Silica Nanoparticle–Carbon Black Composite Microspheres as Photonic Pigments. *ACS Appl Nano Mater* **2020**, *3* (7), 7047–7056. https://doi.org/10.1021/acsanm.0c01366.

(120) Iwata, M.; Teshima, M.; Seki, T.; Yoshioka, S.; Takeoka, Y.; Iwata, M.; Teshima, M.; Seki, T.; Takeoka, Y.; Yoshioka, S. Bio-Inspired Bright Structurally Colored Colloidal Amorphous Array Enhanced by Controlling Thickness and Black Background. *Adv. Mater* **2017**, *29*, 1605050. https://doi.org/10.1002/adma.201605050.
(121) Xiao, M.; Li, Y.; C. Allen, M.; D. Deheyn, D.; Yue, X.; Zhao, J.; C. Gianneschi, N.; D. Shawkey, M.; Dhinojwala, A. Bio-Inspired Structural Colors Produced via Self-Assembly of Synthetic Melanin Nanoparticles. *ACS Nano* **2015**, *9* (5), 5454–5460. https://doi.org/10.1021/acsnano.5b01298.
(122) Kohri, M. Artificial Melanin Particles: New Building Blocks for Biomimetic Structural Coloration. *Polymer Journal*. Nature Publishing Group November 1, 2019, pp 1127–1135. https://doi.org/10.1038/s41428-019-0231-2.
(123) Yang, X.; Ge, D.; Wu, G.; Liao, Z.; Yang, S. Production of Structural Colors with High Contrast and Wide Viewing Angles from Assemblies of Polypyrrole Black Coated Polystyrene Nanoparticles. *ACS Applied Materials & Interfaces* **2016**, *8* (25), 16289–16295. https://doi.org/10.1021/acsami.6b03739.
(124) Katagiri, K.; Uemura, K.; Uesugi, R.; Tarutani, N.; Inumaru, K.; Uchikoshi, T.; Seki, T.; Takeoka, Y. Robust Structurally Colored Coatings Composed of Colloidal Arrays Prepared by the Cathodic Electrophoretic Deposition Method with Metal Cation Additives. *ACS Appl Mater Interfaces* **2020**, *12* (36), 40768–40777. https://doi.org/10.1021/acsami.0c10588.
(125) Yamanaka, T.; Tarutani, N.; Katagiri, K.; Inumaru, K.; Takeoka, Y.; Masui, T. High Heat Resistance of the Structural Coloration of Colloidal Arrays with Inorganic Black Additives. *ACS Appl Mater Interfaces* **2022**, *14* (25), 29324–29330. https://doi.org/10.1021/acsami.2c08649.
(126) Li, H.; Zhu, M.; Tian, F.; Hua, W.; Guo, J.; Wang, C. Polychrome Photonic Crystal Stickers with Thermochromic Switchable Colors for Anti-Counterfeiting and Information Encryption. *Chemical Engineering Journal* **2021**, *426*. https://doi.org/10.1016/j.cej.2021.130683.
(127) Yu, W.; Zhao, Y.; Sheng, W.; Ge, J. Creation of Nanotips on ITO Electrode by Nanoparticle Deposition: An Easy Way to Enhance the Performance of Electrically Responsive Photonic Crystal and Fabricate Electrically Triggered Anticounterfeiting Tags. *Adv Funct Mater* **2023**, *33* (43). https://doi.org/10.1002/adfm.202304474.
(128) Huang, H.; Li, H.; Shen, X.; Gu, K.; Guo, J.; Wang, C. Gecko-Inspired Smart Photonic Crystal Films with Versatile Color and Brightness Variation for Smart Windows. *Chemical Engineering Journal* **2022**, *429*. https://doi.org/10.1016/j.cej.2021.132437.
(129) Wang, W.; Zhou, Y.; Yang, L.; Yang, X.; Yao, Y.; Meng, Y.; Tang, B. Stimulus-Responsive Photonic Crystals for Advanced Security. *Advanced Functional Materials*. John Wiley and Sons Inc October 1, 2022. https://doi.org/10.1002/adfm.202204744.
(130) Li, Z.; Ma, T.; Li, S.; Gu, W.; Lu, L.; Yang, H.; Dai, Y.; Wang, R. High-Efficiency, Mass-Producible, and Colored Solar Photovoltaics Enabled by Self-Assembled Photonic Glass. *ACS Nano* **2022**, *16* (7), 11473–11482. https://doi.org/10.1021/acsnano.2c05840.
(131) Feng, M.; Bu, X.; Yang, J.; Li, D.; Zhang, Z.; Dai, Y.; Zhang, X. Review: Smart Windows Based on Photonic Crystals. *J Mater Sci* **2020**, *55* (20), 8444–8463. https://doi.org/10.1007/s10853-020-04460-6.

(132) Li, H.; Zhao, G.; Zhu, M.; Guo, J.; Wang, C. Robust Large-Sized Photochromic Photonic Crystal Film for Smart Decoration and Anti-Counterfeiting. *ACS Appl Mater Interfaces* **2022**, *14* (12), 14618–14629. https://doi.org/10.1021/acsami.2c01211.
(133) Kim, T.; Yu, E. S.; Bae, Y. G.; Lee, J.; Kim, I. S.; Chung, S.; Lee, S. Y.; Ryu, Y. S. Asymmetric Optical Camouflage: Tuneable Reflective Colour Accompanied by the Optical Janus Effect. *Light Sci Appl* **2020**, *9* (1). https://doi.org/10.1038/s41377-020-00413-5.
(134) Zhang, X.; Liu, C.; Zhang, L.; Jia, L.; Shi, M.; Chen, L.; Di, Y.; Gan, Z. Bioinspired Tunable Structural Color Film with Janus Wettability and Interfacial Floatability towards Visible Water Quality Monitoring. *Adv Funct Mater* **2021**, *31* (20). https://doi.org/10.1002/adfm.202010406.
(135) Zhang, X.; Liu, Y.; Lee, S. T.; Yang, S.; Kang, Z. Coupling Surface Plasmon Resonance of Gold Nanoparticles with Slow-Photon-Effect of TiO2 Photonic Crystals for Synergistically Enhanced Photoelectrochemical Water Splitting. In *Energy and Environmental Science*; Royal Society of Chemistry, 2014; Vol. 7, pp 1409–1419. https://doi.org/10.1039/c3ee43278e.
(136) Dinh, C. T.; Yen, H.; Kleitz, F.; Do, T. O. Three-Dimensional Ordered Assembly of Thin-Shell Au/TiO2 Hollow Nanospheres for Enhanced Visible-Light-Driven Photocatalysis. *Angewandte Chemie - International Edition* **2014**, *53* (26), 6618–6623. https://doi.org/10.1002/anie.201400966.
(137) Meng, S.; Li, D.; Fu, X.; Fu, X. Integrating Photonic Bandgaps with Surface Plasmon Resonance for the Enhancement of Visible-Light Photocatalytic Performance. *J Mater Chem A Mater* **2015**, *3* (46), 23501–23511. https://doi.org/10.1039/c5ta06955f.
(138) Zhang, Z.; Zhang, L.; Hedhili, M. N.; Zhang, H.; Wang, P. Plasmonic Gold Nanocrystals Coupled with Photonic Crystal Seamlessly on TiO2 Nanotube Photoelectrodes for Efficient Visible Light Photoelectrochemical Water Splitting. *Nano Lett* **2013**, *13* (1), 14–20. https://doi.org/10.1021/nl3029202.
(139) Collins, G.; Lonergan, A.; McNulty, D.; Glynn, C.; Buckley, D.; Hu, C.; O'Dwyer, C. Semiconducting Metal Oxide Photonic Crystal Plasmonic Photocatalysts. *Adv Mater Interfaces* **2020**, *7* (8), 1901805. https://doi.org/10.1002/admi.201901805.
(140) Raja Mogan, T.; Zhang, J.; Ng, L. S.; Boong, S. K.; Chong, C.; Lee, J. K.; Li, H.; Lee, H. K. Harmonizing Plasmonic and Photonic Effects to Boost Photocatalytic H2 Production over 550 Mmol · H−1 · Gcat−1. *Angewandte Chemie - International Edition* **2024**, *63* (16). https://doi.org/10.1002/anie.202401277.
(141) Han, J.; Lee, E.; Dudoff, J. K.; Bagge-Hansen, M.; Lee, J. R. I.; Pascall, A. J.; Kuntz, J. D.; Willey, T. M.; Worsley, M. A.; Han, T. Y. J. Tunable Amorphous Photonic Materials with Pigmentary Colloidal Nanostructures. *Adv Opt Mater* **2017**, *5* (7). https://doi.org/10.1002/adom.201600838.
(142) Welling, T. A. J.; Kurioka, K.; Namigata, H.; Suga, K.; Nagao, D.; Watanabe, K. Highly Reflective and Transparent Shell-Index-Matched Colloidal Crystals of Core-Shell Particles for Stacked RGB Films. *ACS Applied Nano Materials*. American Chemical Society August 23, 2024, pp 18337–18345. https://doi.org/10.1021/acsanm.3c03940.
(143) Underwood, S.; Mulvaney, P. *Effect of the Solution Refractive Index on the Color of Gold Colloids*; 1994; Vol. 10. https://pubs.acs.org/sharingguidelines.
(144) Nehl, C. L.; Liao, H.; Hafner, J. H. Optical Properties of Star-Shaped Gold Nanoparticles. *Nano Lett* **2006**, *6* (4), 683–688. https://doi.org/10.1021/nl052409y.

(145) Yonzon, C. R.; Jeoung, E.; Zou, S.; Schatz, G. C.; Mrksich, M.; Van Duyne, R. P. A Comparative Analysis of Localized and Propagating Surface Plasmon Resonance Sensors: The Binding of Concanavalin A to a Monosaccharide Functionalized Self-Assembled Monolayer. *J Am Chem Soc* **2004**, *126* (39), 12669–12676. https://doi.org/10.1021/ja047118q.
(146) Mock, J. J.; Smith, D. R.; Schultz, S. Local Refractive Index Dependence of Plasmon Resonance Spectra from Individual Nanoparticles. *Nano Lett* **2003**, *3* (4), 485–491. https://doi.org/10.1021/nl0340475.
(147) Xiong, Y.; McLellan, J. M.; Chen, J.; Yin, Y.; Li, Z. Y.; Xia, Y. Kinetically Controlled Synthesis of Triangular and Hexagonal Nanoplates of Palladium and Their SPR/SERS Properties. *J Am Chem Soc* **2005**, *127* (48), 17118–17127. https://doi.org/10.1021/ja056498s.
(148) Lu, X.; Rycenga, M.; Skrabalak, S. E.; Wiley, B.; Xia, Y. Chemical Synthesis of Novel Plasmonic Nanoparticles. *Annual Review of Physical Chemistry*. Annual Reviews Inc. 2009, pp 167–192. https://doi.org/10.1146/annurev.physchem.040808.090434.
(149) Mayer, K. M.; Hafner, J. H. Localized Surface Plasmon Resonance Sensors. *Chemical Reviews*. June 8, 2011, pp 3828–3857. https://doi.org/10.1021/cr100313v.
(150) Bohren, C. F.; Huffman, D. R. Frontmatter. In *Absorption and Scattering of Light by Small Particles*; Wiley, 1998. https://doi.org/10.1002/9783527618156.fmatter.
(151) Anderson, L. J. E.; Mayer, K. M.; Fraleigh, R. D.; Yang, Y.; Lee, S.; Hafner, J. H. Quantitative Measurements of Individual Gold Nanoparticle Scattering Cross Sections. *Journal of Physical Chemistry C* **2010**, *114* (25), 11127–11132. https://doi.org/10.1021/jp1040663.
(152) Jensen, T. R.; Duval, M. L.; Lance Kelly, K.; Lazarides, A. A.; Schatz, G. C.; Van Duyne, R. P. Nanosphere Lithography: Effect of the External Dielectric Medium on the Surface Plasmon Resonance Spectrum of a Periodic Array of Silver Nanoparticles. *Journal of Physical Chemistry B* **1999**, *103* (45), 9846–9853. https://doi.org/10.1021/jp9926802.
(153) Koay, N.; Burgess, I. B.; Kay, T. M.; Nerger, B. A.; Miles-Rossouw, M.; Shirman, T.; Vu, T. L.; England, G.; Phillips, K. R.; Utech, S.; Vogel, N.; Kolle, M.; Aizenberg, J. Hierarchical Structural Control of Visual Properties in Self-Assembled Photonic-Plasmonic Pigments. *Opt Express* **2014**, *22* (23), 27750. https://doi.org/10.1364/oe.22.027750.
(154) Ung, T.; Liz-Marzán, L. M.; Mulvaney, P. Gold Nanoparticle Thin Films. *Colloids Surf A Physicochem Eng Asp* **2002**, *202* (2–3), 119–126. https://doi.org/10.1016/S0927-7757(01)01083-4.
(155) Wang, W.; A. Asher, S. Photochemical Incorporation of Silver Quantum Dots in Monodisperse Silica Colloids for Photonic Crystal Applications. *J Am Chem Soc* **2001**, *123* (50), 12528–12535. https://doi.org/10.1021/ja011262j.
(156) Wang, Y.; Kim, B. J.; Guidetti, G.; Omenetto, F. G. Generation of Complex Tunable Multispectral Signatures with Reconfigurable Protein-Based, Plasmonic-Photonic Crystal Hybrid Nanostructures. *Small* **2022**, *18* (22). https://doi.org/10.1002/smll.202201036.
(157) Qi, W. H.; Wang, M. P. Size and Shape Dependent Melting Temperature of Metallic Nanoparticles. *Mater Chem Phys* **2004**, *88* (2–3), 280–284. https://doi.org/10.1016/j.matchemphys.2004.04.026.
(158) Fu, Q.; Cui, Z.; Xue, Y.; Duan, H. Research of Size- and Shape-Dependent Thermodynamic Properties of the Actual Melting Process of Nanoparticles. *Journal of*

Physical Chemistry C **2018**, *122* (27), 15713–15722. https://doi.org/10.1021/acs.jpcc.8b03085.
(159) Alexandra Boltasseva; Harry A. Atwater. Low-Loss Plasmonic Metamaterials. *Science*. January 21, 2011, pp 290–291. https://doi.org/10.1126/science.1201291.
(160) Urcan Guler; Alexandra Boltasseva; Vladimir M. Shalaev. Refractory Plasmonics. *Science*. American Association for the Advancement of Science 2014, pp 263–264. https://doi.org/10.1126/science.1246736.
(161) Naik, G. V.; Shalaev, V. M.; Boltasseva, A. Alternative Plasmonic Materials: Beyond Gold and Silver. *Advanced Materials*. June 25, 2013, pp 3264–3294. https://doi.org/10.1002/adma.201205076.
(162) Kumar, M.; Umezawa, N.; Ishii, S.; Nagao, T. Examining the Performance of Refractory Conductive Ceramics as Plasmonic Materials: A Theoretical Approach. *ACS Photonics* **2016**, *3* (1), 43–50. https://doi.org/10.1021/acsphotonics.5b00409.
(163) Karaballi, R. A.; Humagain, G.; Fleischman, B. R. A.; Dasog, M.; Karaballi, R. A.; Humagain, G.; Fleischman, B. R. A.; Dasog, P. R. M. Synthesis of Plasmonic Group-4 Nitride Nanocrystals by Solid-State Metathesis. *Angewandte Chemie* **2019**, *58*, 3147–3150. https://doi.org/10.1002/ange.201813134.
(164) Reinholdt, A.; Pecenka, R.; Pinchuk, A.; Runte, S.; Stepanov, A. L.; Weirich, Th. E.; Kreibig, U. Structural, Compositional, Optical and Colorimetric Characterization of TiN-Nanoparticles. *The European Physical Journal D - Atomic, Molecular, Optical and Plasma Physics* **2004**, *31* (1), 69–76. https://doi.org/10.1140/epjd/e2004-00129-8.
(165) Reinholdt, A.; Detemple, R.; Stepanov, A. L.; Weirich, T. E.; Kreibig, U. Novel Nanoparticle Matter: ZrN-Nanoparticles. *Appl Phys B* **2003**, *77* (6–7), 681–686. https://doi.org/10.1007/s00340-003-1298-0.
(166) Kortshagen, U. R.; Sankaran, R. M.; Pereira, R. N.; Girshick, S. L.; Wu, J. J.; Aydil, E. S. Nonthermal Plasma Synthesis of Nanocrystals: Fundamental Principles, Materials, and Applications. *Chemical Reviews*. American Chemical Society September 28, 2016, pp 11061–11127. https://doi.org/10.1021/acs.chemrev.6b00039.
(167) Taylor, P. R.; Pirzada, S. A. *Thermal Plasma Processing of Materials: A Review*; 1994; Vol. 1.
(168) Gschwend, P. M.; Conti, S.; Kaech, A.; Maake, C.; Pratsinis, S. E. Silica-Coated TiN Particles for Killing Cancer Cells. *ACS Appl Mater Interfaces* **2019**, *11* (25), 22550–22560. https://doi.org/10.1021/acsami.9b07239.
(169) Song, H. D.; Lee, M.; Kim, G. P.; Choi, I.; Yi, J. Real-Time Optical Monitoring of Pt Catalyst under the Potentiodynamic Conditions. *Sci Rep* **2016**, *6*. https://doi.org/10.1038/srep38847.
(170) Khatami, M.; Alijani, H. Q.; Nejad, M. S.; Varma, R. S. Core@shell Nanoparticles: Greener Synthesis Using Natural Plant Products. *Applied Sciences*. MDPI AG March 10, 2018. https://doi.org/10.3390/app8030411.
(171) Kim, Y.; Han Wi, D.; Wook Hong, J.; Woo Han, S. Plasmonic Nanocrystal Assembly–Semiconductor Hybrids for Boosting Visible to Near-Infrared Photocatalysis. *ACS Nano* **2023**, *17* (18), 18641–18651. https://doi.org/10.1021/acsnano.3c08182.
(172) Fan, Y.; Girard, A.; Waals, M.; Salzemann, C.; Courty, A. Ag@Pt Core–Shell Nanoparticles for Plasmonic Catalysis. *ACS Appl Nano Mater* **2023**, *6* (2), 1193–1202. https://doi.org/10.1021/acsanm.2c04767.

(173) Su, H.; Tian, Q.; Hurd Price, C. A.; Xu, L.; Qian, K.; Liu, J. Nanoporous Core@shell Particles: Design, Preparation, Applications in Bioadsorption and Biocatalysis. *Nano Today* **2020**, *31*, 100834. https://doi.org/10.1016/J.NANTOD.2019.100834.
(174) Lou, D.; Zhu, Z.; Xu, Y. F.; Li, C.; Feng, K.; Zhang, D.; Lv, K.; Wu, Z.; Zhang, C.; Ozin, G. A.; He, L.; Zhang, X. A Core-Shell Catalyst Design Boosts the Performance of Photothermal Reverse Water Gas Shift Catalysis. *Sci China Mater* **2021**, *64* (9), 2212–2220. https://doi.org/10.1007/s40843-020-1630-2.
(175) Bayles, A.; Tian, S.; Zhou, J.; Yuan, L.; Yuan, Y.; R. Jacobson, C.; Farr, C.; Zhang, M.; F. Swearer, D.; Solti, D.; Lou, M.; O. Everitt, H.; Nordlander, P.; J. Halas, N. Al@TiO2 Core–Shell Nanoparticles for Plasmonic Photocatalysis. *ACS Nano* **2022**, *16* (4), 5839–5850. https://doi.org/10.1021/acsnano.1c10995.
(176) Han, J.; C. Freyman, M.; Feigenbaum, E.; Yong-Jin Han, T. Electro-Optical Device with Tunable Transparency Using Colloidal Core/Shell Nanoparticles. *ACS Photonics* **2018**, *5* (4), 1343–1350. https://doi.org/10.1021/acsphotonics.7b01337.
(177) Miranti, R.; Shin, D.; Dwi Septianto, R.; Ibáñez, M.; V. Kovalenko, M.; Matsushita, N.; Iwasa, Y.; Zulkarnaen Bisri, S. Exclusive Electron Transport in Core@Shell PbTe@PbS Colloidal Semiconductor Nanocrystal Assemblies. *ACS Nano* **2020**, *14* (3), 3242–3250. https://doi.org/10.1021/acsnano.9b08687.
(178) Li, C. L.; Chang, C. J.; Chen, J. K. Fabrication of Sandwich Structured Devices Encapsulating Core/Shell SiO2/Fe3O4 Nanoparticle Microspheres as Media for Magneto-Responsive Transmittance. *Sens Actuators B Chem* **2015**, *210*, 46–55. https://doi.org/10.1016/J.SNB.2014.12.094.
(179) S. Levin, C.; Hofmann, C.; A. Ali, T.; T. Kelly, A.; Morosan, E.; Nordlander, P.; H. Whitmire, K.; J. Halas, N. Magnetic−Plasmonic Core−Shell Nanoparticles. *ACS Nano* **2009**, *3* (6), 1379–1388. https://doi.org/10.1021/nn900118a.
(180) Yao, K.; Liu, Y. Infrared Plasmonic Resonators Based on Self-Assembled Core–Shell Particles. *ACS Photonics* **2017**, *5* (3), 844–851. https://doi.org/10.1021/acsphotonics.7b01012.
(181) Wei, M.; Serpe, M. J. Temperature–Light Dual-Responsive Au@PNIPAm Core-Shell Microgel-Based Optical Devices. *Particle and Particle Systems Characterization* **2019**, *36* (1). https://doi.org/10.1002/ppsc.201800326.
(182) Palanikumar, L.; Kalmouni, M.; Houhou, T.; Abdullah, O.; Ali, L.; Pasricha, R.; Straubinger, R.; Thomas, S.; Jawaad Afzal, A.; N. Barrera, F.; Magzoub, M. PH-Responsive Upconversion Mesoporous Silica Nanospheres for Combined Multimodal Diagnostic Imaging and Targeted Photodynamic and Photothermal Cancer Therapy. *ACS Nano* **2023**, *0* (0). https://doi.org/10.1021/acsnano.3c04564.
(183) Garg, A.; Milina, M.; Ball, M.; Zanchet, D.; Hunt, S. T.; Dumesic, J. A.; Román-Leshkov, Y. Transition-Metal Nitride Core@Noble-Metal Shell Nanoparticles as Highly CO Tolerant Catalysts. *Angewandte Chemie* **2017**, *129* (30), 8954–8959. https://doi.org/10.1002/ange.201704632.
(184) Tian, X.; Tang, H.; Luo, J.; Nan, H.; Shu, T.; Du, L.; Zeng, J.; Liao, S.; R. Adzic, R. High-Performance Core–Shell Catalyst with Nitride Nanoparticles as a Core: Well-Defined Titanium Copper Nitride Coated with an Atomic Pt Layer for the Oxygen Reduction Reaction. *ACS Catal* **2017**, *7* (6), 3810–3817. https://doi.org/10.1021/acscatal.7b00366.

(185) Singh, A.; Shishodia, M. S. Graphene vs. Silica Coated Refractory Nitrides Based Core-Shell Nanoparticles for Nanoplasmonic Sensing. *Physica E Low Dimens Syst Nanostruct* **2020**, *124*, 114288. https://doi.org/10.1016/J.PHYSE.2020.114288.
(186) Dong, S.; Chen, X.; Gu, L.; Zhou, X.; Wang, H.; Liu, Z.; Han, P.; Yao, J.; Wang, L.; Cui, G.; Chen, L. TiN/VN Composites with Core/Shell Structure for Supercapacitors. *Mater Res Bull* **2011**, *46* (6), 835–839. https://doi.org/10.1016/J.MATERRESBULL.2011.02.028.
(187) Yang, Y.; Zeng, R.; Xiong, Y.; J. DiSalvo, F.; D. Abruña, H. Cobalt-Based Nitride-Core Oxide-Shell Oxygen Reduction Electrocatalysts. *J Am Chem Soc* **2019**, *141* (49), 19241–19245. https://doi.org/10.1021/jacs.9b10809.
(188) M. Tackett, B.; Sheng, W.; Kattel, S.; Yao, S.; Yan, B.; A. Kuttiyiel, K.; Wu, Q.; G. Chen, J. Reducing Iridium Loading in Oxygen Evolution Reaction Electrocatalysts Using Core–Shell Particles with Nitride Cores. *ACS Catal* **2018**, *8* (3), 2615–2621. https://doi.org/10.1021/acscatal.7b04410.
(189) Li, Y.; Yan, Y.; Ming, H.; Zheng, J. One-Step Synthesis Fe3N Surface-Modified Fe3O4 Nanoparticles with Excellent Lithium Storage Ability. *Appl Surf Sci* **2014**, *305*, 683–688. https://doi.org/10.1016/J.APSUSC.2014.03.169.
(190) Kim, H.; Im, P. W.; Piao, Y. A Facile Route for the Preparation of Monodisperse Iron Nitride at Silica Core/Shell Nanostructures. *Front Bioeng Biotechnol* **2021**, *9*. https://doi.org/10.3389/fbioe.2021.735727.
(191) Exarhos, S.; Alvarez-Barragan, A.; Aytan, E.; A. Balandin, A.; Mangolini, L. Plasmonic Core–Shell Zirconium Nitride–Silicon Oxynitride Nanoparticles. *ACS Energy Lett* **2018**, *3* (10), 2349–2356. https://doi.org/10.1021/acsenergylett.8b01478.
(192) Mohsen, A. A.; Zahran, M.; Habib, S. E. D.; Allam, N. K. Refractory Plasmonics Enabling 20% Efficient Lead-Free Perovskite Solar Cells. *Sci Rep* **2020**, *10* (1). https://doi.org/10.1038/s41598-020-63745-7.
(193) Noguchi, S.; Odahara, J.; Sakai, H.; Carolina Rosero-Navarro, N.; Miura, A.; Tadanaga, K. Combustion Reactions between Transition-Metal Chlorides and Sodium Amide and Their Ignition Temperature. *Inorg Chem* **2021**, *60* (17), 12753–12758. https://doi.org/10.1021/acs.inorgchem.1c00557.
(194) Miura, A. Low-Temperature Synthesis and Rational Design of Nitrides and Oxynitrides for Novel Functional Material Development. *Journal of the Ceramic Society of Japan* **2017**, *125* (7), 552–558.
(195) Tadanaga, K.; Morita, K.; Mori, K.; Tatsumisago, M. Synthesis of Monodispersed Silica Nanoparticles with High Concentration by the Stöber Process. *J Solgel Sci Technol* **2013**, *68* (2), 341–345. https://doi.org/10.1007/s10971-013-3175-6.
(196) Lee, H. B.; Yoo, Y. M.; Han, Y. H. Characteristic Optical Properties and Synthesis of Gold–Silica Core–Shell Colloids. *Scr Mater* **2006**, *55* (12), 1127–1129. https://doi.org/10.1016/J.SCRIPTAMAT.2006.08.044.
(197) Bahadur, N. M.; Watanabe, S.; Furusawa, T.; Sato, M.; Kurayama, F.; Siddiquey, I. A.; Kobayashi, Y.; Suzuki, N. Rapid One-Step Synthesis, Characterization and Functionalization of Silica Coated Gold Nanoparticles. *Colloids Surf A Physicochem Eng Asp* **2011**, *392* (1), 137–144. https://doi.org/10.1016/J.COLSURFA.2011.09.046.
(198) Engelbrekt, C.; Gargasya, Y.; Law, M. Silica Shell Growth on Vitreophobic Gold Nanoparticles Probed by Plasmon Resonance Dynamics. *The Journal of Physical Chemistry C* **2021**, *125* (45), 25119–25125. https://doi.org/10.1021/acs.jpcc.1c07969.

(199) Yang, P.; Ando, M.; Murase, N. Various Au Nanoparticle Organizations Fabricated through SiO2 Monomer Induced Self-Assembly. *Langmuir* **2011**, *27* (3), 895–901. https://doi.org/10.1021/la103143j.
(200) Luis Montaño-Priede, J.; Paulo Coelho, J.; Guerrero-Martínez, A.; Peña-Rodríguez, O.; Pal, U. Fabrication of Monodispersed Au@SiO2 Nanoparticles with Highly Stable Silica Layers by Ultrasound-Assisted Stöber Method. *The Journal of Physical Chemistry C* **2017**, *121* (17), 9543–9551. https://doi.org/10.1021/acs.jpcc.7b00933.
(201) Cathcart, N.; Murshid, N.; Campbell, P.; Kitaev, V. Selective Plasmonic Sensing and Highly Ordered Metallodielectrics via Encapsulation of Plasmonic Metal Nanoparticles with Metal Oxides. *ACS Appl Nano Mater* **2018**, *1* (11), 6514–6524. https://doi.org/10.1021/acsanm.8b01964.
(202) L. Ding, H.; X. Zhang, Y.; Wang, S.; M. Xu, J.; C. Xu, S.; H. Li, G. Fe3O4@SiO2 Core/Shell Nanoparticles: The Silica Coating Regulations with a Single Core for Different Core Sizes and Shell Thicknesses. *Chemistry of Materials* **2012**, *24* (23), 4572–4580. https://doi.org/10.1021/cm302828d.
(203) Zhong, Q.; Cao, M.; Hu, H.; Yang, D.; Chen, M.; Li, P.; Wu, L.; Zhang, Q. One-Pot Synthesis of Highly Stable CsPbBr3@SiO2 Core–Shell Nanoparticles. *ACS Nano* **2018**, *12* (8), 8579–8587. https://doi.org/10.1021/acsnano.8b04209.
(204) Yang, P.; Ando, M.; Murase, N. Highly Luminescent CdSe/CdxZn1–XS Quantum Dots Coated with Thickness-Controlled SiO2 Shell through Silanization. *Langmuir* **2011**, *27* (15), 9535–9540. https://doi.org/10.1021/la201213c.
(205) J. Sandoval, P.; Lopez, K.; Arreola, A.; Len, A.; Basravi, N.; Yamaguchi, P.; Kawamura, R.; X. Stokes, C.; Melendrez, C.; Simpson, D.; Lee, S.-J.; James Titus, C.; Altoe, V.; Sainio, S.; Nordlund, D.; Irwin, K.; Wolcott, A. Quantum Diamonds at the Beach: Chemical Insights into Silica Growth on Nanoscale Diamond Using Multimodal Characterization and Simulation. *ACS Nanoscience Au* **2023**, *0* (0). https://doi.org/10.1021/acsnanoscienceau.3c00033.
(206) Chen, X. J.; Struzhkin, V. V.; Kung, S.; Mao, H. K.; Hemley, R. J.; Christensen, A. N. Pressure-Induced Phonon Frequency Shifts in Transition-Metal Nitrides. *Phys Rev B Condens Matter Mater Phys* **2004**, *70* (1). https://doi.org/10.1103/PhysRevB.70.014501.
(207) Shah, W. H.; Iqbal, Y.; Safeen, A.; Safeen, K.; Khan, G.; Shah, W. H.; Ahmed, I.; Khan, S.; Zhao, T.; Ul-Haq, K. Study of the Structural and Electrical Properties of Silicon Ion Irradiated Zirconium Nitride Thin Films. *Modern Physics Letters B* **2018**, *32* (24), 1850281. https://doi.org/10.1142/S0217984918502810.
(208) Sato, Y.; Hayami, R.; Gunji, T. Characterization of NMR, IR, and Raman Spectra for Siloxanes and Silsesquioxanes: A Mini Review. *J Solgel Sci Technol* **2022**, *104* (1), 36–52. https://doi.org/10.1007/s10971-022-05920-y.
(209) Hong, Y. A.; Ha, J. W. Enhanced Refractive Index Sensitivity of Localized Surface Plasmon Resonance Inflection Points in Single Hollow Gold Nanospheres with Inner Cavity. *Sci Rep* **2022**, *12* (1). https://doi.org/10.1038/s41598-022-11197-6.
(210) Eurov, D. A.; Kirilenko, D. A.; Sharonova, L. V.; Shvidchenko, A. V.; Smirnov, A. N.; Tomkovich, M. V.; Yagovkina, M. A.; Kurdyukov, D. A. Formation of Stable Microporous Core-Shell V2O5/SiO2 Colloidal Particles Potential for Heterogeneous Catalysis. *Mater Today Commun* **2023**, *35*, 106047. https://doi.org/10.1016/J.MTCOMM.2023.106047.

(211) Cheng, C. C.; Chen, J. K.; Shieh, Y. T.; Lee, D. J. Supramolecular Core-Shell Nanoparticles for Photoconductive Device Applications. *Nanotechnology* **2016**, *27* (32). https://doi.org/10.1088/0957-4484/27/32/32LT01.
(212) Li, C.-L.; Huang, B.-R.; Chang, J.-Y.; Chen, J.-K. Bifunctional Superparamagnetic-Luminescent Core-Shell-Satellite Structured Microspheres: Preparation, Characterization, and Magnetodisplay Application. *J. Mater. Chem. C* **2015**, *3* (18), 4603. https://doi.org/10.1039/c5tc00255a.
(213) Di, Y.; Qin, T. Plasmonic ZrN@TiO2 Core-Shell Nanostructure Enhancing Photovoltaic Performance of Dye-Sensitized Solar Cells. *Opt Mater (Amst)* **2022**, *132*. https://doi.org/10.1016/j.optmat.2022.112813.
(214) Noguchi, S.; Miura, A.; Tadanaga, K. Synthesis of ZrN–SiO $_2$ Core–Shell Particles by a Sol–Gel Process and Use as Particle-based Structured Coloring Material. *Journal of the American Ceramic Society* **2024**. https://doi.org/10.1111/jace.19981.
(215) El-Deen, S. S.; Hashem, A. M.; Abdel Ghany, A. E.; Indris, S.; Ehrenberg, H.; Mauger, A.; Julien, C. M. Anatase TiO2 Nanoparticles for Lithium-Ion Batteries. *Ionics (Kiel)* **2018**, *24* (10), 2925–2934. https://doi.org/10.1007/s11581-017-2425-y.
(216) Ponon, N. K.; Appleby, D. J. R.; Arac, E.; King, P. J.; Ganti, S.; Kwa, K. S. K.; O'Neill, A. Effect of Deposition Conditions and Post Deposition Anneal on Reactively Sputtered Titanium Nitride Thin Films. *Thin Solid Films* **2015**, *578*, 31–37. https://doi.org/10.1016/j.tsf.2015.02.009.
(217) Pastukhov, A. I.; Savinov, M. S.; Zelepukin, I. V.; Babkova, J. S.; Tikhonowski, G. V.; Popov, A. A.; Klimentov, S. M.; Devi, A.; Patra, A.; Zavestovskaya, I. N.; Deyev, S. M.; Kabashin, A. V. Laser-Synthesized Plasmonic HfN-Based Nanoparticles as a Novel Multifunctional Agent for Photothermal Therapy. *Nanoscale* **2024**. https://doi.org/10.1039/d4nr02311k.
(218) Gao, X.; Zou, C.; Zhou, H.; Yuan, C.; He, J.; Luo, X. Enhanced Nonlinear Optical Properties of Alloyed AgCu Glassy Nanoparticles. *J Alloys Compd* **2020**, *819*. https://doi.org/10.1016/j.jallcom.2019.153003.
(219) Liu, X. Colloidal Plasmonic Nanoparticles for Ultrafast Optical Switching and Laser Pulse Generation. *Frontiers in Materials*. Frontiers Media S.A. September 25, 2018. https://doi.org/10.3389/fmats.2018.00059.
(220) Wang, X.; Yang, Z.; Zhang, Y.; Jing, L.; Zhao, Y.; Yan, Y.; Sun, K. MnO2 Supported Pt Nanoparticels with High Electrocatalytic Activity for Oxygen Reduction Reaction. *Fuel Cells* **2014**, *14* (1), 35–41. https://doi.org/10.1002/fuce.201300102.
(221) Liu, S.; Fu, S.; Zhang, X.; Wang, X.; Kang, L.; Han, X.; Chen, X.; Wu, J.; Liu, Y. UV-Resistant Holographic Data Storage in Noble-Metal/Semiconductor Nanocomposite Films with Electron-Acceptors. *Opt Mater Express* **2018**, *8* (5), 1143. https://doi.org/10.1364/ome.8.001143.
(222) L. Efros, A.; E. Brus, L. Nanocrystal Quantum Dots: From Discovery to Modern Development. *ACS Nano* **2021**, *15* (4), 6192–6210. https://doi.org/10.1021/acsnano.1c01399.
(223) Liu, F.; Jang, M. H.; Ha, H. D.; Kim, J. H.; Cho, Y. H.; Seo, T. S. Facile Synthetic Method for Pristine Graphene Quantum Dots and Graphene Oxide Quantum Dots: Origin of Blue and Green Luminescence. *Advanced Materials* **2013**, *25* (27), 3657–3662. https://doi.org/10.1002/adma.201300233.

(224) Henini, M.; Patane Á, A.; Polimeni, A.; Levin, A.; Eaves, L.; Main, P. C.; Hill, G. Electrical and Optical Properties of Self-Assembled Quantum Dots. *Microelectronics J* **2002**, *33*, 313–318. https://doi.org/10.1016/S0026-2692(01)00124-0.
(225) Horva Âth, Z. J.; Do Âzsa, L.; Van Tuyen, V.; Po, B.; Èr, Í.; Nemcsics, A. Â.; Frigeri, P.; Gombia, E.; Mosca, R.; Franchi, S. Growth and Electrical Characteristics of InAs/GaAs Quantum Well and Quantum Dot Structures. *Thin Solid Films* **2000**, *367*, 89–92. https://doi.org/10.1016/S0040-6090(00)00701-X.
(226) Guler, U.; Shalaev, V. M.; Boltasseva, A. Nanoparticle Plasmonics: Going Practical with Transition Metal Nitrides. *Materials Today*. Elsevier B.V. May 1, 2015, pp 227–237. https://doi.org/10.1016/j.mattod.2014.10.039.
(227) Kelly, K. L.; Coronado, E.; Zhao, L. L.; Schatz, G. C. The Optical Properties of Metal Nanoparticles: The Influence of Size, Shape, and Dielectric Environment. *Journal of Physical Chemistry B* **2003**, *107* (3), 668–677. https://doi.org/10.1021/jp026731y.
(228) Freyschlag, C. G.; Madix, R. J. Precious Metal Magic: Catalytic Wizardry. *Materials Today* **2011**, *14* (4), 134–142.
(229) Yuan, Y.; Wang, J.; Adimi, S.; Shen, H.; Thomas, T.; Ma, R.; Attfield, J. P.; Yang, M. Zirconium Nitride Catalysts Surpass Platinum for Oxygen Reduction. *Nat Mater* **2019**, *19* (March), 282–286. https://doi.org/10.1038/s41563-019-0535-9.
(230) Baturina, O. A.; Epshteyn, A.; Leff, A. C.; Purdy, A. P.; Brintlinger, T.; Simpkins, B. S.; Santiago, E. Y.; Govorov, A. O. Photoelectrochemical Methanol Oxidation Under Visible and UV Excitation of TiO2-Supported TiN and ZrN Plasmonic Nanoparticles. *J Electrochem Soc* **2021**, *168* (1), 016503. https://doi.org/10.1149/1945-7111/abd605.
(231) Liu, Y.; Zhang, X.; Lu, L.; Ye, J.; Wang, J.; Li, X.; Bai, X.; Wang, W. Nanoplasmonic Zirconium Nitride Photocatalyst for Direct Overall Water Splitting. *Chinese Chemical Letters* **2022**, *33* (3), 1271–1274. https://doi.org/10.1016/j.cclet.2021.07.054.
(232) Haque, M. A.; Kamita, G.; Kurokawa, T.; Tsujii, K.; Gong, J. P. Unidirectional Alignment of Lamellar Bilayer in Hydrogel: One-Dimensional Swelling, Anisotropic Modulus, and Stress/Strain Tunable Structural Color. *Advanced Materials* **2010**, *22* (45), 5110–5114. https://doi.org/10.1002/adma.201002509.
(233) Anamul Haque, Md.; Kurokawa, T.; Kamita, G.; Yue, Y.; Ping Gong, J. Rapid and Reversible Tuning of Structural Color of a Hydrogel over the Entire Visible Spectrum by Mechanical Stimulation. *Chemistry of Materials* **2011**, *23* (23), 5200–5207. https://doi.org/10.1021/cm2021142.
(234) Chung, K.; Yu, S.; Heo, C. J.; Shim, J. W.; Yang, S. M.; Han, M. G.; Lee, H. S.; Jin, Y.; Lee, S. Y.; Park, N.; Shin, J. H. Flexible, Angle-Independent, Structural Color Reflectors Inspired by Morpho Butterfly Wings. *Advanced Materials* **2012**, *24* (18), 2375–2379. https://doi.org/10.1002/adma.201200521.
(235) Saito, A.; Ishibashi, K.; Ohga, J.; Hirai, Y.; Kuwahara, Y. Fabrication Process of Large-Area Morpho-Color Flexible Film via Flexible Nano-Imprint Mold. *Journal of Photopolymer Science and Technology* **2018**, *31* (1), 113–119. https://doi.org/10.2494/photopolymer.31.113.
(236) He, J.; Liu, S.; Gao, G.; Sakai, M.; Hara, M.; Nakamura, Y.; Kishida, H.; Seki, T.; Takeoka, Y. Particle Size Controlled Chiral Structural Color of Monodisperse Cholesteric Liquid Crystals Particles. *Adv Opt Mater* **2023**, *11* (19). https://doi.org/10.1002/adom.202300296.

(237) Ohno, K.; Mizuta, Y. Structural Color Materials Using Polymer-Brush-Decorated Hybrid Particles. *ACS Appl Polym Mater* **2019**, *2* (2), 368–375. https://doi.org/10.1021/acsapm.9b00839.
(238) Zhu, X.; Wei, T.; Shawkey, M. D.; Xing, T.; Chen, G. Bioinspired Fabrication of Noniridescent Structurally Colored Cotton Fabric Based on Polystyrene@polycaffeic Acid Particles. *Ind Crops Prod* **2022**, *176*. https://doi.org/10.1016/j.indcrop.2021.114419.
(239) Schertel, L.; Siedentop, L.; Meijer, J. M.; Keim, P.; Aegerter, C. M.; Aubry, G. J.; Maret, G. The Structural Colors of Photonic Glasses. *Adv Opt Mater* **2019**, *7* (15). https://doi.org/10.1002/adom.201900442.
(240) Choi, D. S.; Choi, J. H.; Lee, C. Y. Structural Colors Based on Amorphous Arrays Comprised Solely of Silica Particles. *Applied Sciences* **2020**, *10* (1). https://doi.org/10.3390/app10010420.
(241) Abraham, L.; Thomas, T.; Pichumani, M. Vivid Structural Colors of Photonic Crystals: Self-Assembly of Monodisperse Silica Nano-Colloids Synthesized Using an Anionic Surfactant. *Chem Phys* **2022**, *563*. https://doi.org/10.1016/j.chemphys.2022.111682.
(242) Gao, W.; Rigout, M.; Owens, H. Self-Assembly of Silica Colloidal Crystal Thin Films with Tuneable Structural Colours over a Wide Visible Spectrum. *Appl Surf Sci* **2016**, *380*, 12–15. https://doi.org/10.1016/j.apsusc.2016.02.106.
(243) Hu, Y.; Zhang, Y.; Yang, D.; Ma, D.; Huang, S. Self-Assembly of Colloidal Particles into Amorphous Photonic Crystals. *Mater Adv* **2021**, *2*, 6499. https://doi.org/10.1039/d1ma00477h.
(244) Feng, L.; Wang, F.; Luo, H.; Qiu, B. Review of Recent Advancements in the Biomimicry of Structural Colors. *Dyes and Pigments*. Elsevier Ltd February 1, 2023. https://doi.org/10.1016/j.dyepig.2022.111019.
(245) Lama, M.; Ping Gong, J. Mechanical Reinforcement of Lamellar Bilayer Hydrogels by Small Amounts of Co-Surfactants. *ACS Omega* **2023**, *8* (28), 25185–25194. https://doi.org/10.1021/acsomega.3c02274.
(246) Xia, Y.; Gao, S.; He, H.; Wang, X.; Zeng, Z.; Chen, B.; Zou, N.; Cao, M.; Wang, S. A New and Straightforward Strategy to Prepare an Optical Hydrogel Film with Dynamic Structural Colors. *Journal of Physical Chemistry C* **2020**, *124* (29), 16083–16089. https://doi.org/10.1021/acs.jpcc.0c02878.
(247) J Pursiainen, O. L.; Baumberg, J. J.; Winkler, H.; Viel, B.; Spahn, P.; Tilmann Ruhl, and; Ghiradella, H.; Aneshansley, D.; Eisner, T.; Silberglied, R. E.; Hinton, H. E. *Ordered Arrangements of Spheres of Two Different Sizes in Opal*; 1965; Vol. 207. https://doi.org/10.1364/OA_License_v1#VOR.
(248) Josephson, D. P.; Popczun, E. J.; Stein, A. Effects of Integrated Carbon as a Light Absorber on the Coloration of Photonic Crystal-Based Pigments. *Journal of Physical Chemistry C* **2013**, *117* (26), 13585–13592. https://doi.org/10.1021/jp403129g.
(249) Vogel, N.; Utech, S.; England, G. T.; Shirman, T.; Phillips, K. R.; Koay, N.; Burgess, I. B.; Kolle, M.; Weitz, D. A.; Aizenberg, J. Color from Hierarchy: Diverse Optical Properties of Micron-Sized Spherical Colloidal Assemblies. *Proc Natl Acad Sci U S A* **2015**, *112* (35), 10845–10850. https://doi.org/10.1073/pnas.1506272112.
(250) Avci, C.; De Marco, M. L.; Byun, C.; Perrin, J.; Scheel, M.; Boissière, C.; Faustini, M. Metal–Organic Framework Photonic Balls: Single Object Analysis for Local Thermal Probing. *Advanced Materials* **2021**, *33* (43). https://doi.org/10.1002/adma.202104450.

(251) Noguchi, S.; Lama, M.; Fujii, Y.; Miura, A.; Tadanaga, K. Structural Color Materials with Color Mixing Effect Using Noble Metal-Free Plasmonic Particles in SiO2–ZrN System. *Adv Opt Mater* **2024**. https://doi.org/10.1002/adom.202400287.
(252) Yi, Y.; Yu, L.; Tian, Z.; Song, Y.; Shao, Y.; Gao, L.; Sun, J.; Liu, Z. Biotemplated Synthesis of Transition Metal Nitride Architectures for Flexible Printed Circuits and Wearable Energy Storages. *Adv Funct Mater* **2018**, *28* (50). https://doi.org/10.1002/adfm.201805510.
(253) Djire, A.; Pande, P.; Deb, A.; Siegel, J. B.; Ajenifujah, O. T.; He, L.; Sleightholme, A. E.; Rasmussen, P. G.; Thompson, L. T. Unveiling the Pseudocapacitive Charge Storage Mechanisms of Nanostructured Vanadium Nitrides Using In-Situ Analyses. *Nano Energy* **2019**, *60*, 72–81. https://doi.org/10.1016/j.nanoen.2019.03.003.
(254) Liu, Y.; Liu, L.; Kang, L.; Ran, F. Vanadium Nitride with Surface Single Specie Oxide via Vanadium-Organic Frameworks Precursor. *J Power Sources* **2020**, *450*. https://doi.org/10.1016/j.jpowsour.2019.227687.
(255) Teng, X.; Wei, M.; Yi, W.; Li, J.; Yin, M.; Xi, G. General Synthesis of Large-Area Transition Metal Nitride Porous Arrays for Highly Sensitive Surface-Enhanced Raman Scattering Substrates with Ultrahigh Durability. *Small Struct* **2023**, *4* (11). https://doi.org/10.1002/sstr.202300127.
(256) Kafizas, A.; Carmalt, C. J.; Parkin, I. P. CVD and Precursor Chemistry of Transition Metal Nitrides. *Coordination Chemistry Reviews*. July 2013, pp 2073–2119. https://doi.org/10.1016/j.ccr.2012.12.004.
(257) Schramke, K. S.; Qin, Y.; Held, J. T.; Mkhoyan, K. A.; Kortshagen, U. R. Nonthermal Plasma Synthesis of Titanium Nitride Nanocrystals with Plasmon Resonances at Near-Infrared Wavelengths Relevant to Photothermal Therapy. *ACS Appl Nano Mater* **2018**, *1* (6), 2869–2876. https://doi.org/10.1021/acsanm.8b00505.
(258) Alvarez Barragan, A.; Ilawe, N. V.; Zhong, L.; Wong, B. M.; Mangolini, L. A Non-Thermal Plasma Route to Plasmonic TiN Nanoparticles. *Journal of Physical Chemistry C* **2017**, *121* (4), 2316–2322. https://doi.org/10.1021/acs.jpcc.6b08910.
(259) Todd, P. K.; Fallon, M. J.; Neilson, J. R.; Zakutayev, A. Two-Step Solid-State Synthesis of Ternary Nitride Materials. *ACS Mater Lett* **2021**, *3* (12), 1677–1683. https://doi.org/10.1021/acsmaterialslett.1c00656.
(260) Karaballi, R. A.; Monfared, Y. E.; Dasog, M. Overview of Synthetic Methods to Prepare Plasmonic Transition-Metal Nitride Nanoparticles. *Chemistry - A European Journal* **2020**, *26* (39), 8499–8505. https://doi.org/10.1002/CHEM.201905217.
(261) Lalisse, A.; Tessier, G.; Plain, J.; Baffou, G. Plasmonic Efficiencies of Nanoparticles Made of Metal Nitrides (TiN, ZrN) Compared with Gold. *Sci Rep* **2016**, *6*. https://doi.org/10.1038/srep38647.
(262) Dasog, M. Transition Metal Nitrides Are Heating Up the Field of Plasmonics. *Chemistry of Materials* **2022**, *34* (10), 4249–4258. https://doi.org/10.1021/acs.chemmater.2c00305.
(263) Biliak, K.; Protsak, M.; Pleskunov, P.; Nikitin, D.; Hanuš, J.; Ali-Ogly, S.; Šomvársky, J.; Tosca, M.; Cieslar, M.; Košutová, T.; Dopita, M.; Lopes Ferreira, F.; Choukourov, A. Plasmonic TiN, ZrN, and HfN Nanofluids for Solar-to-Heat Conversion. *ACS Appl Nano Mater* **2023**, *6* (23), 21642–21651. https://doi.org/10.1021/acsanm.3c03662.
(264) Yang, Z. G.; Xu, H. M.; Shuai, T. Y.; Zhan, Q. N.; Zhang, Z. J.; Huang, K.; Dai, C.; Li, G. R. Recent Progress in the Synthesis of Transition Metal Nitride Catalysts and Their

Applications in Electrocatalysis. *Nanoscale*. Royal Society of Chemistry June 7, 2023, pp 11777–11800. https://doi.org/10.1039/d3nr01607b.

(265) Venugopal, N.; Gerasimov, V. S.; Ershov, A. E.; Karpov, S. V.; Polyutov, S. P. Titanium Nitride as Light Trapping Plasmonic Material in Silicon Solar Cell. *Opt Mater (Amst)* **2017**, *72*, 397–402. https://doi.org/10.1016/j.optmat.2017.06.035.

(266) Khezripour, Z.; Mahani, F. F.; Mokhtari, A. Performance Improvement of Ultrathin Organic Solar Cells Utilizing Light-Trapping Aluminum-Titanium Nitride Nanosquare Arrays. *Opt Mater (Amst)* **2018**, *84*, 651–657. https://doi.org/10.1016/j.optmat.2018.07.073.

(267) Han, Y.; Yue, X.; Jin, Y.; Huang, X.; Shen, P. K. Hydrogen Evolution Reaction in Acidic Media on Single-Crystalline Titanium Nitride Nanowires as an Efficient Non-Noble Metal Electrocatalyst. *J Mater Chem A Mater* **2016**, *4* (10), 3673–3677. https://doi.org/10.1039/c5ta09976e.

(268) Defilippi, C.; Shinde, D. V.; Dang, Z.; Manna, L.; Hardacre, C.; Greer, A. J.; D'Agostino, C.; Giordano, C. HfN Nanoparticles: An Unexplored Catalyst for the Electrocatalytic Oxygen Evolution Reaction. *Angewandte Chemie* **2019**, *131* (43), 15610–15616. https://doi.org/10.1002/ange.201908758.

I sincerely hope that the contents of this dissertation will contribute to the advancement of science and technology, as well as to the promotion of peace for humanity.

NOGUCHI Shinji / 野口 真司